Studies on Wheel/Rail Contact – Impact Forces at Insulated Rail Joints

Tao Pang, B.Eng

A Thesis Submitted in Partial Fulfilment for the Award of the Degree of

Master of Engineering

Centre for Railway Engineering

Central Queensland University

Australia

June 2007

ABSTRACT

To investigate the wheel/rail contact impact forces at insulated rail joints (IRJs), a three-dimensional finite element model and strain gauged experiments are employed and reported in this thesis. The 3D wheel/rail contact-impact FE model adopts a two-stage analysis strategy in which the wheel-IRJ railhead contact is first established in the static analysis and the results transferred to dynamic analysis for impact simulations. The explicit FE method was employed in the dynamic analysis. The Lagrange Multiplier method and the Penalty method for contact constraint enforcement were adopted for the static and dynamic analyses respectively.

The wheel/rail contact-impact in the vicinity of the end post is exhibited via numerical examples from the FE modelling. The wheel/rail contact impact mechanism is investigated. The strain gauged experiments which consist of a lab test and a field test are reported. The signature of the strain time series from the field test demonstrates a plausible record of the dynamic responses due to the wheel/rail contact impact. By using the experimental data, both the static and the dynamic FE models are validated.

It is found that the stiffness discontinuity of the IRJ structure causes a running surface geometry discontinuity during the wheel passages which then causes the impact in the vicinity of the end post. Through a series of sensitivity studies of several IRJ design parameters, it is shown that the IRJ performance can be effectively improved with optimised design parameters.

TABLE OF CONTENTS

LIST OF FIGURES

LIST OF TABLES

LIST OF SYMBOLS

MATHEMATICAL SYMBOLS

$[\,]$	Rectangular or square matrix
$[\,]^T$	Matrix transpose
$[\,]^{-1}$	Matrix inverse
$\| \|$	Norm of a matrix or a vector
$\bullet$	Time differentiation (over dot)
$-$	Boundary value (over bar)

LATIN SYMBOLS

a	Major axis of elliptical contact area
A	Contact area
B	Strain-displacement matrix
b	Minor axis of elliptical contact area
C_d	Material damping
c_0	Stress wave propagation speed
D	Elasticity matrix
E	Young's modulus
F	Concentrated force
f	Body force
f_b	Boundary force
g	Gap function of contact surfaces
G	Shear modulus

h	Depth of Hertz elastic foundation
I	Identity matrix
K	System stiffness matrix
k	Stiffness matrix
L_e	Dimension of characteristic element
M	Mass matrix
N	Shape function
n	Normal vector to the contact surface
p	Normal contact pressure
p_0	Peak value of contact pressure at the centre of contact area
q	Tangential contact traction
R	Radius of curvature
s	Distance of loading point from the origin
t	Time
u	Displacement
v	Velocity
Z	Contact body profile
x, y, z	Coordinate of rectangular Cartesian reference system

GREEK SYMBOLS

α	Semi angle of wedge and cone
β	Measures of material difference of contact bodies
ε	Normal strain
γ	Shear stain

σ	Normal stress
τ	Shear stress
ρ	Density
ξ	Fraction of critical damping
$\omega_{\max}$	System frequency of highest mode
λ	Lagrange multiplier
ζ	Integral variable of potential function
ν	Poison ratio of the material
μ	Friction coefficient
υ	Interpolation parameter for velocity
ϑ	Interpolation parameter for displacement
Π	Energy function
χ	Penalty parameters

LIST OF ACRONYMS

2D	Two-dimension
3D	Three-dimension
CRE	Centre for Railway Engineering
CQU	Central Queensland University
DOF	Degree of Freedom
FE	Finite element
FEA	Finite element analysis
FEM	Finite element method
HCT	Hertzian contact theory
HTL	Heavy Testing Laboratory
IRJ	Insulated rail joint
QR	Queensland Rail
RMD	Rigid multibody dynamics

ACKNOWLEDGEMENTS

I would like to thank all those people who have given me generous help and supports during the past two years.

Many thanks to my supervisor, A/Prof. Manicka Dhanasekar, director for Centre for Railway Engineering; I sincerely appreciated his sustained guide and support in both academic and personal way from the commencement to the completion of my master program.

I also would like to express my appreciation to the research staffs in Centre for Railway Engineering, Mr. Trevor Ashman, Mr. Grant Caynes, A/Prof. Colin Cole, Mr. Paul Boyd and many QR engineers who has made major contribution to the important and interesting experiment in this research.

Thanks to Mr. Tim McSweeney, Research Support Officer in Centre for Railway Engineering, for his generous help throughout my two years' research and precious advices in the final stage of thesis writing.

The thesis was possible thanks to the scholarship awarded by the Centre for Railway Engineering, Central Queensland University, Australia RailCRC and Queensland Rail.

Special thankfulness to my parents, my girlfriend Saina and all my friends I met in Australia, only with your support, help and understanding I could accomplish this thesis.

DECLARATION

The work contained in this thesis is a direct result of the original work carried out by me and has not previously been submitted for the award of a degree or diploma at any other tertiary institution in Australia or Overseas

Signed: ________________ Date: 29th June, 2007

Tao Pang

Author

1. Introduction

Insulated rail joints (IRJs) are safety critical sections in the signalling system of the rail network. To realise the electrical isolation function, insulation materials are inserted between rail ends secured by the joint bars and bolts. IRJs are also regarded as weak spots of the track structure and posses short service life. This situation stimulates high demand from the rail companies to improve the performance of IRJs; the study on the failure of IRJs has also became a recent focus in the international railway engineering research community.

To improve the performance of IRJs, understanding its failure mechanism is a priority. There are various failure modes corresponding to different designs of IRJs. In Australia, the railhead metal flow/material fatigue in the vicinity of the end post is regarded as the most common failure mode. As the wheels pass over the IRJs, severe wheel/rail contact impact loads are excited. Under such high level cyclic impact loads of wheel passages, the metal flow/material fatigue is initiated. With a view to fully understand the failure mechanism of the IRJs, study on the contact impact force between the running surfaces of the wheel and the rail is essential. As a part of an overall research project which aims to investigate the failure mechanism of the IRJ, this thesis studies the wheel/rail contact impact force using finite element analysis (FEA) and strain gauged laboratory and field experiments. The study on the material failure issue is conducted in another PhD thesis in which the impact loads and the associated contact results from this thesis are used as the input data.

1.1. Aims and Objectives

The aim of this research is to examine the wheel/rail contact-impact forces at IRJs. This aim is achieved through the following research procedures:

- Review the existing methods/models for determining wheel/rail contact-impact forces.
- Develop a 3D wheel rail contact impact FE model of an IRJ
- Examine the effect of several selected design and operational parameters on the contact-impact force excitation.
- Validate the FE model with experimental field data where possible.

1.2. Scope and Limitations

The scope of this research is to investigate the contact-impact force excited by a new wheel and a new IRJ; in other words, the stiffness discontinuity of IRJs rather than other running surface defects excites the impact forces that are of interest to this research. The vertical contact-impact force is examined in detail as it provides the major contribution to the damage. The associated contact responses are also examined for further study of the failure mechanism of IRJs. A sensitivity study of several key design and operational parameters is also included.

Due to the complexity of the modelling involved in the investigation of the wheel/rail contact-impact on the railhead in the vicinity of the end post, the following aspects are considered as out of the scope of this research:

- The wear and defects on either the railhead or the wheel tread
- Railway track misalignments

- Curved track
- Longitudinal stress resulting from temperature fluctuations
- Looseness of bolts
- Wagon/bogie/wheelset dynamics

1.3. Thesis Structure

This thesis contains eight chapters presenting the reviews of IRJ designs, literature reviews of wheel rail contact, contact-impact theories, FE modelling, numerical examples, strain gauged experiment as well as the FE model validation.

To improve the service life, various IRJs designs are employed in different countries; the major design parameters in those cases are reviewed in Chapter 2. The failure mechanisms of a typical IRJ are presented and a hypothesis for the common failure mode within the Australian heavy haul network, namely, the mechanical fatigue and/or metal plastic flow at the railhead in the vicinity of the end post under high level wheel/rail impact forces is presented. The models of wheel/rail contact impact reported in the literature are also reviewed in detail.

Chapter 3 reports the mechanics of contact and the theory of the finite element method. Both the classical and the computational theories of contact mechanics are reviewed. The solution methods for FEM are also briefly introduced. The explicit method employed in this research is introduced. The algorithms of FE modelling of contact impact are also presented.

The modelling of wheel/rail contact impact at IRJs is fairly complex; hence it needs some model idealisations to reduce the model size. In Chapter 4, the IRJs and the wheel geometry, material and boundary conditions are reviewed and then simplified. The wheel/rail contact establishment is presented. The details of loading, boundary conditions and contact definitions are reported. The meshing strategy that affects the model accuracy and efficiency is also presented in detail.

Chapter 5 presents numerical examples of wheel/rail contact impact at IRJs. Both static and dynamic analysis results are reported in detail and attention is also paid to compare the numerical results with the HCT. This chapter also provides results that prove the model is capable of providing both plausible and logical results. Sensitivity of some major design parameters is investigated for better understanding of the cause of impact as well as to achieve the future design improvement. The IRJ with optimised design parameters shows that the impact force can be effectively reduced to an insignificant level.

Chapter 6 briefly reports lab tests and field tests conducted as part of an ongoing research at the Centre for Railway Engineering (CRE) with the support from QR. The data collected from both tests are processed and compared to the numerical results. In the lab test, the IRJ is simply supported and subjected to a static load and investigated with several different loading positions along the length of the IRJ. In the field test, a continuous welded rail segment in the field is replaced by the strain gauged IRJ. A field installed data recording system has captured the dynamic response of the IRJ due to wheel passages. The signature of the strain data from the field test is also presented and discussed.

Chapter 7 reports the validation of the FE model. Both the static and the dynamic FE models are validated using the experimental data and reasonable agreements are achieved. Two traffic conditions in the field test, namely loaded and unloaded coal wagon traffic, are selected to validate the dynamic analysis.

The summary, conclusions and recommendations of this thesis are reported in Chapter 8.

2. Review of Insulated Rail Joints (IRJs)

2.1. Introduction

This chapter presents a review of insulated rail joints (IRJs). As safety critical sections of the signalling system in rail networks, the significance of IRJs is presented first in Section 2.2. Various IRJ designs employed worldwide are reviewed in Section 2.3. The failure modes of IRJs are described in Section 2.4 and a hypothesis of failure of the IRJs used in the heavy haul network of the Australian railways is reported in Section 2.5. Wheel/rail contact impact at IRJs that is believed to be the key factor of initiating the IRJ failure is explained in Section 2.6.

2.2. Significance of IRJs

IRJs are used to electrically isolate the rails as part of the system to achieve signal control. Failure of IRJs is a significant safety issue. As such the rail infrastructure owners take extreme care in maintaining the IRJs in sound condition.

Structurally IRJs are designed as bolted joints with each component electrically isolated from each other. As for all types of joints which involve a discontinuity in the rail, IRJs are considered to be weak spots in the rail track. The service life of IRJs is typically 100 MGT, which is considerably shorter than other rail components that withstand as high as 1000MGT (Davis, 2005). The annual cost to the Australian rail industry for the maintenance and replacement of IRJs has been conservatively estimated to be \$5.4 million in direct costs and \$1.1 million in indirect costs annually (RailCRC 2003). Investigation of the failure mechanism of IRJs with a view to improving their performance has, therefore, assumed prominence in recent times.

2.3. Designs of IRJ

IRJs comprise of an insulation material (end post) fixed between the ends of two adjacent lengths of rail, and secured by bolted joint bars that connect the two rails. Several designs of IRJs are reported in the literature. The designs vary in terms of the parameters of the supporting systems, joint bars and insulation end posts.

Two types of supporting systems of IRJs exist depending on the positionings of the sleepers with reference to the end post:

i) Suspended IRJ

ii) Supported IRJ

As shown in Fig. 2.1, the suspended IRJ has the sleepers positioned symmetric to the end post. For the suspended IRJ, there is no support underneath the end post.

On the other hand, for the supported IRJ, the end post is placed directly on the sleepers. There are two types of designs:

i) Continuously supported

ii) Discretely supported

Figure 2.1 Suspended IRJ (RAILFOTO, 2005)

Continuous insulated joints (Fig. 2.2) are continuously supported at the rail base using the specially designed joint bar. A special tie plate known as “abrasion plate” is also used to support the joint.

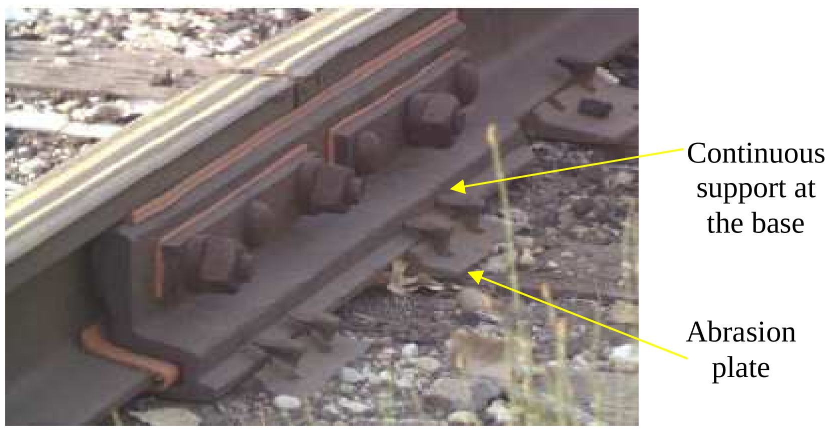

Figure 2.2 Continuously Supported Insulated Joint (AREMA, 2006)

The end post of the discretely supported IRJ is directly placed on a sleeper, as shown in Fig. 2.3.

Fig. 2.4 shows another type of discretely supported IRJ, which employs two sleepers together at the centre.

Figure 2.3 Discretely supported IRJ (LBfoster, 2006)

Figure 2.4. Supported IRJ (Esveld, 2001)

The joint bar designs are characterised by various cross-section designs and the length of joint bar, namely 4-bolt joint bar and 6-bolt joint bar. Various cross-section shapes are shown in Fig. 2.5. For simplicity, instead of showing the symmetric joint bars on both sides of rail, the joint bar on just one side only is presented in this figure.

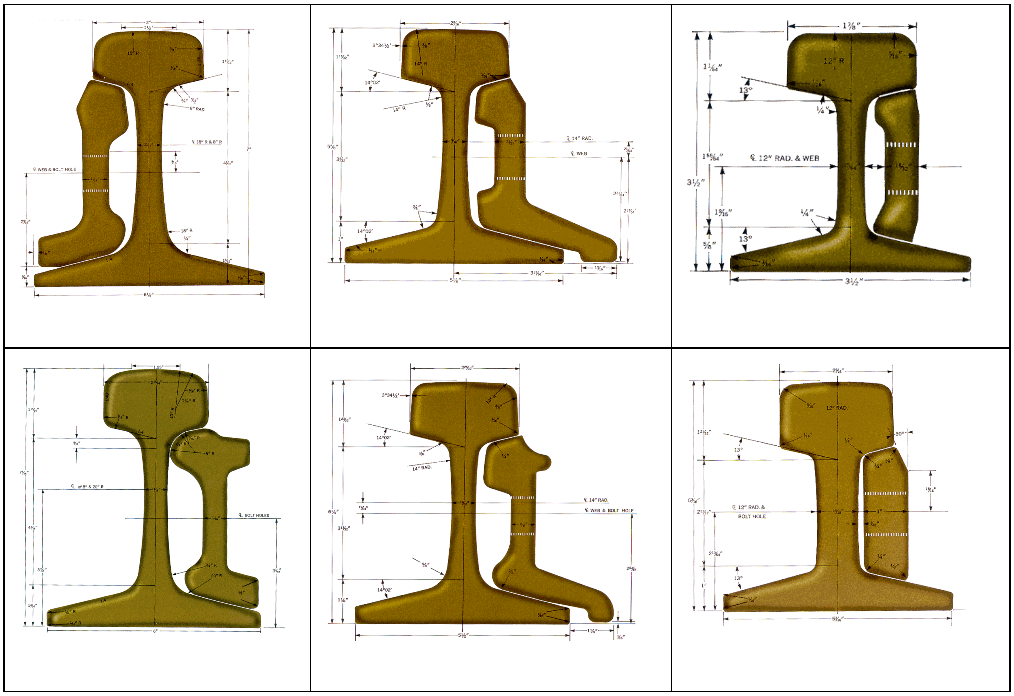

Figure 2.5 Different joint bar designs (AKRailroad, 2006)

The 6-bolt joint bar and 4-bolt joint bar are the two most common designs; a 4-bolt joint bar is shown in Fig 2.1 and a 6-bolt joint bar is shown in Fig. 2.6. The 6-bolt joint bars are obviously longer than the 4-bolt joint bars.

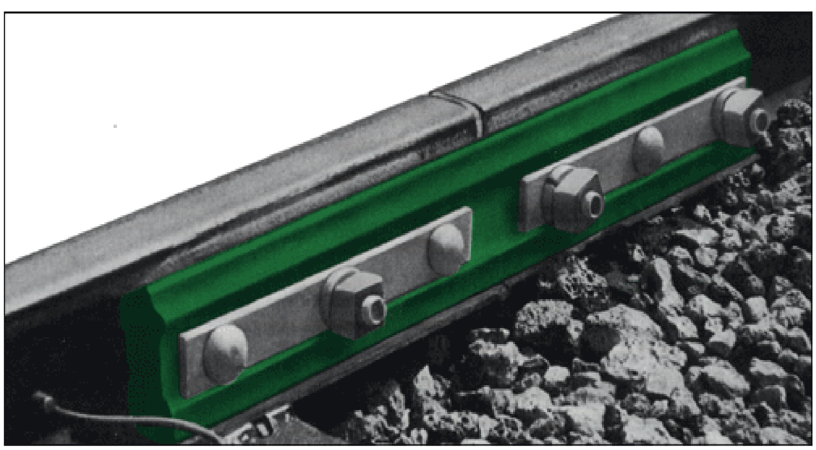

Figure 2.6 IRJ with 6-bolt joint bar (LBfoster, 2006)

Joints are also made either square or inclined to the longitudinal axis of the rails. Fig.2.7 shows examples of these types of joints.

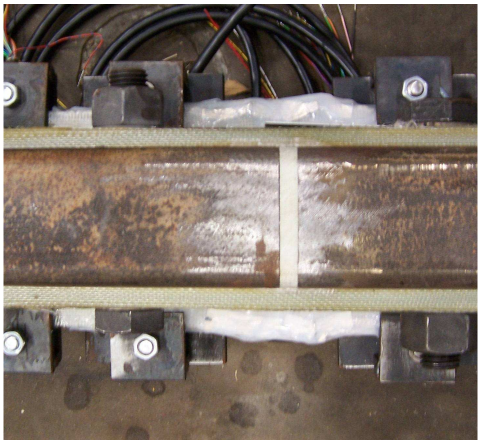

(a) Square Joint

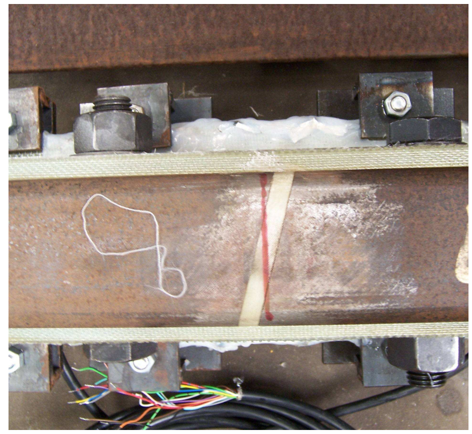

(b) Inclined Joint

Figure 2.7 Types of Insulated Rail Joints

The properties of the end post materials play an important role in the response of the IRJs. Polymer, Nylon and Fiber-glass are the commonly used IRJ insulation materials. In addition, the gap size (thickness of end post material) is also varied from 5mm to 20mm and is a key parameter for the IRJ design.

The design of IRJs also differs with the detailing of end post fitting between the rails. Glued IRJ and inserted IRJ (non-glued) end posts are two common forms employed. The glued IRJs use adhesive material such as epoxy to ensure full contact between the steel joint bars and the rail web whilst they remain electrically insulated. The inserted IRJs are a simple insert of the insulated materials into the end post gap with thermal treatment but without any adhesion material.

Some novel designs of IRJs appear in the market with a view to enhancing the structural integrity of the joints. Fig. 2.8 shows an encapsulated IRJ design used in Canada with the Polyamide 12 as the insulation.

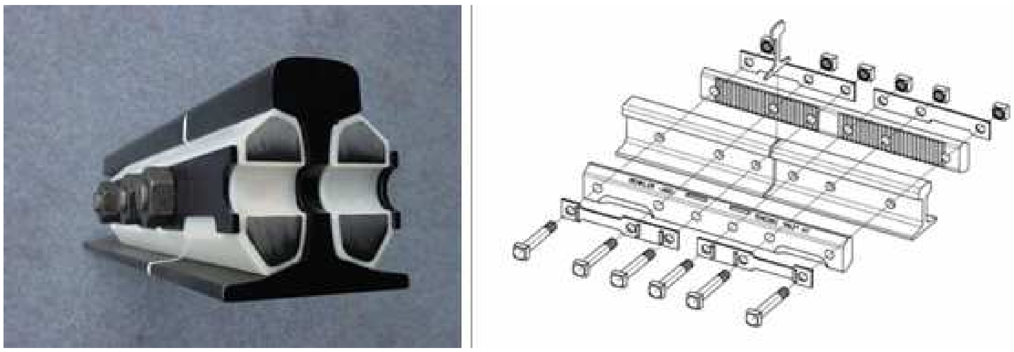

Figure 2.8 Novel design of IRJ in Canada (Nedcan, 2006)

The IRJs, like other rail circuits, are laid on the “beddings” which contains several flexible layers. Two types of tracks exist, namely, ‘conventional’ ballasted track and ‘non-ballasted’ (for example slab-track) track. Most of the Australian railway tracks are traditional ballasted and hence in this thesis only the ballasted track is chosen as the rail bedding. Referring to Fig. 2.9, IRJs are fixed to the sleepers by fasteners. The sleeper pads are inserted between IRJs and sleepers. The ballasted track substructure contains three layers: ballast, sub-ballast and subgrade. The first two layers usually consist of coarse stone chippings. The rail track superstructure and substructure together with the wheel/rail interaction constitute a complete IRJ working environment.

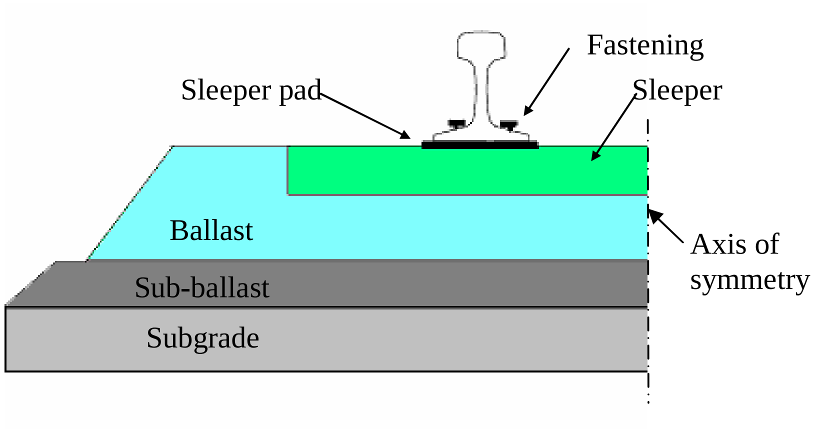

Figure 2.9 Ballasted Track

2.4. Failure of IRJs: An International Perspective

Amongst the various IRJ designs used worldwide, the failure modes of IRJs can be categorised as follows:

i) Bond failure/delamination of end post

ii) Loosening of bolts

iii) Broken joint bars

iv) Battered /crushed end posts

v) Metal flow/material fatigue on rail head

These failure modes, with one aggravating to the other, leading to a vicious circle accelerating the overall failure of IRJs. According to survey conducted by Davis (2005), the bond failure is the most common failure mode found in the heavy haul routes of North America due to high level shear stress under severe wheel loads. Fig. 2.10 presents the bond failure of the end post. The wheel/rail contact impact and the longitudinal force due perhaps to thermal effects also contribute to bolt loosening which further worsen the structural integrity and excites higher wheel/rail contact impact forces. This may consequently lead to other failure modes, namely, broken joint bars and battered/crushed end post shown in Fig. 2.11.

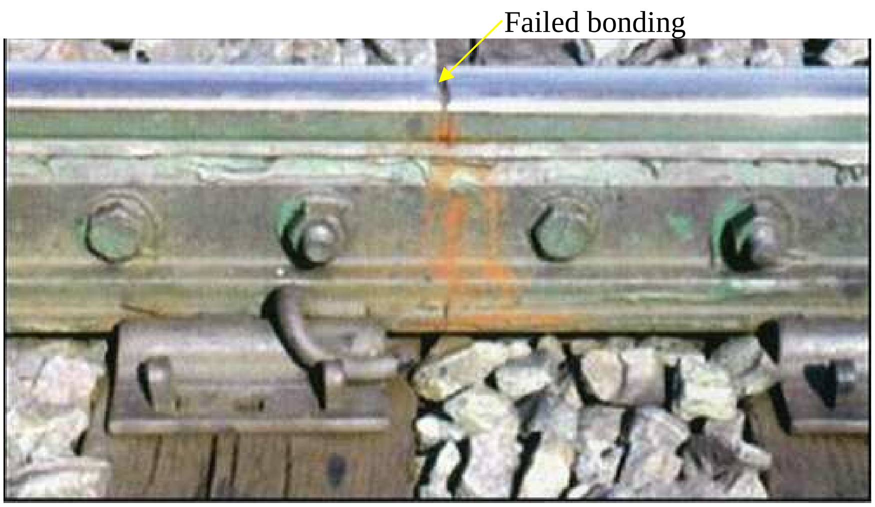

Figure 2.10 IRJ with failed glue bond (Davis, 2005)

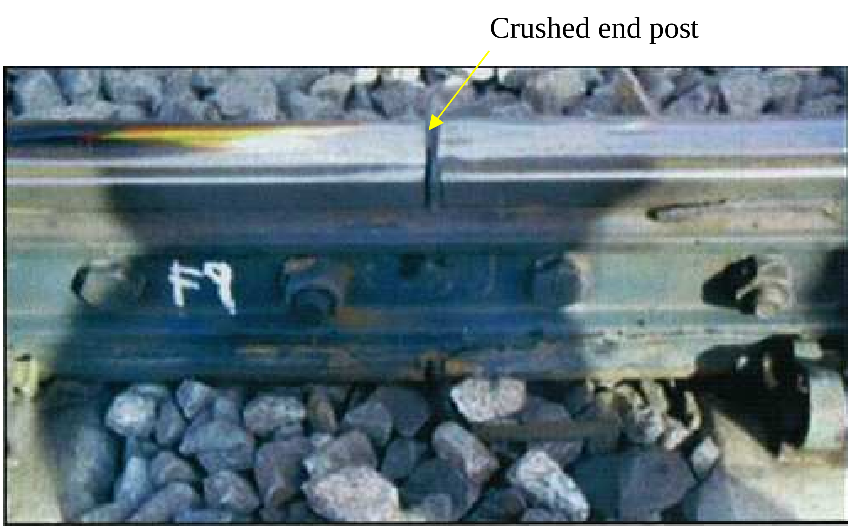

Figure 2.11 IRJ with end post crushed (Davis, 2005)

Railhead metal flow/fatigue is another failure mode that occurs if the broken joint bar or battered end post does not occur. This failure mode starts as defects on the railhead (shown in Fig. 2.12) and progresses to railhead metal failure (shown in Fig. 2.13). One of the key factors that causes this failure mode is the severe wheel/rail contact impact force and the associated rate dependent metal plasticity.

Within Australia, the railhead material failure or metal flow is the most commonly observed mode and hence is focused in this research. Fig 2.13 shows the material failure in the vicinity of the end post. It exhibits railhead metal flow, which leads to contact between the rails separated by the end post, causing critical electrical isolation failure of the IRJ. It is notable that due to the material chipping out, severe geometry discontinuity is generated, which further leads to early structural failure of IRJs.

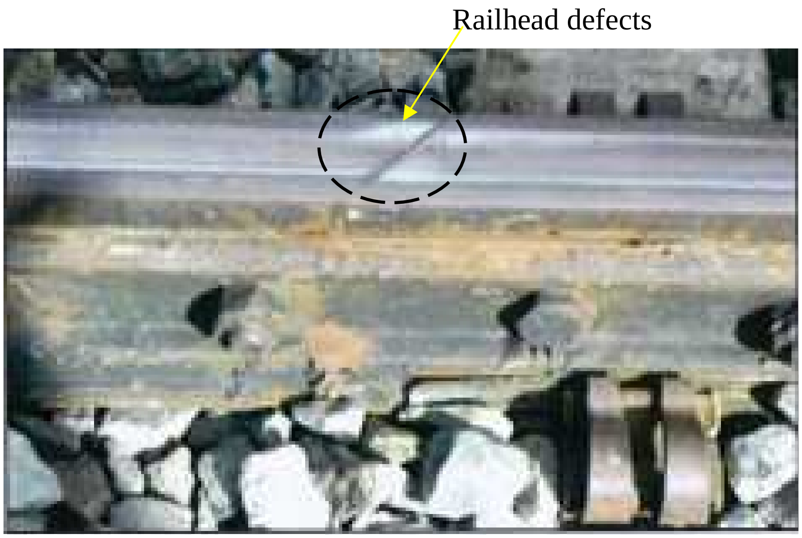

Figure 2.12 Running surface defect of IRJ (Davis, 2005)

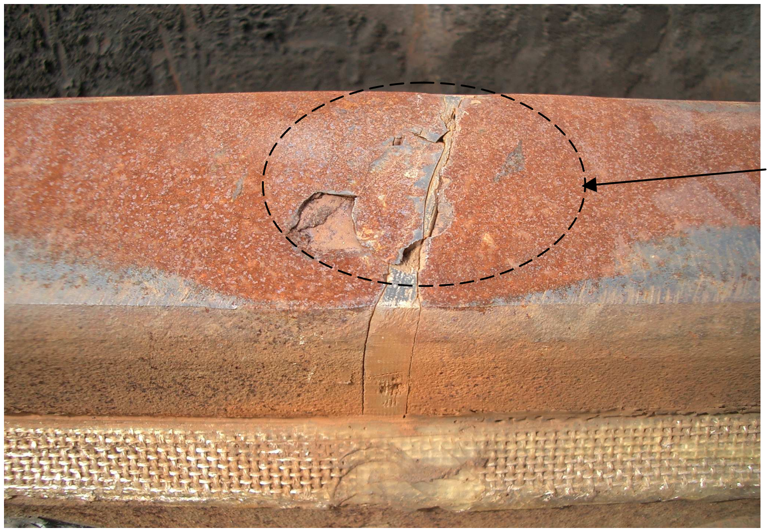

Figure 2.13 Typical IRJ failure in Australian heavy haul networks

2.5. Wheel/rail Contact-Impact at IRJs

To understand the railhead failure mechanism of the IRJs, a quantitative study of the wheel/rail contact impact is important. Many researchers have contributed their efforts to this area recently and have developed various models to investigate the wheel/rail contact impact. Static analysis is always helpful to understand the wheel/rail contact issue; as it is simple, it has been adopted by many researchers to study the IRJ characteristics. The key to investigate the wheel/rail contact-impact is however the dynamic analysis. Rigid multibody dynamics (RMD) and finite element method (FEM) are widely employed to study the wheel/rail contact-impact.

2.5.1. Static wheel/rail contact simulations

Kerr and Cox (1999) established an analytical static loading model of an IRJ. The deflection near the end post was studied using a modified beam model supported on an elastic foundation. The rail sections and joint bars were modelled as linear elastic beams, and the epoxy-fiberglass insulation was simplified as spring layers by employing the Zimmermann hypothesis. The contact load was equally distributed to both rail ends. A static loading test was conducted to validate the analytical model. The test results were found to agree well with the established analytical model. The wheel/rail contact issue was not discussed in their paper.

Yan and Fischer (2000) have carried out a static 3D finite element analysis (FEA) with three different rail models: standard rail, crane rail and a switching component. By comparing the results with the Hertz contact theory (HCT), the authors concluded that the elastic model agreed well with the HCT if the surface curvature of the rail remains unchanged. For the elasto-plastic model, it is found that their numerical results differ from the conventional HCT. The numerical results show that the contact pressure has a lower peak value but flatter distribution than the HCT if material plasticity occurs.

By establishing an elastic 3D FE rail model, Chen and Kuang (2002) carried out a static analysis of an IRJ subjected to vertical wheel loadings. They found that the traditional HCT was not valid for predicting the contact pressure distribution near the joint. The idealised elliptical contact dimensions were also listed to point out the differences with the HCT predictions.

Chen and Chen (2006) presented a 2D static FE model that was used to study the effect of an IRJ on the wheel/rail normal and tangential contact pressure distribution.

Contact elements were used to simulate the wheel/rail interaction behavior. In their model, different traction and braking forces were applied to investigate the contact pressure and maximum shear stress distribution in the railhead. Their conclusion was that the Hertz theory was not valid near the IRJ due mainly to edge effects.

Chen (2003) also investigated the material elastic-plastic effect to the IRJ under static loading using a 2D static wheel/rail contact model and concluded that the elastic model agree well with the HCT as the contact position from the rail edge over HCT half contact length exceeded 1.5. However, the elasto-plastic model indicated a disparate result that the peak pressure had a smaller value (around 70% of HCT) compared to the elastic model or HCT. With the wheel moving towards the rail end, the Von-Mises stress, plastic zone size increases gradually whilst the contact area and the peak contact pressure decrease.

Wiest et al.(2006) compared four different wheel/rail contact models at a rail turnout to examine the Hertz elastic half-space contact assumptions. Hertzian contact method, non-Hertizan contact method, elastic finite element analysis and elasto-plastic finite element analysis were conducted. The wheel and the rail switch were modelled in the finite element analysis and ‘master-slave’ contact surfaces from ABAQUS /Standard were adopted to solve the wheel/rail interaction. The results showed that the elastic finite element method agreed well with the Hertzian and non-Hertzian method in terms of contact area, peak contact pressure and penetration depth. The results of the elasto-platic finite element model differed to the other three models with a much larger contact area and smaller peak contact pressure.

2.5.2. Dynamic wheel/rail contact simulations using rigid multibody dynamics

For the dynamic analysis of IRJs, rigid multibody dynamics were widely employed in the IRJ studies. Jenkins et al. (1974) studied the dipped rail joints using the rigid body dynamic methods. They modelled the dipped rail joint as a dipped continuous beam supported by sets of springs and dashpots at the location of sleepers. Contact between wheel and railhead is assumed to be of HCT. They predicted the dynamic contact force factors (defined as the ratio of dynamic to static force) between the rail and the wheel at the assumed dipped joints, and found that there existed two contact force factors: the first being a high amplitude (5~6) and high frequency peak (500Hz), and the second a low amplitude (3~4) and low frequency peak (30~100Hz). The first peak damps out in a few milliseconds and affects only the local contact area. The second peak damps slowly and affects most track and wagon components.

Newton and Clark (1979) also studied the rail/wheel dynamic interaction in both experimental and theoretical methods. The contact/impact between the wheel and the rail introduced by wheel flats rolling over the railhead was researched and a comparison of an experiment and theoretical results was carried out. The experiment used an indentation on the railhead and strain gauges were used to measure the strain history. The theoretical model considered the sleeper pad as a spring and dashpot layer, sleepers as a mass layer, and ballast as another spring and dashpot layer resting on a rigid foundation. It was shown that the dynamic effects of wheel flats strongly depend on the rail pad stiffness and the speed regime.

Sun and Dhanasekar (2002) developed a whole wagon and rail track multibody dynamics model to investigate the dynamic rail-vehicle interactions. The rail track was modelled as a four layer sub-structure and the non-linear Hertz spring was employed for the contact mechanism. Several idealised wheel/rail irregularities were imposed as the dynamic load excitations. The results were validated by several published models and experiments, and good agreements were achieved.

Wu and Thompson (2003) developed an efficient dynamic rail wheel contact model for rail joint impact noise analysis. Rail and wheel, which were assumed as elastic bodies, were connected to each other using the Hertz non-linear spring allowing a loss of contact. The wheel centre trajectories were employed to model the dipped joint. The rail foundation was modelled as discrete double layer system with spring, mass and damping parameters to model the pad, sleeper and ballast characteristics. Gap size, vertical misalignment and dip of rail joint were studied. The impact force was shown to have 400%~800% of static load at certain conditions for various velocities and depths of joint dip.

Steenbergen (2006) reported a theoretical 'multi-point contact' wheel/rail model by multibody dynamics to investigate the contact spatial discontinuity in his paper. Through a comparison with the common practical 'continuous single point contact' model which employs the Hertz nonlinear spring as the contact parameter, the author concluded that by using the 'continuous single point contact' the possibility of impact would be automatically excluded and that the situation can be improved by introducing the vertical velocity change to the wheel mass when 'double point contact' occurs. However, the rail irregularities such as the IRJs are treated as steps and kinks, which may not be easy to apply to IRJs without permanent deformations (such as new IRJs).

Recently many researchers developed efficient approaches which coupled rigid multibody dynamics with FEM to study the rolling fatigue, railhead crack and metal plastic flow at the wheel/rail contact surface irregularities which need a strain and stress analysis. The rigid multibody dynamics models were developed to investigate the wheel/rail dynamic contact force. The results were then transferred into the finite element model for the detailed strain and stress analysis to investigate the railhead damage.

Bezin et al. (2005) introduced an approach which coupled a multibody system model and a finite element model together to conduct a rail stress analysis. In this research, a whole wagon/rail multibody dynamics model was developed using ADAMS/Rail. The generated dynamic force was then transferred into a global FE model setup using ABAQUS as the loading condition. In this global FE model, the bending stress and strain of rail and sleeper components established with elastic Timoshenko beam and spring elements were obtained via a static analysis. A local 3D solid finite element contact model was established to study the contact pressure and stress distribution which was essential to predict the crack initiation and growth. The contact position and force were also transferred from the multibody dynamics model. The dynamic force validation was also carried out by comparing with some field measurements and good agreement was achieved.

Busquet et al. (2005) reported a quasi-static finite element analysis of the railhead plastic flow due to wheel/rail rolling contacts. The contact force and load distribution was generated via a multibody dynamics model which employed the Hertzian and Kalker (Chollet, 1999) contact theory. The dynamic results were then transferred into the refined 3D solid rail model to calculate the metal plastic flow. No contact surface irregularity was concerned in this research.

With assumption that the contact bodies are rigid, the rigid multibody dynamics has the advantage of simplification of calculation and hence is widely adopted to study the wheel/rail dynamic interactive behaviour. However, because the HCT is employed in the rigid body method, its application to this research is difficult as the material plasticity and discontinuous running surface are involved.

2.5.3. Dynamic wheel/rail contact simulations using finite element method

In recent years, some simplified finite element models have employed beam elements to model the wheel/rail dynamic contact behaviour. In these models the HCT was adopted for the wheel/rail vertical interaction and the rail was modelled with beam elements. Andersson and Hahlberg (1998) studied the wheel rail impact at turnout crossings using a finite element model. Trains were considered as discrete masses, springs and dampers system and Rayleigh-Timoshenko beam elements were employed to simulate the rails and sleepers supported by an elastic foundation without any damping. Hertz contact spring was applied for the rail/wheel interaction. Single wheel, half bogie and full bogie models were set up for comparison. Two key factors for impact force of the crossings, rail flexibility difference and transition irregularity were investigated. The transition irregularity was idealised as a trough shaped beam. Results showed that when the transition irregularity was ignored, an impact force from 30%~50% of static load would be achieved while the impact factor varied from 100%-200% if the irregularity was considered. The contact force increased non-linearly with the increase in train velocity.

Dukkipati and Dong (1999) studied the dip-joint problem employing a discretely supported finite element rail model. Multi-spring contact was adopted as the wheel/rail interaction and the joint was modelled with Timoshenko beam elements. Both wheel set and bogie structure were considered for the vehicle model. The simulation was validated by comparing its dynamic forces with some experimental results. It was found that the mass of the whole wagon system shared by the wheel and rail equivalent mass had a significant influence on the P1 force, while unsprung wheel mass and foundation stiffness affected the P2 force significantly.

Koro et al. (2004) established a dynamic finite element model to investigate the edge effects of rail joint. A modified constitutive relation of Herzian contact spring (Kataoka, 1997) was adopted to model the wheel/rail contact. Timoshenko beam elements were used to model the joint structures including the joint bars. Tie springs were employed to connect the joint bars to the rail supported on a discrete elastic foundation. Special attention was paid to the geometry discontinuity at the concentrated loading position using modified double node Timoshenko beam elements. Gap size and train speed effects on impact force were carefully investigated.

The results showed that for velocities lower than 150Km/h, impact force was sensitive to the gap size while the train speed only had a minor influence.

Wu and Thompson (2004) studied the track non-linear effect for wheel/rail impact analysis. A wheel flat was considered as the impact source and a Hertzian contact spring was employed for the wheel/rail interaction. The track was modelled using a finite element method with beam elements supported by non-linear track foundation. The results showed that the pad stiffness affects the impact amplitude significantly.

The 3D dynamic FE model has been employed recently to investigate the wheel/rail contact behaviour with the development of improved computing capabilities. Wen et al (2005) performed a dynamic elasto-plastic finite element analysis of the standard rail joints containing a gap and joint bars. They employed a coupled implicit-explicit technique that imported the initial steady state implicit solution prior to impact into the explicit solution to determine the impact dynamic process. They have reported that the impact load varies linearly with the static axle load but is largely insensitive to the speed of travel of the wheel. The impact force history presented in their paper exhibited *three peaks*, which were difficult to comprehend given the model allowed for only a single wheel.

Wiest et al. (2006) developed a FE model to study the crossing nose damage due to wheel/rail impact. A dynamic model was established to simulate the wheel passing over the crossing nose. The dynamic behaviour of the wheel was idealised as pure rolling and the rail supporting system was considered as rigid. The cyclic calculation was carried out to study the dynamic response and material flow of the rail nose. A quasi-static sub-model was employed after the dynamic analysis to further study the stress and strain evolution. Two different railhead materials, manganese and composite, were carefully studied for the material plastic flow.

Li et al. (2006) developed a full-scale 3D finite element model for wheel/rail contact dynamic analysis on rail squats. A single wheel and rail were modelled with solid elements and contact elements were used for the contact modelling. The rail squats were studied as the contact surface irregularity, and a two-layer discrete support system was employed as the rail foundation. The dynamic contact force time series matched well with field measurements. Material strength, unsprung mass, traction and braking, sleeper spacing and fastening system property played an important role on the dynamic effect.

2.6. A Hypothesis for the Failure of Australian IRJs

There are two key factors that lead to the failure of IRJs:

i) Wheel/rail contact-impact force

ii) Material ratchetting

The wheel/rail contact-impact force is excited by the IRJ structural/geometry discontinuity. Under severe wheel/rail loading, the material retchetting/fatigue is initiated and causes metal flow on the railhead. The initiation and progression of the failure is considered concentrated on the railhead in the vicinity of end post. It is worth noting that, although the wheel/rail interaction force has components in both the vertical and the horizontal planes, the vertical contact-impact force is believed to play the major role. This failure mechanism of IRJs has been widely acknowledged by Australian practioners. As part of a project to study this failure mechanism of IRJ, this thesis focuses on the investigation of wheel/rail contact/impact forces; the material ratchetting issue is covered in another ongoing PhD thesis, using the impact load and contact pressure obtained from this thesis as the input loading.

The wheel/rail contact impact mechanism hypothesis is shown in Fig. 2.14. Because of the difference in modules between the end post material and steel, as well as their connection (glued or non-glued), structural discontinuity exists. As the wheel approaches the joint, an IRJ running surface discontinuity is momentarily generated which forms a recoverable ‘dipped’ joint. The wheel then ‘flies’ over the end post gap and ‘lands’ on the Rail 2 (see Fig. 2.14) and generates the impact. At the time of impact, the wheel exhibits ‘two-point contact’ due to the dipped joint.

2.7. Summary

The FE method is widely employed for static wheel/rail contact models. By incorporating the material plasticity and edge effects to the wheel/rail contact behaviour, these models draw a conclusion that at the vicinity of the end post, the Hertz Contact theory (HCT) is not valid to model the wheel/rail interaction in the vicinity of the end post.

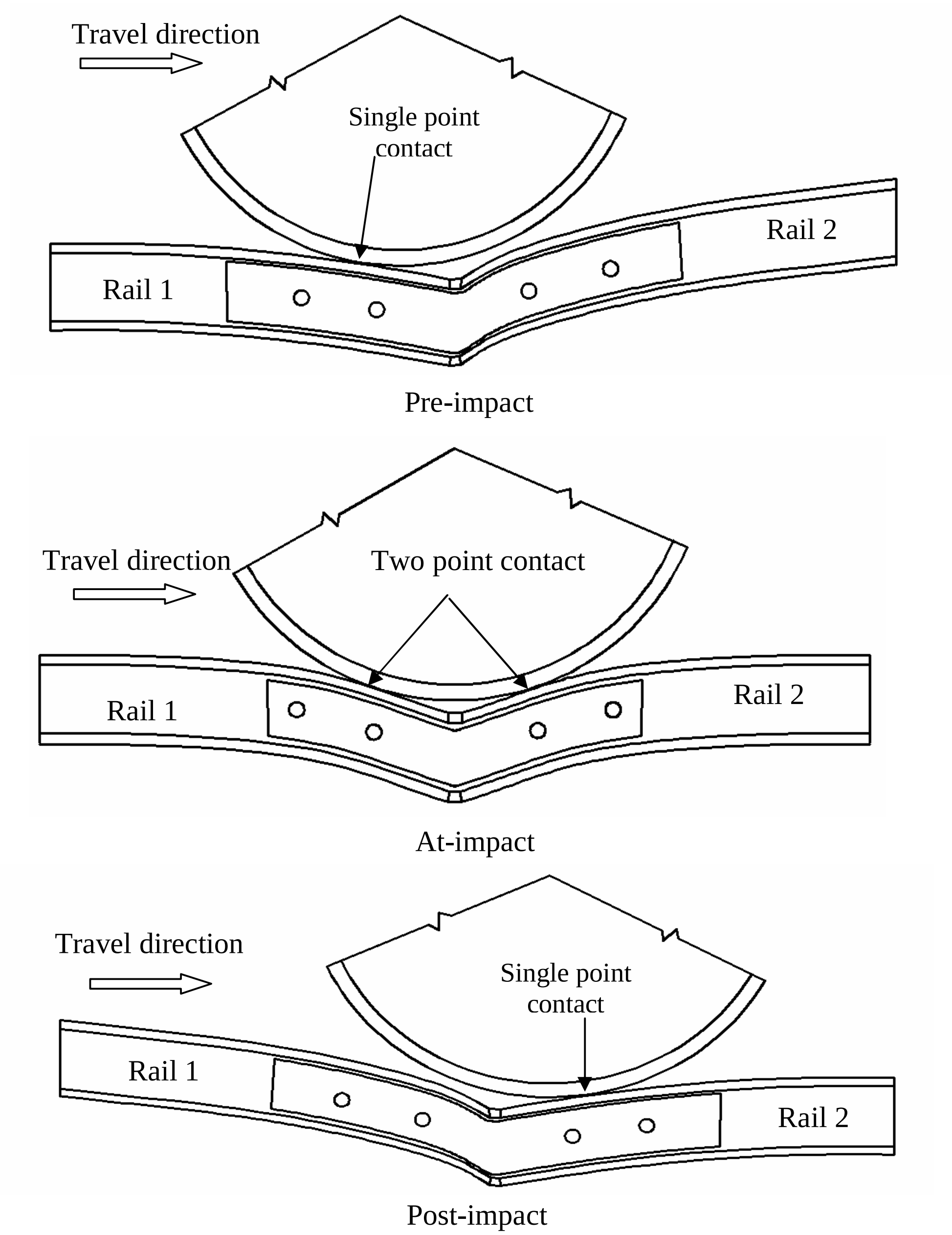

Figure 2.14 Wheel/IRJ contact impact hypothesis

For the dynamic analysis, there are two major methods employed by rail engineering researchers: RMD and FE method. For the conventional RMD models, the wheel/rail vertical contact behaviour is mostly described as ‘single point contact’ and governed by HCT. The structural imperfections of IRJs are usually idealised as surface defects.

This approach is believed to be improper to predict the wheel/rail impacts dominated by 'multi point contact' at IRJs. The treatment of IRJ structural discontinuity is also questionable as the 'new' IRJs have instantaneous dips under wheel passages but no permanent defects.

With the development of improved computing facilities, the finite element method is increasingly being adopted for 3D wheel/rail dynamic contact modelling at IRJs and other wheel/rail imperfections. The wheel/rail interactions are solved by numerical methods without any assumptions of the contact behaviour as a priori. The capability of modelling the material plasticity and practical mechanical structure makes the FEM the preferred choice for this research.

This chapter has also provided a general review of IRJ designs and failure mechanisms. A hypothesis for railhead failure is presented and relevant literature reviewed.

The theoretical basis for the analysis of contact impact is described in Chapter 3. A FE model for contact-impact analysis of IRJs is developed in Chapter 4 and results provided in Chapter 5.

3. Theory of Contact-Impact

3.1. Introduction

This chapter reports the mechanics of contact and the theory of the finite element method. Both the classical and the computational theories of contact mechanics are reviewed first, followed by the solution methods for FEM. The techniques of FE modelling of contact impact are also presented.

3.2. Brief Review of Mechanics of Contact

3.2.1. Classical theories

Contact is one of the common research topics because of its wide applications in the engineering field. The earliest theory of contact mechanics is due to the pioneering researcher Heinrich Hertz who published a classical paper on contact in 1882 in the German language. Subsequently several researchers improved the Hertz contact theory by relaxing the limitations and extending its application to more practical situations.

(a) Normal contact of elastic solids – Hertzian contact theory

Hertz contact theory (HCT) is established based on some basic assumptions: elastic contact bodies, frictionless contact surfaces, continuous and non-conforming surfaces, small strains and small contact area relative to the potential area of contacting surfaces (Johnson, 1985) .

Fig. 3.1 shows two non-conforming solids (Body 1 and Body 2) which contact at an area that is finite and small compared to their dimensions. Assuming that the profile of each surface is topographically smooth in both micro and macro scales, the profiles of the contacting bodies are expressed in Eq. (3.1) and (3.2).

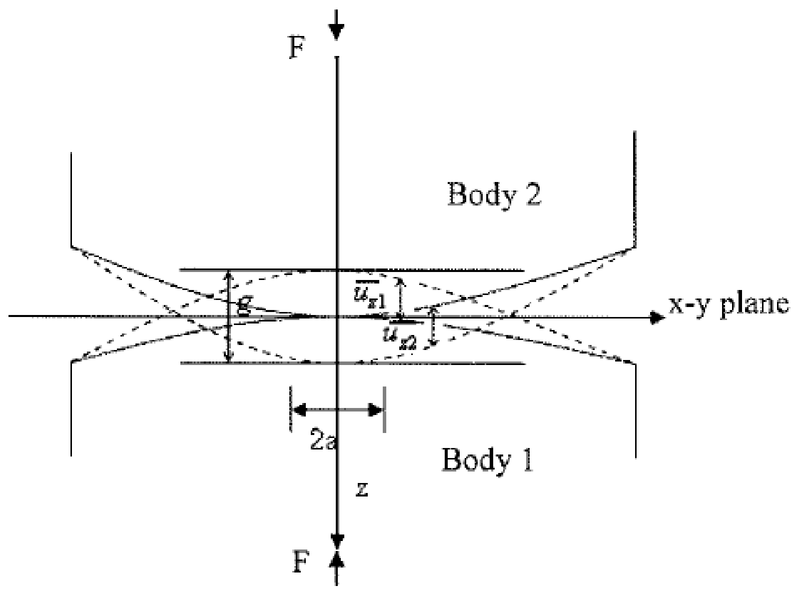

Figure 3.1 Contact between non-conforming solids

$$Z_1 = \frac{1}{2R_1^{'}} x^2 + \frac{1}{2R_1^{''}} y^2 \tag{3.1}$$

$$Z_2 = -(\frac{1}{2R_2^{'}} x^2 + \frac{1}{2R_2^{''}} y^2) \tag{3.2}$$

The separation between the two surfaces is then calculated as follows:

$$g = Z_1 - Z_2 = \frac{1}{2R^{'}} x^2 + \frac{1}{2R^{''}} y^2 \tag{3.3}$$

where $\begin{cases} \dfrac{1}{R_1^{'}} + \dfrac{1}{R_2^{'}} = \dfrac{1}{R^{'}}, \\ \dfrac{1}{R_1^{''}} + \dfrac{1}{R_2^{''}} = \dfrac{1}{R^{''}} \end{cases}$.

Defining the $\overline{u_{z1}}$ and $\overline{u_{z2}}$ as the displacements of points on each surface and g as the compression displacement of two bodies, when points are in the contact area, the following expression can be written:

$$\overline{u_{z1}} + \overline{u_{z2}} = g - \frac{1}{2R^{'}}x^2 - \frac{1}{2R^{''}}y^2 \tag{3.4}$$

If Eq. (3.4) is not satisfied (as in Eq. (3.5)), the bodies are said to be separated.

$$\overline{u_{z1}} + \overline{u_{z2}} < g - \frac{1}{2R^{'}}x^2 - \frac{1}{2R^{''}}y^2 \tag{3.5}$$

In Eq. (3.4) and (3.5), $\overline{u_{z1}}$ and $\overline{u_{z2}}$ are obtained implementing the elasticity theory with the contact pressure P that is yet to be determined:

$$\begin{aligned} \overline{u_{z1}} &= \frac{1-\nu^2}{\pi E}\iint \frac{p(x,y)}{R}dxdy, \\ \overline{u_{z2}} &= \frac{1-\nu'^2}{\pi E'}\iint \frac{p(x,y)}{R}dxdy \end{aligned} \tag{3.6}$$

Inserting Eq. (3.6) into Eq. (3.4), an integral equation is obtained employing potential theory. The resulting pressure distribution is then worked out as:

$$p(x,y) = \frac{3F}{2\pi ab}\sqrt{1 - \frac{x^2}{a^2} - \frac{y^2}{b^2}} \tag{3.7}$$

where a and b represent the major and minor axes respectively of the elliptical contact zone and can be determined by resolving the following set of integral equations once the curvatures of contact surfaces R' and R'' are determined (Eq. 3.8):

$$\begin{aligned} \frac{1}{2R^{'}} &= \frac{3F}{4\pi}\left(\frac{1-\nu^2}{E} + \frac{1-\nu'^2}{E'}\right)\int_0^\infty \frac{d\zeta}{(a^2+\zeta)\sqrt{(a^2+\zeta)(b^2+\xi)\zeta}}, \\ \frac{1}{2R^{''}} &= \frac{3F}{4\pi}\left(\frac{1-\nu^2}{E} + \frac{1-\nu'^2}{E'}\right)\int_0^\infty \frac{d\zeta}{(b^2+\zeta)\sqrt{(a^2+\zeta)(b^2+\zeta)\zeta}} \end{aligned} \tag{3.8}$$

The analytical solution of contact dimensions and pressure distributions between two smooth elastic bodies is obtained through the above process. This problem is strictly nonlinear because the displacement at any point of contact depends on the distribution of contact pressure throughout the whole contact zone. This leads to a significant complexity to solve the integral equations of contact pressure for each step in the dynamic contact condition. As a simplification, the ‘Hertz contact spring’ is developed. Assuming a simple Winkler elastic foundation rather than elastic half space, the model is illustrated in Fig. 3.2 which shows an elastic foundation resting on a rigid base and contacted with a rigid indenter.

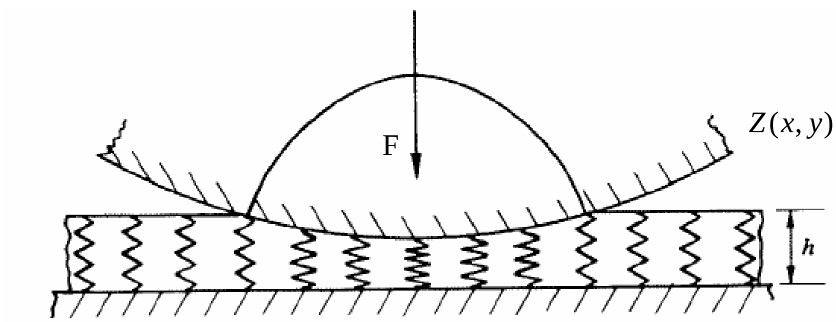

Fig 3.2 Hertz contact foundation model (Johnson, 1985)

Using the profile of the indenter $Z(x,y)=\frac{1}{2R^{'}}x^2+\frac{1}{2R^{''}}y^2$ and the original compressed displacement g, the displacement profile of the contact surfaces is written as:

$$\overline{u_z}(x,y)=\begin{Bmatrix} g-Z(x,y), g>Z \\ 0, g<Z \end{Bmatrix} \quad (3.9)$$

The contact pressure at any point is assumed to be dependent only on the displacement at that point as in Eq. (3.10).

$$p(x,y)=(K/h)\overline{u_z}(x,y) \quad (3.10)$$

Inserting Eq. (3.9) into Eq. (3.10), the pressure distribution is expressed as:

$$p(x, y) = (K / h)(g - \frac{1}{2R^{'}} x^2 + \frac{1}{2R^{''}} y^2) \tag{3.11}$$

By integrationof the pressure distribution the total contact force is obtained as:

$$F = K\pi g^2 \sqrt{R^{'} R^{''}} / h \tag{3.12}$$

where h is the depth of elastic foundation. The relationship of contact force and contact indention is thus generated.

(b) Non- Hertz normal contact of elastic bodies

HCT application to practical problems is limited due to its assumption of strict smooth elastic half space. To solve practical problems, non-Hertz normal contact solutions are, therefore, developed. For the wheel/rail contact at IRJs, the Hertzian assumptions are violated because of edge effect, discontinuous surface profile and interface frictions; Hertz solutions are therefore not strictly applicable for contact problems at IRJs.

(i.) Edge effect

The HCT half space assumption is violated for problems encountering contact at non-continuous profiles such as the edge of bodies. Many researchers have examined the edge effect in recent decades (Dundurs & Lee (1972), Gdoutos & Theocaris (1975), Comninou (1976), Bogy (1971), Khadem & O'Connor (1969)). Unfortunately analytical solutions are not possible, with the problems requiring idealisations or gross simplifications.

A rigid punch with a square corner was considered as a case of non-Hertzian contact theory as the edge of the punch was not continuous. These tilted punch problems were solved by Muskhelishvili (1949). The pressure distribution close to a corner ($s = a - x << a$) can be expressed as:

$$p(s) = \frac{2(1-\nu)}{\pi(3-4\nu)}(2as)^{-1/2}\cos\{[(1/2\pi)\ln(3-4\nu)]In(2a/s)\} \qquad (3.13)$$

where s is the distance from the contact edge corner and a is the contact patch dimension.

Furthermore general edge problems that contain angles at corners other than 90° were considered by Dundurs & Lee (1972) for frictionless contact and by Gdoutos & Theocaris (1975) and Comninou (1976) for frictional situations and by Bogy (1971) for no slip.

(ii.) Discontinuous surface profiles

When there is curvature change within the the contact area, the Hertz continuous surface assumption is violated. The geometries of edge effect problems are idealised as a wedge or cone to formulate analytical solutions. The pressure distribution was given in Johnson's (1985) book as:

$$p(x) = \frac{E^* \cot\alpha}{2\pi}\ln\{\frac{a+(a^2-x^2)^{1/2}}{2}\} = \frac{E^* \cot\alpha}{\pi}\cosh^{-1}(a/x) \qquad (3.14)$$

where $\frac{1}{E^*} = \frac{1-\nu^2}{E} + \frac{1-\nu'^2}{E'}$ and α denotes the semi-angle of the wedge or cone.

Love (1939) used the indentation of a flat surface by a blunt cone and gave similar results. Similar work has also been done by Sneddon (1948) and Spence (1968). However, the analytical solution for problems defined with generalised contact profiles is not yet found in the literature.

(iii.) Interface friction

The interface friction is inevitable in practical situations. In the normal direction, the material elastic deformation in the tangential plane causes traction even without any relative tangential movements. However, this is only applicable to the cases that deal with contacting bodies made of different materials. Johnson (1985) has maintained that the relationship for the normal pressure and traction ($q = \mu p$) still is valid for the slip case. For stick situations, Mossakovski (1954,1963) and Goodman (1962) studied this using a 2D problem firstly, and Spence (1968) improved their findings to show that under appropriate conditions the stress field is self-similar at all stages of loading. The traction distribution $q(x)$ is given as:

$$q(x) = \frac{\beta p_0}{\pi a}[(a^2 - x^2)^{1/2} \ln\left|\frac{a+x}{a-x}\right| + x \ln\{\frac{a+(a^2-x^2)^{1/2}}{a-(a^2-x^2)^{1/2}}\}] \tag{3.15}$$

where β represents the measure of difference between the elastic materials of the two elastic bodies and can be calculated as in Eq. (3.16):

$$\beta = [\frac{\{1-2\nu/G\} - \{1-2\nu'/G'\}}{\{1-\nu/G\} + \{1-\nu'/G'\}}] \tag{3.16}$$

where G is the shear modulus.

In summary, although the theory of classical contact mechanics is widely used in the study of wheel/rail contact, the limitation imposed by the basic assumptions and the difficulty to obtain the analytical solution introduce significant challenges to the specific problem of contact impact at IRJs. This is because classical contact mechanics, especially Hertz contact theory, does not account for the edge effect and material plasticity. Although several non-Hertz contact solutions are proposed in the literature, analytical solutions for more general cases are not yet available and hence, their application to railway engineering still remains far from being realised.

3.2.2. Computational theories

Computational contact mechanics is developed on the basics of non-linear continuum mechanics by employing numerical methods such as the finite element method. The contact is considered as a boundary condition. In this section, the basis of the finite element method is reviewed prior to presenting the computational contact theory.

(a) Basics of finite element method

Zienkiewicz (1971) has provided a displacement approach to solve the generalised elastic continuum problems numerically as described below:

i. *The continuum is separated by imaginary lines or surfaces into a number of 'finite elements'.*

ii. *The elements are assumed to be interconnected at a discrete number of nodal points located on their boundaries. The displacements of these nodal points are the basic unknown parameters of the problem.*

iii. A set of functions are chosen to define uniquely the state of displacement within each 'finite element' in terms of its nodal displacements.

iv. The displacement functions define uniquely the state of strain within an element in terms of nodal displacement. These strains, together with any initial strains and constitutive properties of material will define the state of stress throughout the element and, hence, also on its boundaries.

The finite element method introduces some approximations to the solution. The first is the displacement function which only approximately represents the displacement profile of the elements. The second relates to equilibrium conditions that are satisfied to within a prescribed level of tolerance.

The process of solving the equilibrium condition is equivalent to the minimisation of total potential energy of the system in terms of the prescribed displacement field. Therefore, finite element method applications can be extended to almost all problems where a variational formulation is possible.

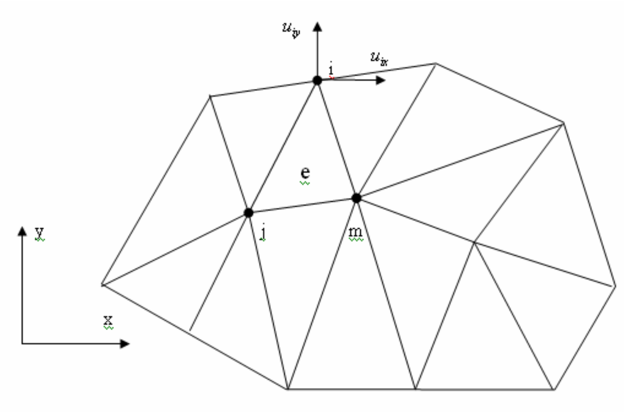

Figure 3.3 2D discrete plane with elements

For simplicity a two dimensional plane stress analysis formulation is provided here. In Fig. 3.3, a typical finite element, e, is defined by nodes, i, j, m and straight line boundaries. The displacement field within this element at any point can be represented as:

$$u = Nu_e \tag{3.17}$$

where N is the shape function and u_e represents the nodal displacement for an element. The strain-displacement relations are then expressed as:

$$\varepsilon = Bu_e \tag{3.18}$$

Matrix B is strain-displacement transformation matrix. Stresses are determined from:

$$\sigma = D\varepsilon \tag{3.19}$$

where D is the elastic matrix.

By imposing a virtual nodal displacement du_e, equilibrium with the external and internal work is achieved. Eqs. (3.17) and (3.18) are then rewritten as:

$$du = Ndu_e, d\varepsilon = Bdu_e \tag{3.20}$$

The work done by the nodal forces is the sum of the products of the individual force components and the corresponding displacement,

$$\Pi_{ext} = (du_e)F_e \tag{3.21}$$

where F_e is the nodal force.

In the same way, the internal work per unit volume done by stresses and body forces is worked out as:

$$\Pi_{\text{int}} = (d\varepsilon)\sigma - (du)f \tag{3.22}$$

or

$$\Pi_{\text{int}} = (du_e)(B\sigma - Nf) \tag{3.23}$$

in which f is the body force.

Employing the virtual work principle that equates the external work to the total internal work, Eq. (3.24) is obtained:

$$(du_e)F_e = (du_e)(\int B\sigma dxdy - \int Nfdxdy) \tag{3.24}$$

When the material elasticity is valid, substituting Eqs. (3.18) and (3.19) into Eq.(3.24), the following equation can be obtained:

$$F_e = \int (B^T DBdxdy)u_e - \int Nfdxdy \tag{3.25}$$

In Eq. (3.25), $k^e = \int B^T DBdxdy$ is the matrix of element stiffness. F_e is a set of unknown parameters. In order to determine the displacement field u_e, boundary conditions must be employed to resolve these equations at the overall system level.

The stiffness of the whole system is obtained by assembling the stiffness matrices of all elements together.

$$K = \sum k^e \tag{3.26}$$

The principle of virtual displacement used above ensures the equilibrium of the system for the displacement pattern that minimises the potential energy. The equilibrium would be complete only if the virtual work equality for all arbitrary variations of displacement were ensured.

Balancing the internal energy with the external work, Eq. (3.27) is obtained:

$$\int (d\varepsilon)\sigma dV - [\int (du)\, fdV + \int (du)\, f_b dS] = 0 \qquad (3.27)$$

The first term of the above equation will be recognized as the variation of the strain energy, Π_{int} of the structure, and the second term that is in the brackets is the variation of the potential energy of external loads, Π_{ext}.

Rewriting Eq. (3.27), we obtain:

$$d(\Pi_{int} + \Pi_{ext}) = d(\Pi_p) = 0 \qquad (3.28)$$

where Π_p is the total potential energy. This means the finite element method seeks a displacement field that keeps the total potential energy stationary and minimised. In that case, finite element method can be used in any problem in which function Π_p could be specified or in the following minimum condition:

$$\frac{\partial \Pi_p}{\partial u} = \begin{Bmatrix} \dfrac{\partial \Pi_p}{\partial u_1} \\ \dfrac{\partial \Pi_p}{\partial u_2} \\ \vdots \\ \end{Bmatrix} = 0 \qquad (3.29)$$

In practical application, the equilibrium equations can be obtained by descretising the virtual work equation and expressed as:

$$F(u) = 0 \tag{3.30}$$

The displacement field can be obtained by solving Eq. (3.30), and other terms such as the strain and the force are derived from the obtained displacement.

So far the finite element process to the linear elastic problem is introduced. However, in this thesis, because of the material plasticity and contact boundary condition, the non-linearity is involved. Thus the approach is generalized to accommodate the non-linear problems. Galerkin Treatment is commonly used as a weighted residual method to the general finite element process. On top of that, the weak form of the differential governing equations is introduced first. The governing equations are written in the general form as:

$$H(u) = \begin{Bmatrix} H_1(u) \\ H_2(u) \\ \vdots \end{Bmatrix} = 0 \tag{3.31}$$

In a domain Ω, with the boundary conditions

$$J(u) = \begin{Bmatrix} J_1(u) \\ J_2(u) \\ \vdots \end{Bmatrix} = 0 \tag{3.32}$$

The equivalent weak-form is expressed as

$$\int wH(u)d\Omega + \int \overline{w}J(u)d\Gamma = 0 \tag{3.33}$$

Where w and $\overline{w}$ are arbitrary parameters called weighted coefficient. Eq.(3.33) is called the weakform of Eq.(3.31) and Eq.(3.32) with lower requirement of connectivity for displacement function.

The solution in approximation form is written as following:

$$u \approx \sum N_i d_i = Nd \tag{3.34}$$

Where d is the nodal displacement field. The approximation to the Eq. () is written as:

$$\int wH(Nd)d\Omega + \int \overline{w}J(Nd)d\Gamma = 0 \tag{3.35}$$

The $H(Nd)$ and $J(Nd)$ represent the residual obtained by substitution of the approximation into the differential governing equations. Eq.(3.35) is a weighted integral of such residuals. The approximation thus is called the method of weighted residuals. To the weighted residual method, there are a few treatments; among which, the Galerkin method is most commonly used. The Galerkin method chooses the shape function as the weighted coefficient and written as:

$$w_j = N_j \tag{3.36}$$

As a result, in the Galerkin method, Eq.(3.37) is derived:

$$\int NH(Nd)d\Omega + \int NJ(Nd)d\Gamma = 0 \tag{3.37}$$

(b) Computational contact theory

For contact problems, the contact between two bodies is treated as a boundary condition for each body. The contact pressure and traction represented by term f_b (Eq. 3.27) are considered as boundary constraints. The Lagrange Multiplier method and the Penalty method of contact constraint enforcement are employed to solve the equilibrium equations.

Contact is a complex boundary condition because of its nonlinearity. Before employing the contact constraint enforcement to solve the equilibrium equations, the relation between contact pressure/traction and displacement needs to be set up. As the state of contact affects the relationship between the contact pressure/traction and the displacement, first the computational approach should establish the occurrence of contact. The following conditions are required to be assessed in each computational step.

$$\begin{cases} non-contact \\ contact\begin{cases} stick \\ slip \end{cases} \end{cases}$$

A potential algorithm is presented as a simple illustration. Consider Fig. 3.4 showing two elastic bodies $B^i, i=1,2$. x_i denotes coordinates of the original configuration. In the normal direction of contact, non-penetration condition is defined as gap function g_N given by:

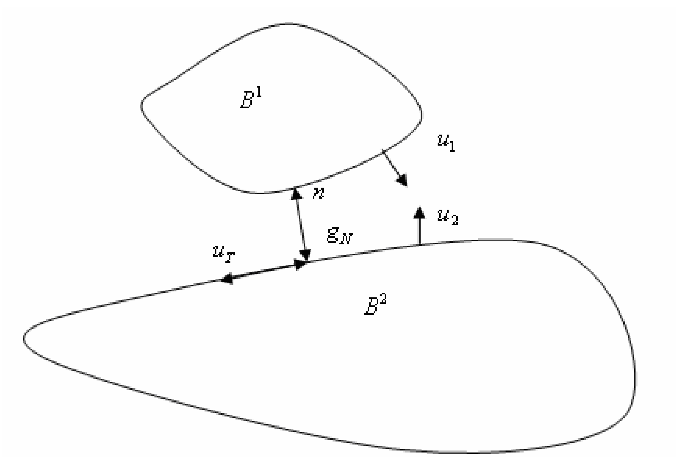

Figure 3.4 Two bodies in contact

$$g_N = g_{N0} - (u_1 - u_2) \cdot n \begin{cases} > 0(non-contact) \\ = 0(contact) \\ < 0(penetrate) \end{cases} \tag{3.38}$$

Eq. (3.38) is used to judge the state of contact/non-contact, in which n is the normal vector to the contact surface, g_{N0} is the original gap, expressed as Eq. (3.39):

$$g_{N0} = (x_2 - x_1) \cdot n \tag{3.39}$$

In Eq. (3.38), in the condition $g_N < 0$, the contacting bodies penetrate into each other and the penetration is defined as $g_N{}'$.

The tangential motions of contact state are associated with stick and slip. Stick refers to no relative motion between the two contact bodies while slip refers to existence of relative tangential motion. The motion can be defined using a function u_T in the tangential direction.

For stick condition:

$$u_T = [I - n \times n](u_1 - u_2) = 0 \tag{3.40}$$

while in slip conditions:

$$u_T = [I - n \times n](u_1 - u_2) \neq 0 \tag{3.41}$$

where I is the unit matrix. Through Eq. (3.38) to Eq. (3.41), the contact states are determined.

The compressive contact pressure p within the contact patch can be expressed as:

$$p = n \cdot \bar{\sigma} \cdot n \tag{3.42}$$

where $\bar{\sigma}$ is the boundary value of stress on the contact surface. For the slip zone, the frictional tangential traction employs Coulomb friction law and is defined as:

$$q = \mu p \tag{3.43}$$

For the stick zone, the frictional traction is expressed as:

$$q = \bar{\sigma} \cdot n - pn \tag{3.44}$$

The stress $\bar{\sigma}$ is converted to displacement based on the elastic or elasto-plastic material model. Thus, the relation between contact pressure/traction and displacement is developed.

(i.) Contact constraint enforcement

To solve the equilibrium equations, the contribution of total potential energy from the contact boundary is extracted and Eq. (3.29) is rewritten as:

$$\delta\Pi_p = \delta(\Pi_{ext,\mathrm{int}} + \Pi_c) = 0 \tag{3.45}$$

where $\Pi_{ext,\mathrm{int}}$ is the sum of internal and external energies except from the boundary of contact, and Π_c is the energy contribution from contact. The $\Pi_{ext,\mathrm{int}}$ term in Eq. (3.45) is further extended as:

$$\Pi_{ext,\mathrm{int}} = \int \{\varepsilon\}^T \{\sigma\} dV + \int \{\ddot{u}\}^T \{m\}\{u\} dV + \int \{f\}\{u\} dV + \int \{u\}^T \{f_b\} dS] \tag{3.46}$$

The term Π_c is expressed in different forms depending on the type of contact constraint method used. In this research, two common methods, the Lagrange multiplier method and the Penalty method are employed in the static and dynamic analysis respectively.

1) Lagrange Multiplier method

In this method, the contact potential energy Π_c is written as:

$$\Pi_c = \int (\lambda_N g_N + \lambda_T u_T) dS \tag{3.47}$$

To get the solution of the multipliers λ_N, λ_T, variation principle is employed as per Eq. (3.45). In that process, multipliers λ_N, λ_T are treated as the unknown variables. The variation of the total potential energy generates a set of equations from which multipliers is determined using Newton iteration algorithm. The overall process of solving the contact boundary problem with Lagrange Multiplier method is illustrated in Fig.3.5. The multipliers (λ_N and λ_T) correspond to the normal and tangential pressures (p and q) respectively.

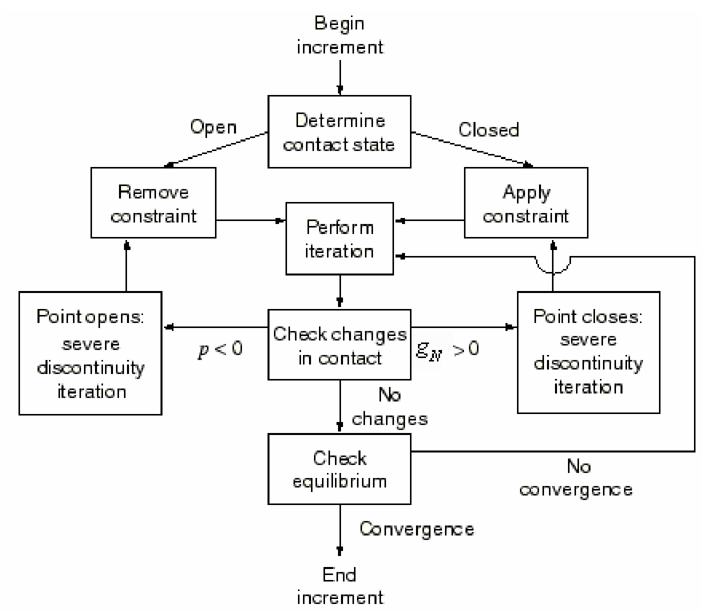

Figure 3.5 Process of solving the contact boundary problem using Lagrange Multiplier method (ABAQUS, 2003)

2) Penalty method

Relative to the Lagrange method, the Penalty method has the advantage that in the variational form the contact pressure and traction p and q are explicitly removed. Similar to Eq. (3.47), the contact potential energy can be expressed as:

$$\Pi_c = \frac{1}{2}\int (\chi_N (g_N^{'})^2 + \chi_T u_T \cdot u_T) dS \tag{3.48}$$

where χ_N, χ_T are penalty parameters, and $g_N^{'}$ is the penetration function. The values of penalty parameters χ_N, χ_T are properly set to avoid the ill-conditioned numerical problem.

For ABAQUS/Explicit, which is employed for dynamic analysis of wheel/rail contact, the process of solving the contact constraint using the Penalty method can be described as follows:

1) Surfaces of the two contacting bodies are firstly defined as a 'master-slave' pair.
2) The Penalty method searches for slave node penetration g_N in the current configuration.
3) Contact forces as a function of the penetration distance g_N are applied to the 'slave' nodes to oppose the penetrations, while equal and opposite pressures p are applied on the master nodes as equivalent forces. The penalty stiffness is used to calculate contact forces.
4) The equilibrium equations with the contact forces are then solved

Another constraint enforcement method named Kinematic method is also available in the ABAQUS/Explicit exclusively for the explicit time-integration method. The steps of this method are listed as follows:

1) The kinematic state of the model is advanced into a predicted configuration without considering the contact conditions.

2) The depth and the associated mass of the penetrated ‘slave’ nodes are then determined.

3) The resisting force required to oppose the penetration by using the penetration depth g_N, mass M and the time increment Δt is then calculated.

4) The resisting forces are then applied to the ‘master’ and the ‘slave’ surfaces to adjust the contact body from penetrating to contacting.

5) The equilibrium equations containing the contact forces are then solved.

(c) ALE Formulation

For contact problems, Lagrangian formulation employed in this thesis, is well understood and frequently used to solve the practical engineering problems. However, this formulation requires considerable computational cost especially when the contact model is large in size and the contact area requires refined mesh. For that reason, another efficient formulation namely, Arbitrary Lagrangian Eulerian (ALE), is recognized and developed in the recent years by many researchers such as Nackenhorst (2004),Ponthot and Belytschko (1997), Brinkmeier etc (2007). The major ALE advantages for rolling contact problems can be briefly concluded as:

1) A spatially fixed discretisation is introduced, which enables local refinement in the contact zone for more accurate analysis

2) Error control and adaptive mesh refinement can be performed with respect to

the spatial discretisation only

3) Superimposed transient dynamics is immediately described in space domain, which is required for example for rolling noise analysis

4) Within a purely Lagrangian description the whole circumference of the wheel has to be discretised as fine as needed for a detailed contact analysis. The number of unknows is drastically reduced when the rolling process is observed in a spatial observer framework

5) For the treatment of the explicit time dependency time discretisation schemes have to be involved. A stationary operating point has to be computed starting from the resting state

However, due to its rare application in the commercial code, which is important for practical modelling, in this research the Lagrangian formulation is employed. The basics of ALE formulation is briefly reviewed in this section for possible further model development in the future.

For rolling contact problems, the general idea of ALE formulation is the decomposition of motion into a pure rigid motion (φ) and the superimposed deformation (ϕ). The material deformation gradient is

$$O = \hat{O} \cdot Q \tag{3.49}$$

Where the Q is the pure rigid body motion and the $\hat{O}$ is a measure for the deformation of rolling body.

The elementary balance laws of solid mechanics in the ALE formulation contain two section: balance of mass and balance of momentum. The balance of mass is represented as Eq. (3.50)

$$M = \int_{\hat{\phi}} \rho dV = \int_{\varphi} \hat{\rho} d\hat{V} = \int \rho_0 dV = const. \tag{3.50}$$

Where the M is the mass, ρ is the mass density and the V is the mass volumn. On the other hand the balance of momentum is written as following with respect to the reference configuration,

$$Div\hat{P} + \hat{\rho} f = \hat{\rho} \frac{dv}{dt} \tag{3.51}$$

The $\hat{P}$ denotes the First Piola-Kirchhoff stress tensor, f is the body force density and the v the velocity of the material particals. The boundary condition can be described as:

$$\begin{aligned} \phi &= \overline{\phi} \\ \hat{P} \cdot \hat{N} &= \overline{T} \end{aligned} \tag{3.52}$$

In addition the contact conditions should be satisfied.

For approximate solutions using the finite element method the balance law is re-written in a weak form as Eq. (3.53)

$$\int (Div\hat{P} + \hat{\rho} f - \rho \frac{dv}{dt}) \cdot \eta d\hat{V} \tag{3.53}$$

This equation can be further developed to the incremental finite element representation of the equations of motion,

$$M\ddot{d} + G\dot{d} + [K - W]\Delta d = \mathrm{f}_{\mathrm{ext}} + \mathrm{f}_{\mathrm{inertia}} - \mathrm{f}_{\mathrm{int}} \tag{3.54}$$

To be solved for the evolution of the displacement field

$$d^{t+\Delta t} = d^t + \Delta d \tag{3.55}$$

The K is the tangential stiffness matrix, M is the standard mass matrix

$$G = \int \hat{\rho}(N^T A - A^T N) d\hat{V} \tag{3.56}$$

is the gyroscopic matrix and

$$W = \int \hat{\rho} A^T A d\hat{V} \tag{3.57}$$

is the ALE inertia matrix obtained from the linearization of the centrifugal forces.

For the contact boundary condition, the normal and tangential contact can be treated locally decoupled. For the normal contact, the enforcement of the Signorini condition is written as

$$g_N \leq 0,\ p \geq 0,\ pg_N = 0 \tag{3.58}$$

Well established algorithm for contact computation can be applied directly to enforce the normal contact constraints. The penalty method for example leads to the contact force contribution

$$f_{contact} = -\int \bar{N}^T \chi_n^t g_N da \tag{3.59}$$

Contribution to the tangent matrix:

$$K_{contact} = \int \chi_n \bar{N}^T \alpha_n \alpha_n{}^T \bar{N} da \tag{3.60}$$

However, the well established techniques developed within a pure Lagrangian framework can not be applied directly to enforce the tangential contact constraints within the ALE picture. This leads to the additional treatment from the Lagrangian to ALE formulation and can refer to Ziefle's (2007) work.

3.3. Review of Solution Methods for Finite Element Method

The solution methods for non linear problems can be classified into two types:

- Time independent
- Time dependent

The time independent algorithm is explored for static problems without considering the inertial effect, while the time dependent algorithm is suitable for the dynamic problems in which the inertial effect is not negligible. Both of the two methods are employed in the finite element model used in this research.

3.3.1 Algorithm for time-independent problems

For static non-linear problems, iteration methods such as the Newton's method are widely used in the finite element analysis to solve the system of equilibrium equations. The entire procedure of solving the non-linear equations is divided into several increments and each increment is subdivided into iterations.

Eq.(3.30) can be written as follows with the superscript n representing the increment n:

$$F^{n}(u) = 0 \tag{3.61}$$

The u is the exact solution of displacement. To obtain that solution, assume that an approximation u_i is obtained after the iteration i. The Δu_i is the difference between u and u_i, so:

$$F^n(u_i + \Delta u_i) = 0 \qquad (3.62)$$

Expanding the left-side of this equation in a Taylor series gives:

$$F^n(u_i) + \frac{\partial F^n}{\partial u_i}(u_i)\Delta u_i + \frac{\partial^2 F^n}{\partial {u_i}^2}(u_i)\Delta {u_i}^2 + \ldots = 0 \qquad (3.63)$$

Since u_i is a close approximation to the solution, Δu_i should be small. As a result, the second and higher order terms of Δu_i can be neglected. Eq. (3.63) is simplified as:

$$K_i^n \Delta u_i = -F_i^n \qquad (3.64)$$

Where $F_i^n = F^n(u_i)$ and K_i^n is the Jacobian matrix which is solved as:

$$K_i^n = \frac{\partial F^n}{\partial u_i}(u_i) \qquad (3.65)$$

Δu_i can then be obtained from Eq. (3.64) and the next approximation is expressed as:

$$u_{i+1} = u_i + \Delta u_i \qquad (3.66)$$

The iteration continues until the Δu_i is small enough that the solution is considered convergent.

3.3.2 Algorithm for time-dependent problems

For dynamic problems, two algorithms have been widely used in the finite element method: explicit time integration method and implicit time integration method. Wriggers (2002) gives basic instructions about these two methods:

- *Explicit time integration methods are easy to implement, since the solution at time t_{n+1} depends only upon known variables at t_n. These methods are* *extremely efficient when the mass matrix is approximated by a lumped mass matrix which is diagonal. Explicit methods are conditionally stable, which means that the time step size is governed by the Courant criterion (a condition on numerical method calculations requiring that the time interval employed be no greater than that required for a stress wave to cross the characteristic length of elements).*

- *Implicit time integration method schemes approximate time derivatives by quantities which also depend upon the last time step* t_n *and upon the still unknown values at time* $t_{n+\alpha}$. *These methods require a solution of a nonlinear equation at each time step. They are much more expensive, since they have to be combined with, for example, the Newton procedure. However, implicit schemes can be constructed so that they are unconditionally stable, and hence can be applied with a far bigger time step than the explicit schemes.*

The time step size for both these two methods depends on the nature of the problem. For high frequency response problems, such as impact, a small step size is necessary which should be lower than the time period of the sound wave travelling through the characteristic length of element.

For dynamic problems, the inertial force is not negligible and the system is in dynamic equilibrium which is expressed as:

$$M\ddot{u} + C_d\dot{u} + Ku = F \tag{3.67}$$

(a.) Explicit time integration

In the finite element method, a central difference scheme is widely applied where velocities and accelerations at time t_n are approximated by:

$$\dot{u}_n = \frac{u_{n+1} - u_{n-1}}{2\Delta t}, \qquad \ddot{u}_n = \frac{u_{n+1} - 2u_n + u_{n-1}}{(\Delta t)^2}. \tag{3.68}$$

Inserting the above functions into Eq. (3.63), Eq. (3.69) can be obtained:

$$(M + \frac{\Delta t}{2} C_d) u_{n+1} = (\Delta t)^2 [F_n - K u_n] + \frac{\Delta t}{2} C_d u_{n-1} + M(2u_n - u_{n-1})\mathbb{F} \tag{3.69}$$

To solve, initial conditions u_0 and $\dot{u}_0$ are required. Note the term u_{n-1} exists, which means at the first step u_{-1} needs to be determined first. By using a Taylor series expansion at time t_{-1}, we obtain:

$$u_{-1} = u_0 - \Delta t \dot{u}_0 + \frac{(\Delta t)^2}{2} \ddot{u}_0 \tag{3.70}$$

where $\ddot{u}_0$ is obtained from Eq. (3.67) as follows:

$$\ddot{u}_0 = M^{-1}[-C_d \dot{u}_0 - K u_0 + F_0] \tag{3.71}$$

The process introduced above is the concept of a classical approach of solving the equations explicitly. Different finite element codes adopt different algorithms. In ABAQUS/Explicit, the equations of motion for the body are integrated using the explicit central difference integration rule:

$$\dot{u}_{i+\frac{1}{2}} = \dot{u}_{i-\frac{1}{2}} + \frac{\Delta t_{i+1} + \Delta t_i}{2} \ddot{u} \tag{3.72}$$

$$u_{i+1} = u_i + \Delta t_{i+1} \dot{u}_{i+\frac{1}{2}} \tag{3.73}$$

where $\dot{u}$ is velocity and $\ddot{u}$ is acceleration. The subscript i refers to the increment number and $i-\frac{1}{2}$ and $i+\frac{1}{2}$ refer to mid-increment values. The central difference integration operator is explicit in that the kinematic state can be advanced using known values of $\dot{u}_{i-\frac{1}{2}}$ and $\ddot{u}_i$ from the previous increment:

$$\ddot{u}_i = M^{-1} \cdot (F_{ext\,i} - F_{\text{int}\,i}) \tag{3.74}$$

where M is the nodal mass matrix, F_{ext} is the applied external load, and F_{int} is the internal force.

Special treatment of the mean velocities $\dot{u}_{i+\frac{1}{2}}$, $\dot{u}_{i-\frac{1}{2}}$ etc. is required for initial conditions, certain constraints, and presentation of results. For presentation of results, the state velocities are stored as a linear interpolation of the mean velocities:

$$\dot{u}_{i+1} = \dot{u}_{i+\frac{1}{2}} + \frac{1}{2} \Delta t_{i+1} \ddot{u}_{i+1} \tag{3.75}$$

The central difference operator is not self-starting because the value of the mean velocity $\dot{u}_{-\frac{1}{2}}$ needs to be defined:

$$\dot{u}_{\frac{1}{2}} = \dot{u}_0 + \frac{\Delta t_1}{2} \ddot{u}_0 \tag{3.76}$$

Substituting this expression into the updated expression for $\dot{u}_{i+\frac{1}{2}}$ yields the following definition of $\dot{u}_{-\frac{1}{2}}$:

$$\dot{u}_{-\frac{1}{2}} = \dot{u}_0 - \frac{\Delta t_0}{2}\ddot{u}_0 \tag{3.77}$$

The explicit procedure requires no iterations and no tangent stiffness matrix (See Eq. (3.74)), thus explicit integration dynamic analysis requires less computation cost for each time increment. However, as the central difference operator is conditionally stable, the increment should be significantly small. The stability limit for the operator is given in terms of the highest Eigenvalue in the system as:

$$\Delta t \le \frac{2}{\varpi_{\max}}(\sqrt{1+\xi^2}) - \xi) \tag{3.78}$$

where ξ is the fraction of critical damping associated with the highest mode. Another conservative estimate of the stable time increment can be given by the minimum taken over all the elements:

$$\Delta t = \min(L_e / C_d) \tag{3.79}$$

where L_e is the characteristic element dimension and C_d is the current effective dilational wave speed of the material which is related with density, elastic modulus, and Poison ratio of the material:

$$C_d = \sqrt{\frac{E(1-\nu)}{\rho(1+\upsilon)(1-2\upsilon)}} \tag{3.80}$$

ABAQUS/EXPLICIT uses the explicit integration algorithm for solving equilibrium equations. Simulations using this method generally take of the order of 10,000 to 1,000,000 increments, but the computational cost per increment is relatively cheap.

(b.) Implicit time integration

One of the most widely applied implicit methods is the Newmark (1959) method. The approximations of displacement and velocity at time t_{n+1} are based on the following two functions:

$$
\begin{aligned}
u_{n+1} &= u_n + \Delta t \dot{u}_n + \frac{(\Delta t)^2}{2}[(1-2\vartheta)\ddot{u}_n + 2\vartheta \ddot{u}_{n+1}], \\
\dot{u}_{n+1} &= \dot{u}_n + \Delta t[(1-\upsilon)\ddot{u}_n + \upsilon \ddot{u}_{n+1}].
\end{aligned} \tag{3.81}
$$

where the constant parameters ϑ and υ can be chosen freely and the order and accuracy of the method is determined. By inserting Eq. (3.81) into Eq. (3.67), we can get the equilibrium equation which can now be solved by using some iteration method such as the previously introduced Newton method. By obtaining the solution of acceleration $\ddot{u}_{n+1}$, other variables like displacement and velocity can be worked out using Eq. (3.81).

In summary, for the solution of wheel/rail dynamic contact at IRJs, both implicit and explicit methods may be used. However, there are some significant differences between them. The implicit method calculates the overall dynamic response of the structure in each iteration while the explicit method employs the wave propagation solutions associated with relatively local response in continua. The implicit method is unconditionally stable because of the iteration process. In contrast, the conditionally stable explicit method is only stable when the increment is small enough relative to the stress wave propagation.

The nature of impact problems determines that the time increment should be small and hence the number of increments would be numerous. By using the implicit method, the computational cost would be unacceptablely expensive as every increment would involve a number of iterations. By contrast, the explicit method would provide a much cheaper solution by computing local response in each increment; a reasonably accurate result can be guaranteed if the increment step is kept small.

3.4. Discussion of Contact Impact

The impact condition emerges as the rate of loading is high and the dynamic effects are important. In other words, in wheel/rail rolling or sliding contact, the material inertia flows through the deforming region and influences the stress field. This leads to the stress propagation wave in the contact bodies and material plasticity may be caused under the high rate of loading. Referring to Johnson (1985), the stress wave amplitude is expressed as:

$$\sigma = \rho c_0 v \tag{3.82}$$

where σ is the stress, ρ is the contact body density, c_0 is the stress wave propagation velocity and v is the deformation velocity of the contact body. If the stress value exceeds the yield stress Y, the material yields. To keep the material in elastic condition, the deformation velocity must be less than the certain value:

$$v < Y / \rho c_0 \tag{3.83}$$

For steel material employed in this research, the yield stress is 780MPa, the density is 7800Kg/m^3 and therefore the stress propagation speed is 5900m/s. As a result, the maximum impact velocity in the deformation direction for elastic deformation is 16.95m/s. Deformation rates above this magnitude causes material yield.

3.5. Summary

In this chapter contact mechanics was first briefly reviewed. For classical theory, the Hertz contact theory has provided the analytical contact solution with the elastic half space assumption. Non-Hertz theory has also been discussed and it was shown that it better represents some special contact situations. However, it has also been shown that both Hertz and non-Hertz theory did not provide a practical solution for wheel/rail contact at IRJs. For computational contact mechanics, the contact boundary conditions have been introduced through constraint enforcement. The Lagrange Multiplier method and the Penalty method appear advantageous for the contact solutions.

4. Finite Element Modelling Strategies

4.1. Introduction

In this chapter, a 3D wheel/IRJ FE contact-impact model is reported. Some simplification strategies are employed to reduce the model size. The exact geometry, material zones, boundary conditions and loading are simplified in the idealised model presented. The wheel-IRJ railhead contact is first established in the static analysis and the results transferred to dynamic analysis for impact simulations. Details of contact modelling in both the static and the dynamic procedures are also presented. Numerical examples of the static/dynamic FE model is reported in Chapter 5.

4.2. Complexities of Modelling IRJ

It is fairly complex to simulate the behaviour of an IRJ that works under the dynamic environment of wheel passages. The dynamics of the IRJ are affected by the characteristics of the rolling stock and that of the IRJ itself. The dynamics of the rolling stock is idealised as pure rolling/sliding of the wheel; only a single wheel with a proportional wagon mass is modelled. The complexities of modelling the IRJ can be illustrated through the discussion of geometry, material and boundary condition.

4.2.1. Geometry

The conventional IRJ used in Australia consists of rails, joint bars, bolts, washers and nuts and insulation materials for joint bars and end post (Fig. 4.1).

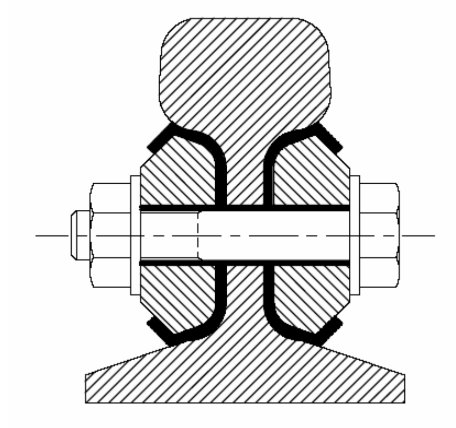

(a) Cross section of IRJ

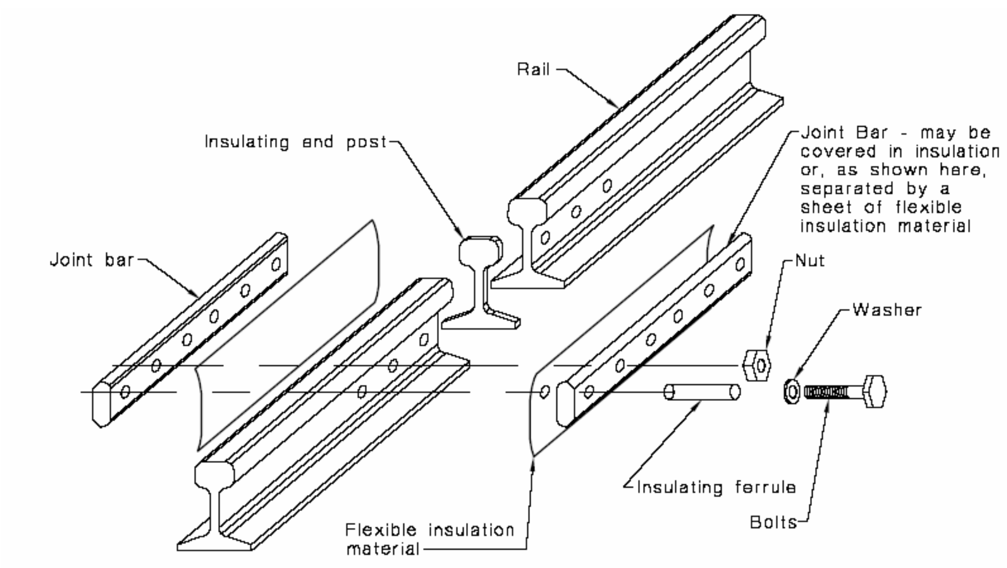

(b) Exploded view

Figure 4.1 Typical insulated rail joint assembly (AS1085.12, 2002)

This thesis considers the IRJ that consists of AS 60kg rail (Fig. 4.2) and joint bar (Fig 4.3) connected by M24 bolt (Fig. 4.4).

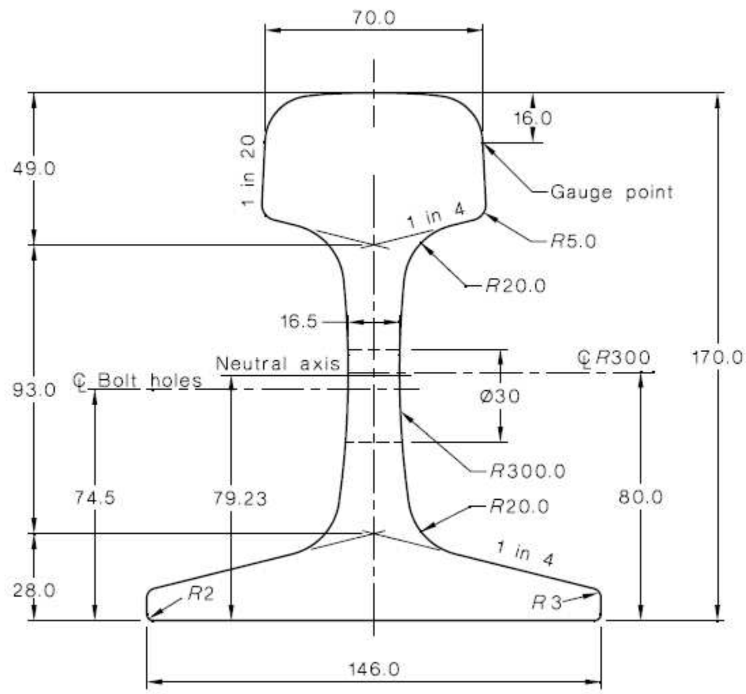

Figure 4.2 60kg Rail dimension (Standards Australia, 2002)

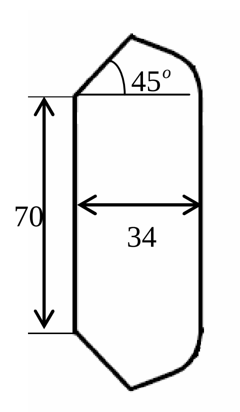

Figure 4.3 Joint bar dimensions

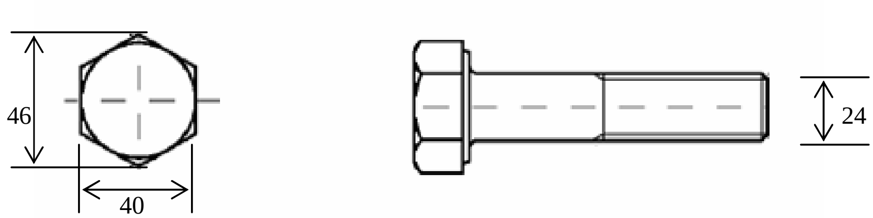

Figure 4.4 M24 Bolt dimensions (Standard Australia & Standard New Zealand, 1996)

As illustrated in Fig. 4.5, the wheel tread and hub is designed to withstand heavy loading due to contact forces and axle loading. The thin wheel web reduces the wheel mass and the wheel flange is necessary to provide guidance along curved track.

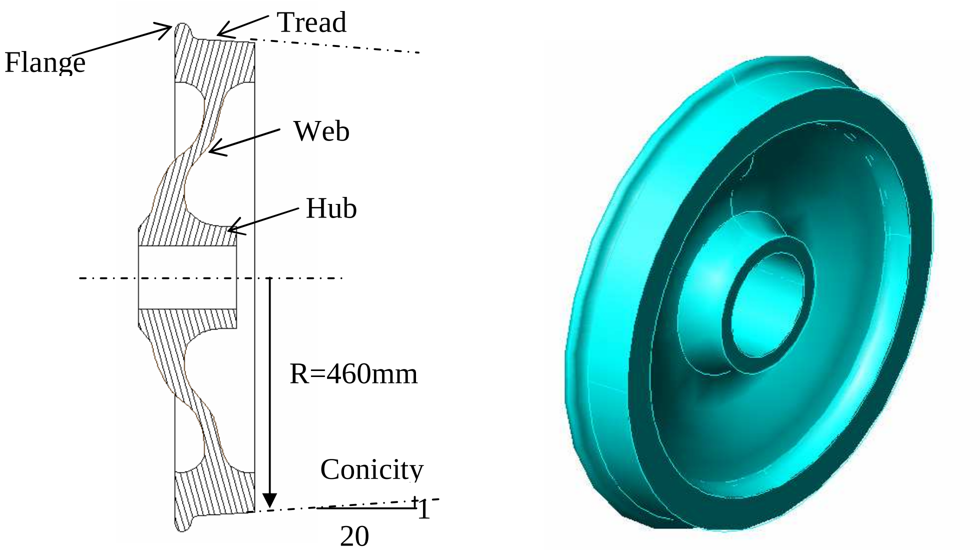

Figure 4.5 Geometry of wheel

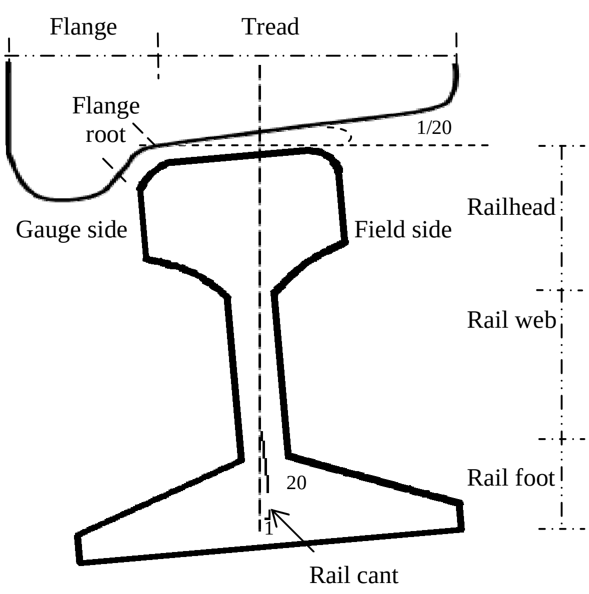

Figure 4.6 Rail/wheel vertical section alignment

The wheel profile without any wear or flat is perfectly conical with the conicity of 1/20. The vertical axis of IRJs also has an inclination of 1/20. Fig. 4.6 illustrates the alignment of the rail to maintain its contact to the wheel.

4.2.2. Material

The wheel and the rail material (steel) is assigned elasto-plastic properties. Table 4.1 lists the mechanical properties of steel and insulation material Nylon66:

Table 4.1 Mechanical property of steel and insulation material (Chen, 2002)

Property	*Steel*	*Nylon66*
Young's modulus	210GPa	1.59GPa
Poisson's ratio	0.3	0.39
Density	7800kg/m^3	1140kg/m^3
Yield Stress	780MPa	(elastic only)

4.2.3. Boundary Conditions

Under pure rolling, the wheel rotates at an angular velocity ω that corresponds to the linear velocity v. The wheel motion is restrained in the lateral direction; in other words, DOFs 5 and 6 (Fig. 4.7) are arrested.

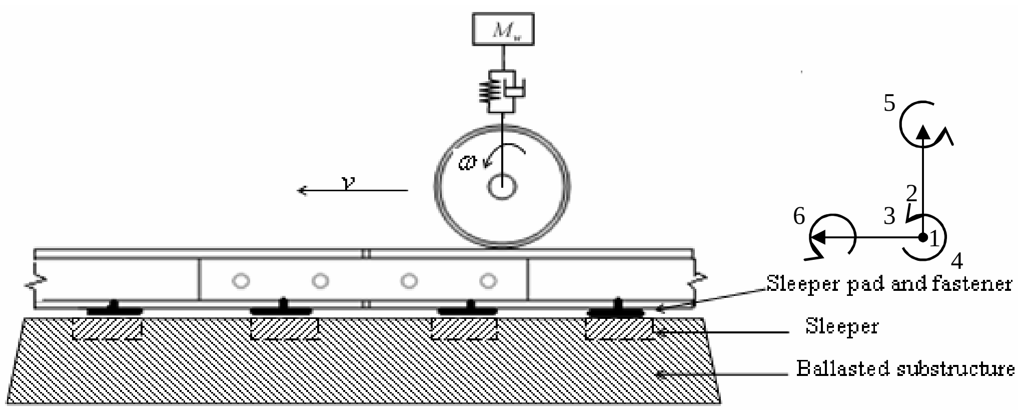

Figure 4.7 Boundary conditions of wheel and IRJ

The rail is positioned on the ballast bed using sleepers (prestressed concrete sleepers in this case) which are embedded into the ballast layer. Sleeper pads are inserted between the sleepers and the rail bottom and are fixed by the fastening system (see Fig. 4.8).

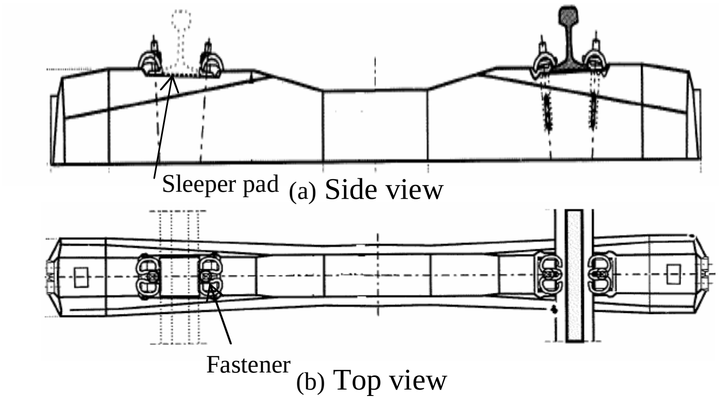

Figure 4.8 Typical prestressed concrete sleeper arrangement (Esveld, 2001)

In the longitudinal direction, the wheel load influences the rail deflection for a certain length. According to Sun (2003), referring to Fig. 4.9, the length is approximately 10m for AS 60kg rail subjected to a concentrated wheel load of 100KN. In this thesis, the length of rail being modelled is 12m which is sufficient for the load influence.

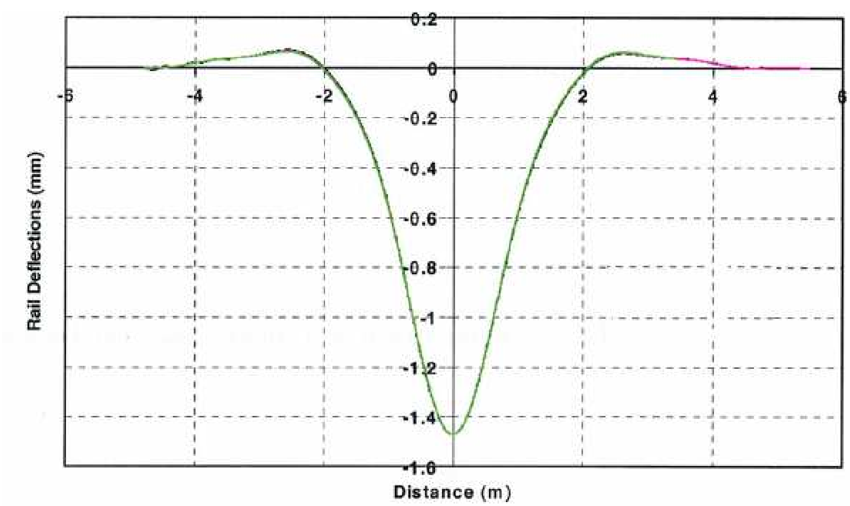

Figure 4.9 Rail effect length with deflection (Sun, 2003)

The wheel/rail contact is another boundary condition that provides restraint in both the vertical and horizontal directions.

4.3. Strategy-1: Simplifications of Geometry Modelling

The complexity of the IRJ and the wheel geometry demands simplifications to reduce the computational cost. For the IRJ, as attention is focused on the dynamics and failure of the railhead wheel contact impact area in the vicinity of the end post, the finite element model was simplified to just one part model by ignoring the interaction between the contact surfaces of the rail, the joint bars, the bolts, and the nuts. Furthermore, the bolt-heads and nuts are not essential and hence they are ignored. However, the bolt shank is retained to apply the pre-tension load. In other words, as shown in Fig.4.10, the fully assembled IRJ was assumed as one instance partitioned with varying material regions (insulation & rail steel materials). Although the simplified model can not predict failure modes such as bolt looseness and delamination, it has been found quite sufficient for the determination of contact impact forces of the railhead in the vicinity of the end post.

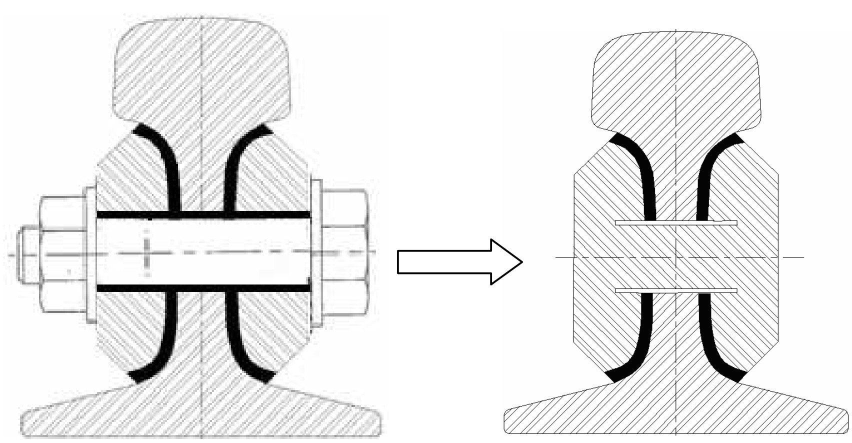

Figure 4.10 Idealisation of the IRJ geometry

Since this research focus is on the impact at IRJs and the function of the wheel is to provide a contact patch across the IRJ, the geometry of wheel cross-section is also simplified. Since the flange contact is out of our scope, the wheel flange is firstly removed and the wheel cross-section is also simplified as shown in Fig. 4.11. The wheel radius and tread conicity are kept the same as the design of 460mm and 1/20 respectively.

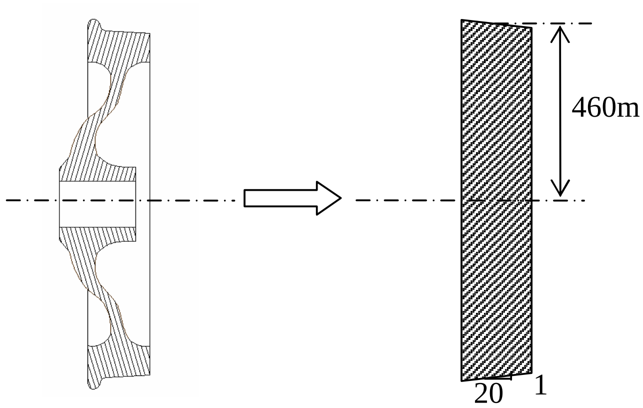

Figure 4.11 Wheel geometry simplification

As a result, the 3D full-scale FE model is generated as shown in Fig. 4.12based on the above idealised geometries of the IRJ and wheel.

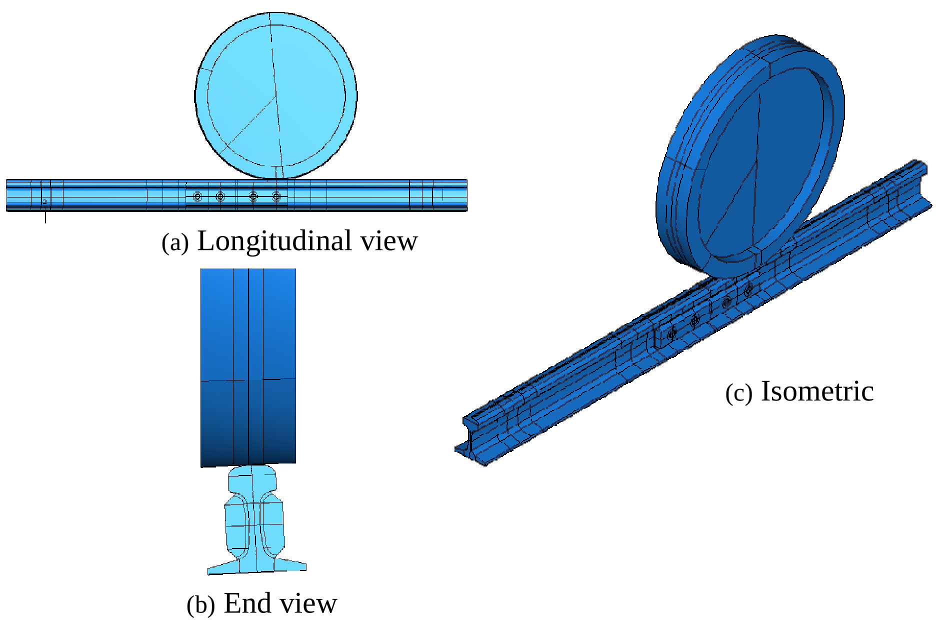

Figure 4.12 Geometry of FE model

4.4. Strategy-2: Simplifications of Material Modelling

Although steel is elasto-plastic, as the bulk of the rail section is subjected to very low levels of stresses under wheel passage, for all those regions steel is considered elastic. The zone close to the wheel contact patch is partitioned to assign elasto-plastic properties. The joint bar, bolt shank and bulk of the wheel steel are simply considered as elastic. A narrow strip of the wheel tread is assigned with elasto-plastic steel property. The end post and thin partition between the rail web and the joint bar are assigned Nylon66 properties that remained elastic.

4.4.1. Elasto-plastic steel zones

The elasto-plastic steel zone is limited to the vicinity of the end post close to the wheel/rail contact patch. The length of this zone is defined as the product of the longitudinal velocity of the wheel and the duration of the simulation. Correspondingly, the elasto-plastic zone of the wheel is a strip across the wheel tread as shown in Fig. 4.13.

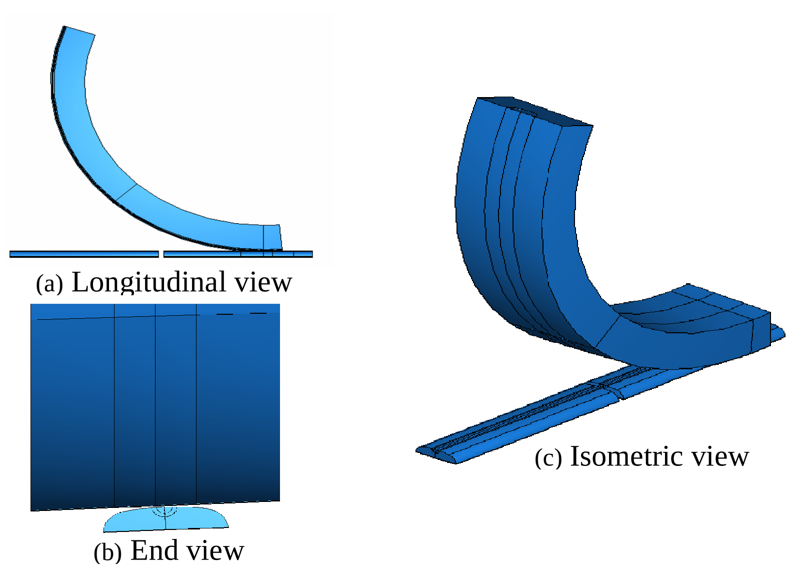

Figure 4.13 Elasto-plastic steel zone for wheel and IRJ

4.4.2. Insulating material zones

The insulating material zones are modelled for the rail end post insulation and joint bar/rail insulations. As the geometry has been simplified, the insulation between the bolt shank and rail web hole is ignored (rather a gap is provided between the surfaces of these two parts). Fig. 4.14 shows the insulating material zones of the IRJ.

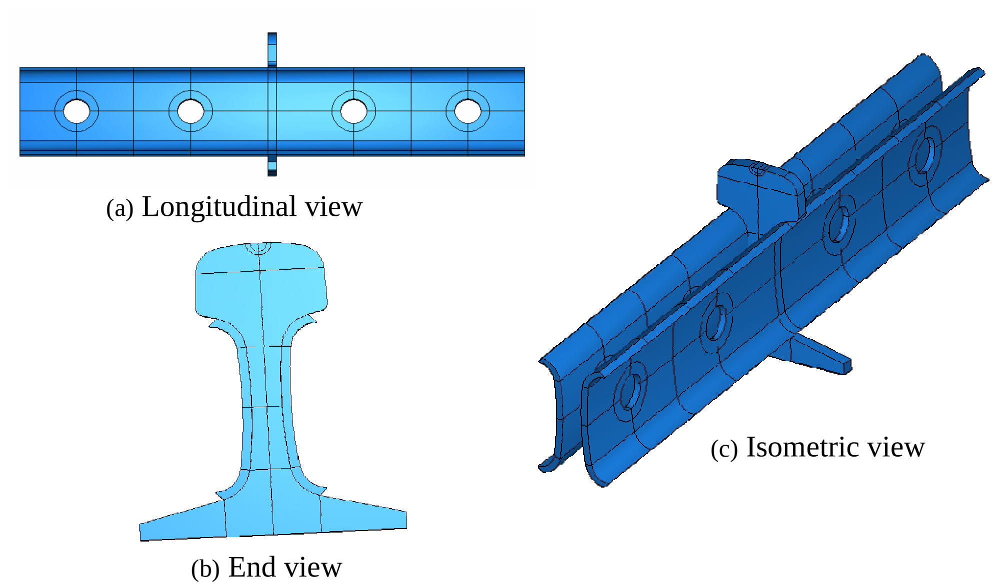

Figure 4.14 Insulation zone of IRJ

4.5. Strategy-3: Simplifications of Boundary Conditions

The IRJ is supported on the ballasted substructure through sleepers and sleeper pads at the rail bottom. Modelling such a mechanical system is very expensive and unnecessary, particularly for this research that is focused on the impact at the railhead. To reduce the computational cost, some simplifications are made for modelling the sleepers, the sleeper pads, the fasteners and the ballasted substructure. In the longitudinal direction, the rail end boundary condition is also simplified.

4.5.1. Idealisation of support system

The function of sleepers is to support the rail and transfer the loading to the substructure. The rail bottom is fixed to the sleeper by the fastener and the sleeper pad is used to minimise the damage to the sleeper top surface. For the IRJ, the interactive surfaces with the sleepers are restrained in all directions. Sleeper itself was simplified as a spring and dashpot.

The rail support system is modelled as shown in Fig. 4.15. The interaction of the rail bottom surface and the sleeper top surface is modelled through coupling at a single reference point that has six DOFs of which five DOFs except the vertical displacement DOF are arrested. The effective area that represents the coupling zone is determined as the product of the top width (136mm) of the prestressed concrete sleeper and the width of the rail base (146mm). The sleepers are spaced at 700mm. The stiffness and damping of the support system are combined with that of the substructure.

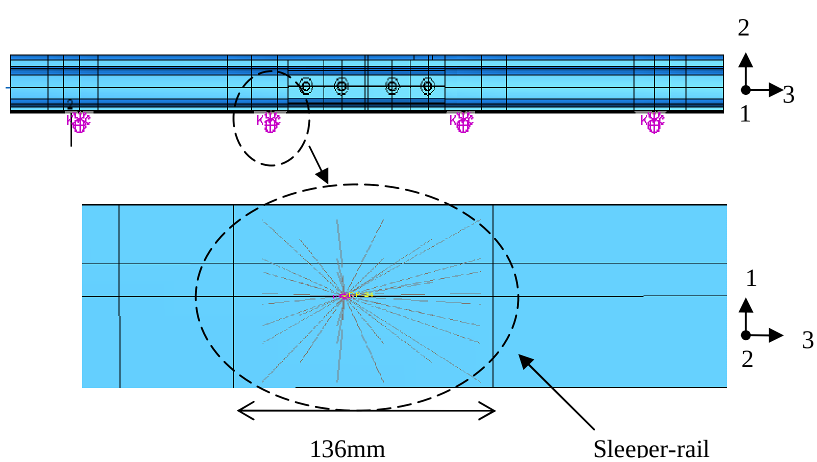

Figure 4.15 Sleeper support idealisation

4.5.2. Elastic support

The property of ballast substructure is non-linear and complicated. To set up a model of reasonable size, the ballast substructure is usually simplified as an elastic layer. There are several models reported in the literature that treat ballast as an elastic support (Zhai (1996), Newton and Clark (1979), Fermer and Nielsen(1995)). In this research, a linear single layer model is employed as shown in Fig. 4.16. One end of each spring/dashpot element is connected to the reference node (Fig. 4.16) and the other end is fixed to the ground.

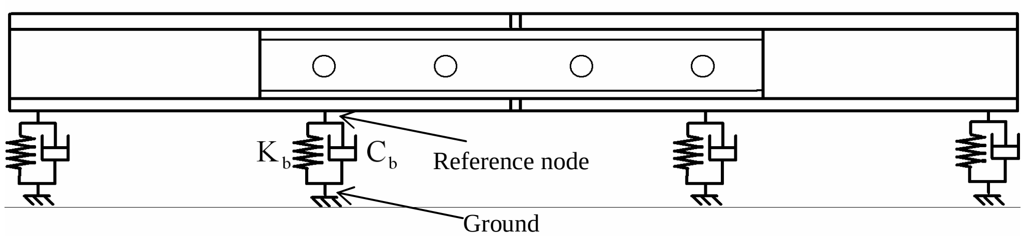

Figure 4.16 One-layer rail elastic support model

4.5.3. Beam element to solid element connections

As described in section 4.2, to truly account for the effect of wheel loading, a 12m long rail is necessary for the system considered. It is very expensive to model the 12m long rail using 3D solid elements. Hence, a beam element is employed to model a segment of 9.6m long rail and the remaining 2.4m rail in the vicinity of the end post is modelled using solid elements. Therefore, it becomes essential to ensure proper connection between the beam elements and the solid elements.

Each end of the rail section of solid element, is assumed to be a rigid surface disregarding shear deformation. The beam element is positioned in such a way that its geometric centre coincides with the geometric centre of the rail section modelled with solid elements.

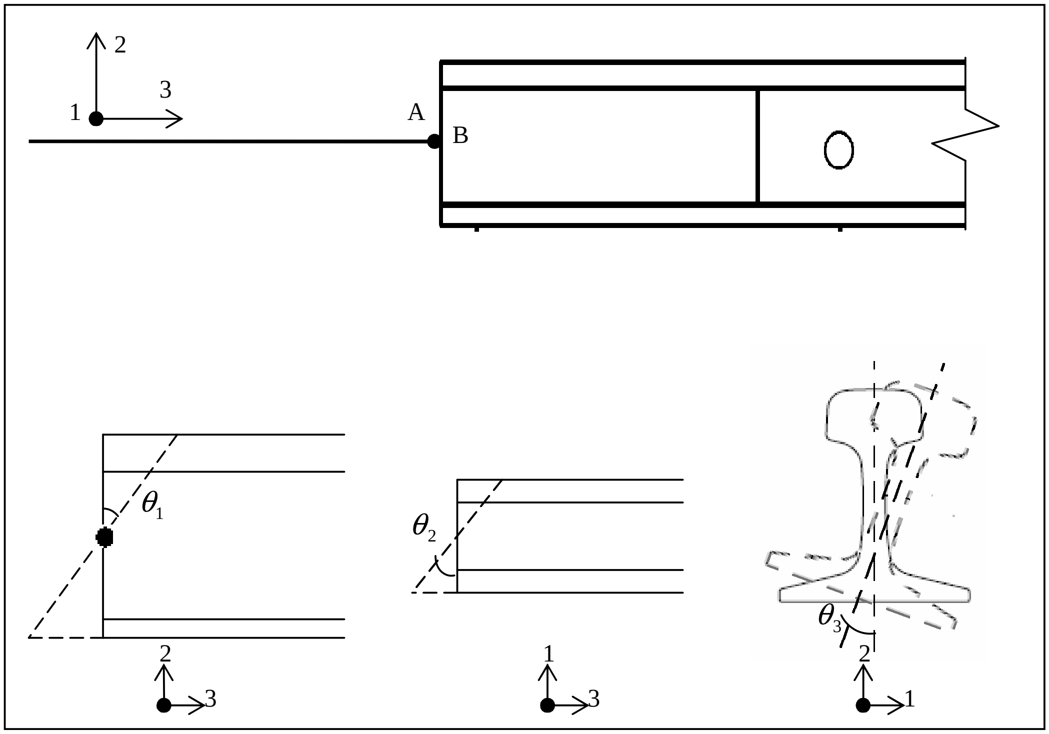

Figure 4.17. Beam-solid element connection

Referring to Fig. 4.17, the nodes A and B belong to the beam element and the solid element respectively. The six DOFs of the beam element node A $u_{1A}, u_{2A}, u_{3A}, u_{4A}, u_{5A}, u_{6A}$ are related to the three DOFs of the solid element nodes u_{1B}, u_{2B}, u_{3B} as shown in Eq. (4.1).

$$\begin{cases} u_{1A} = u_{1B} \\ u_{2A} = u_{2B} \\ u_{3A} = u_{3B} \\ u_{4A} = \theta_1 \\ u_{5A} = \theta_2 \\ u_{6A} = \theta_3 \end{cases} \tag{4.1}$$

where $\theta_1, \theta_2, \theta_3$ are rail section rotation about the geometric centre and defined by Eq.(4.2) as the quotient of several controlling node displacements and their distance to the geometric centre as shown in Fig. 4.18. Nodes B, C, D are all in the rail section plane. Node B is the geometric centre of the rail section and Node C is located at the railhead surface centre and Node D is located at the rail web surface with the same vertical distance to the bottom as Node B.

$$\begin{cases} \theta_1 = (u_{3C} - u_{3B}) / d_{BC} \\ \theta_2 = (u_{3D} - u_{3B}) / d_{BD} \\ \theta_3 = (u_{1C} - u_{1B}) / d_{BC} \end{cases} \tag{4.2}$$

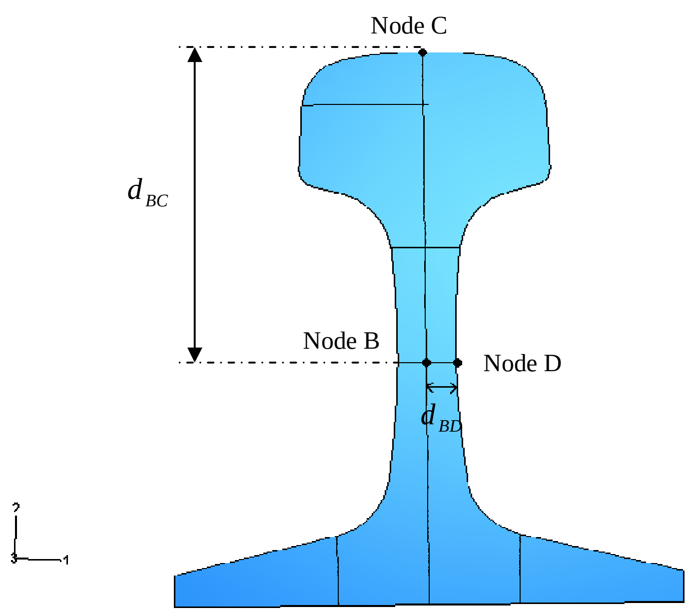

Figure 4.18 Controlling nodes for rail section rotational DOFs

Fig. 4.19 presents the beam-solid connection in the 3D model.

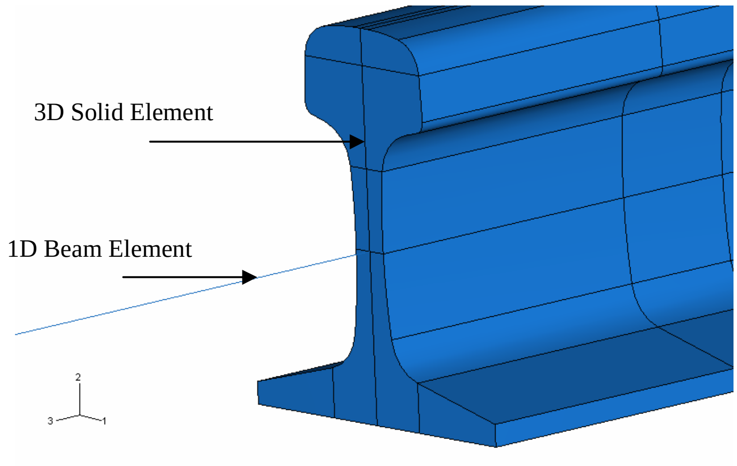

Figure 4.19 Beam-solid connection of 3D model

A schematic diagram of the full model of the IRJ is shown in Fig. 4.20.

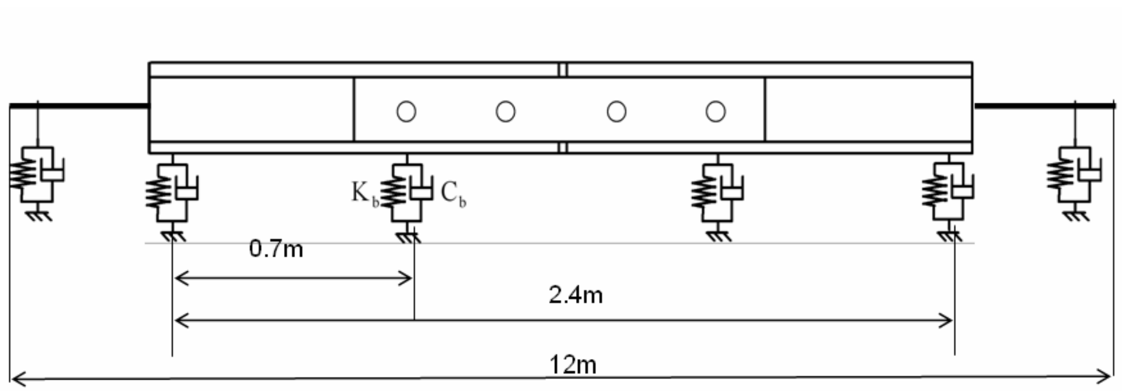

Figure 4.20 Schematic diagram of the full IRJ model

4.5.4. Boundary conditions of the wheel

Proportion of wagon mass is transferred to the wheel through the suspension system as shown in Fig. 4.21. The proportional mass is obtained by dividing the gross wagon mass by the number of wheels. Similar to the elastic support system, the suspension system is simplified into a single layer spring/damping model.

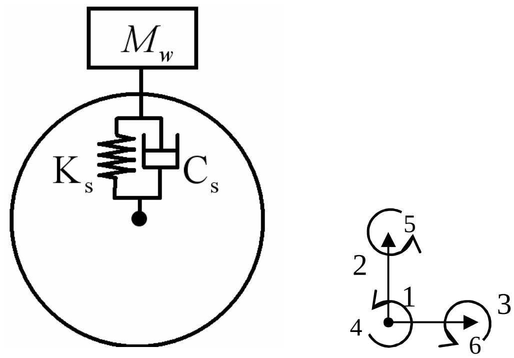

Figure 4.21 The wheel loading system

In the static wheel/rail contact model, the wheel DOF 2 is free and DOFs 1 and 3 are arrested. In the dynamic analysis, the lateral motion of the wheel is restrained to ensure the contact stability before impact. The wheel DOFs 2 and 3 are set free. For the pure rolling condition, the wheel body is assigned an initial condition of rotating speed ω around its centre axis and a longitudinal velocity v which is defined as the product of rotating speed and the radius.

For the pure sliding case (that models the brake force applied to the wheel causing wheel locking) the wheel is assigned with the longitudinal velocity v without the rotating speed ω. In other words, the wheel DOF 3 is set to the velocity of v, DOF 2 is free and DOFs 1, 4, 5, 6 are arrested.

4.6. Strategy-4: Loading Strategy

Prior to impact, the railhead and the wheel must attain a steady state of contact in order to ensure confidence in the solutions of the impact at the IRJ. Compared with the dynamic analysis using ABAQUS/Explicit, the static analysis employing ABAQUS/Standard has the advantage of attaining the steady state of contact with much cheaper computational cost. This strategy leads to a two-stage analysis for whee/rail contact impact at the IRJ.

In the static model, bolt pretension load, wheel axle load and the wheel centrifugal force are applied to the FE model. Bolt pretension load is applied through the internal cross section of the bolt shank, as shown in Fig. 4.22. Bolt pretension P_b is calculated from the bolt torque moment *T*, the bolt diameter *D* and the coefficient of the bolt torque moment K_b (K_b=0.19-0.25) as shown in Eq. (4.3).

$$P_b = \frac{T}{K_b D} \tag{4.3}$$

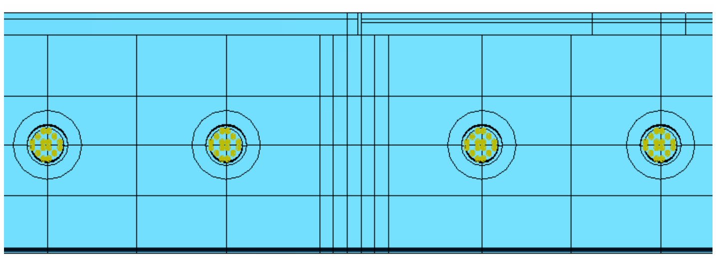

(a) Longitudinal view

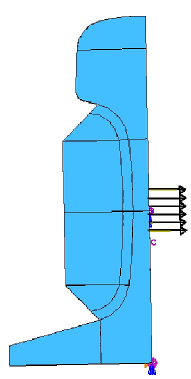

(b) End view

Figure 4.22 Bolt pretension load application

The wheel axle load is the weight of proportional wagon mass and applied to wheel centre, shown as Fig. 4.23. The wheel centrifugal force is employed to the static model as the preload of rotation. This was necessary as steady state rolling/sliding was desired in the dynamic analysis.

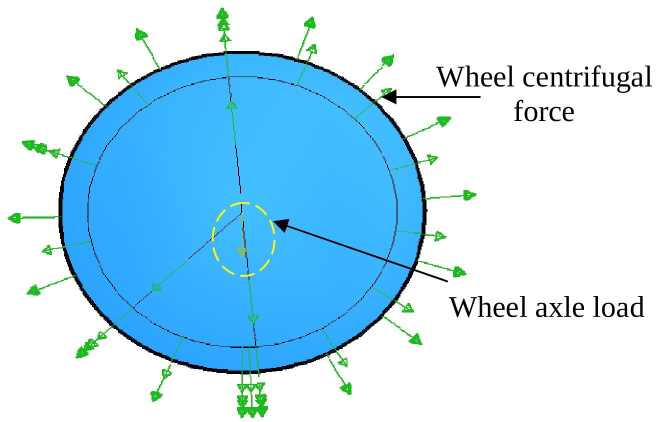

Figure 4.23 Wheel axle load and centrifugal force

4.7. Strategy-5: Wheel/Rail Contact Modelling

Definition of rail/wheel contact interaction in ABAQUS is very sensitive to convergence, accuracy of result, and computational time. Thus careful definition of the rail/wheel contact is the key to the impact dynamic analysis.

In the modelling, the master/slave contact surface method is employed for both the static and the dynamic analyses. The surfaces of the wheel are defined as the master, and the railhead is defined as the slave. The contact surface pair is allowed to undergo finite sliding. The interface friction is described with the Coulomb friction law by defining a friction coefficient μ . In the normal direction, the pressure-overclosure relationship is set to HARD meaning that surfaces transmit no contact pressure unless the nodes of the slave surface contact the master surface. Fig. 4.24 shows the contact surfaces of the wheel and the railhead.

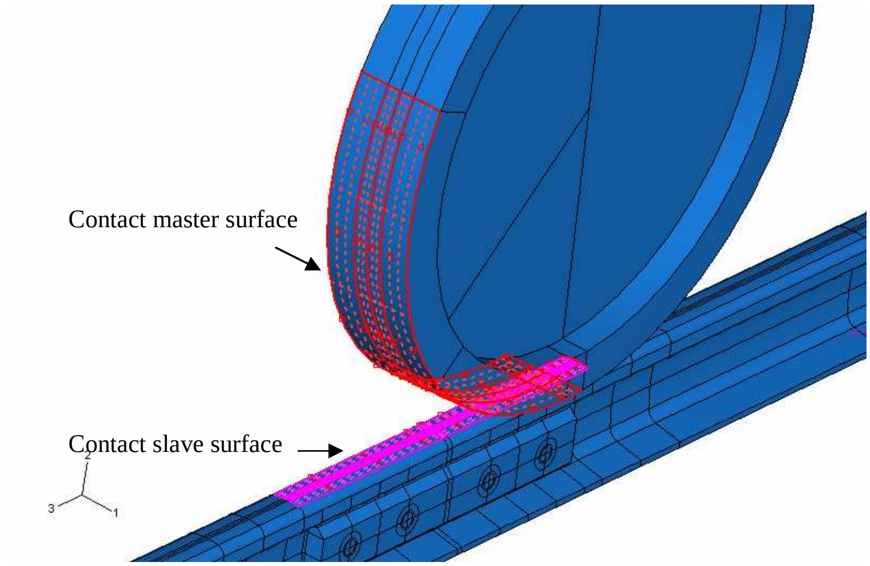

Figure 4.24 Contact surfaces for wheel and IRJ

4.7.1. Contact definition in static model

The Lagrange Multiplier method is used in static analysis for the contact constraint enforcement. Iterations continue until convergence of the solution is obtained. If a slave node penetrates the master surface by more than 0.1% of the characteristic interface length, which is the size of smallest element, the contact pressure is modified according to the penetration and another series of iterations is performed until convergence is once again achieved. Only when the penetration tolerance requirement is satisfied, is the solution accepted.

At the beginning of the contact analysis, there may exist small gaps or penetrations caused by numerical roundoff, or bad assemblies. Adjusting the initial position of the slave contact surface is required to eliminate these gaps or penetrations; otherwise, slave nodes that are overclosed in the initial configuration will remain overclosed at the start of the simulation, which may cause convergence problems. In static analysis, an adjustment zone is defined by specifying an adjusting depth a. The zone extending the distance a in the normal direction from the master surface is termed as the adjustment zone. Any nodes on the slave surface that are within the adjustment zone in the initial geometry of the model are moved precisely onto the master surface as shown in Fig.4.25. The motion of these slave nodes does not create any strain in the model; it is simply treated as a change in the geometry definition. When 'a' is too large, ill contact occurs leading to incorrect stress solutions, especially in the area around the contact surface. On the other hand, when 'a' is too small, contact iteration exhibits sensitivity to the mesh leading to convergence problems.

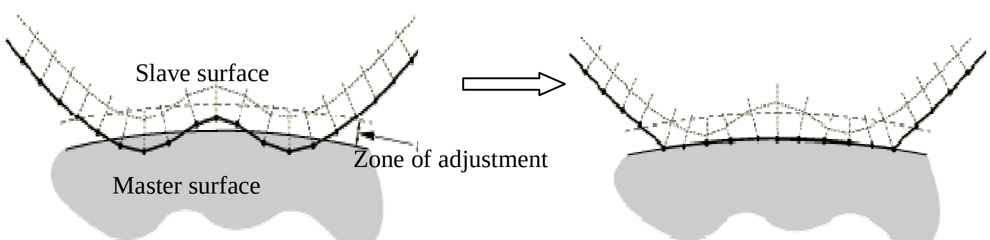

Figure 4.25 Contact surfaces initial adjustment (Abaqus, 2003)

To stabilise the numerical roundoff excited by the rigid body motion, the contact control parameter APPROACH is used to address the problem. This option activates viscous damping in the normal direction to prevent numerical difficulties associated with the rigid body motion that occurs when surfaces that are not initially in contact are brought into contact.

4.7.2. Contact definition in dynamic analysis

In ABAQUS/Explicit, two contact constraint enforcement methods, namely, the Penalty method and Kinematic method are available. Both methods were performed and results compared. The Penalty method is chosen because of the better performance (results are presented in the Chapter 5).

4.8. Strategy-6: Meshing

Meshing is an important part of FE modelling which has a strong influence on the reliability and accuracy of results as well as the model efficiency. Refined mesh usually provides more accurate results than coarse mesh. However the refined mesh increases the computational cost significantly. Hence, some meshing strategies are employed to set up a reliable FE model with reasonable cost. For the parts which undergo high level loading or stress, refined mesh is necessary. On the other hand, for the parts which are away from the severe loading or stress condition, coarse mesh is suitable to reduce the model size.

The whole FE model contains 3 major parts: wheel, IRJ solid part and IRJ beam part. For the wheel, the zone close to the wheel/rail contact patch is partitioned and assigned the refined mesh. The zone in the wheel tread is partitioned in such a way that a circle with 25mm radius extrudes along the wheel circumference as shown in Fig. 4.26 (a). Another partition is made in the wheel tread as shown in Fig. 4.27 (b). The circumference length of this partition is the product of wheel rotating velocity and simulation duration. The refined mesh is in the intersection zone of these two partitions with the element size of 2.5mm. The wheel meshing is presented as Fig. 4.27.

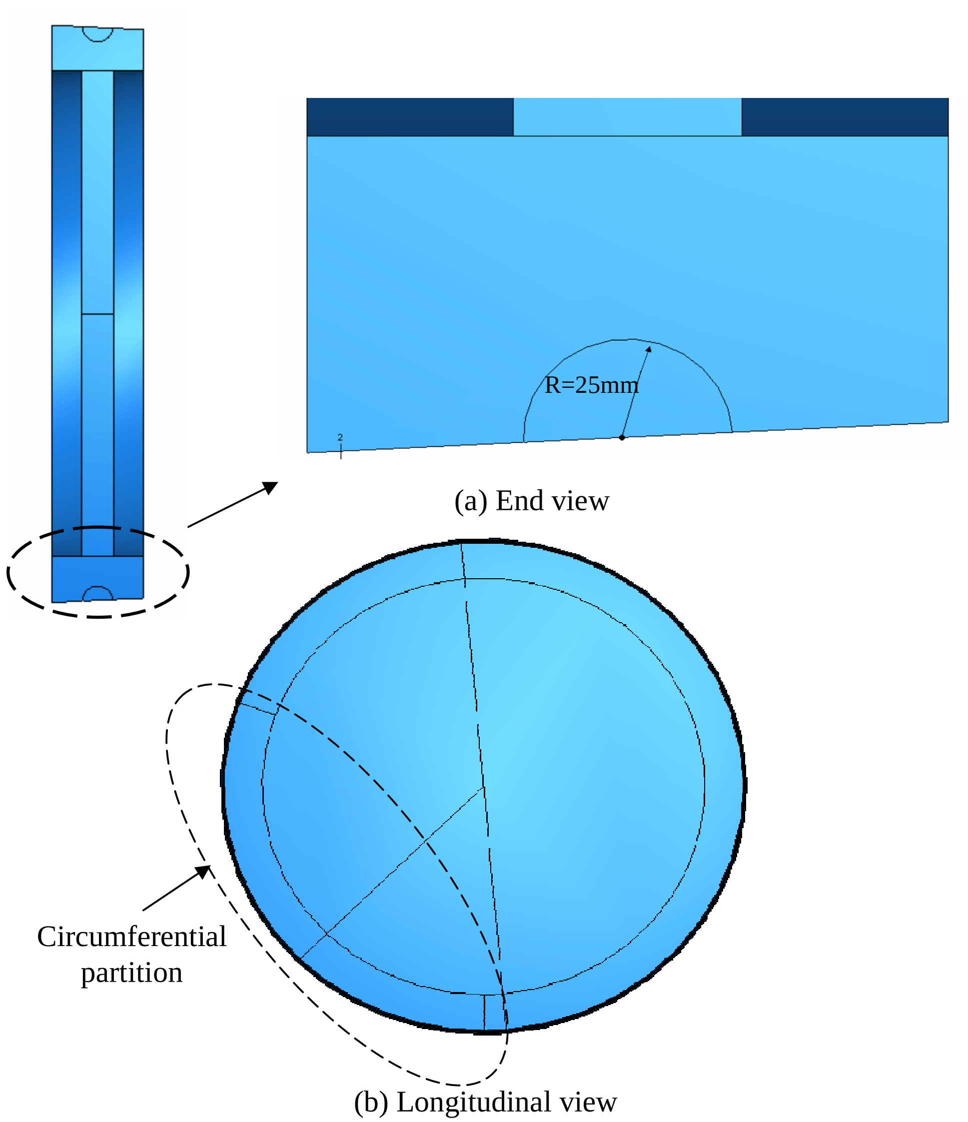

Figure 4.26 Wheel partition

The beam part for the IRJ is discretised using beam elements with a size of 200mm with a total number of 60. The two node linear Timoshenko shear flexible beam element B31 in the ABAQUS element library is employed with ABAQUS.

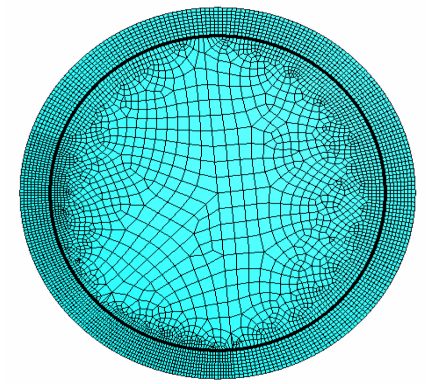

(a) Longitudinal view

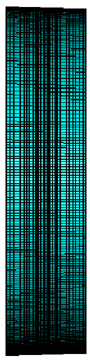

(b) End view

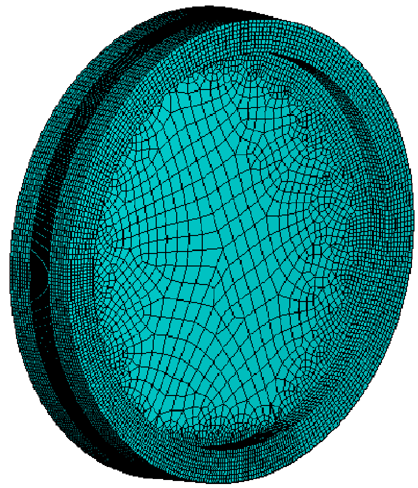

(c) Isometric view

Figure 4.27 Wheel meshing

The solid part of the IRJ consists of two major zones. One zone is part of the railhead in the vicinity of the end post with a longitudinal length of 658mm, referring to Fig. 4.28. The rail head zone is generally assigned with refined mesh with the element size of 4mm. A further partition is made in the central top part of the railhead to obtain a more refined mesh for the wheel/rail contact zone. In this zone the element size is approximately 0.5mm.

The rest of the IRJ (Fig. 4.30) is generally assigned with coarser mesh. The element size in this part, except the partition for bolt shank, is approximate 5mm. Because of the high level of bolt pretension load, the partition of bolt shank is assigned a refined mesh with the element size of 2.5mm. The partition for end post zone is also assigned with a refined mesh with an element size of 2.6mm.

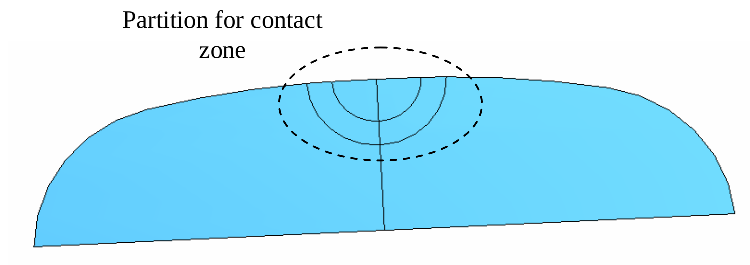

(a) End view

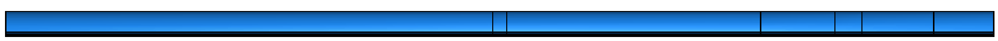

(b) Longitudinal view

Figure 4.28 Railhead zone of IRJ

The mesh of the railhead zone is shown in Fig. 4.29.

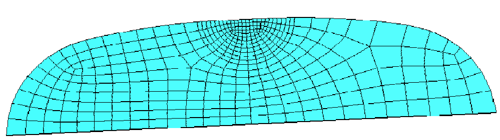

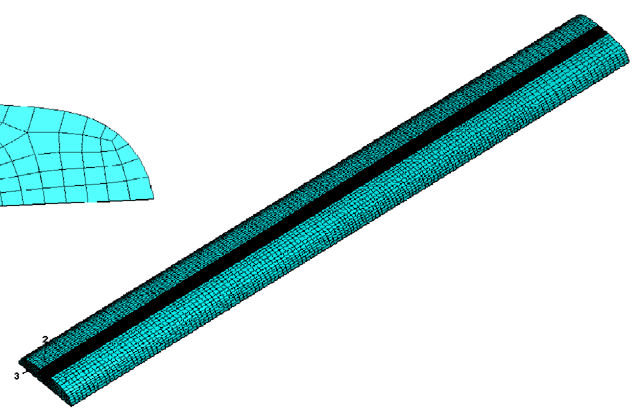

(a) End view (b) Isometric view

Figure 4.29 Refined mesh for railhead zone of IRJ

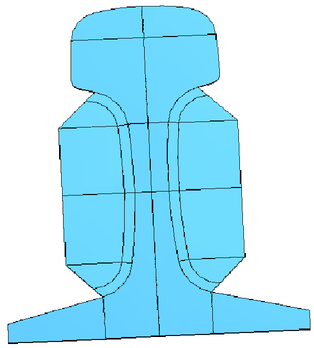

(a) End view

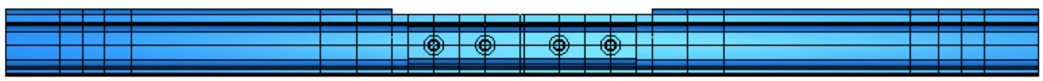

(b) Longitudinal view

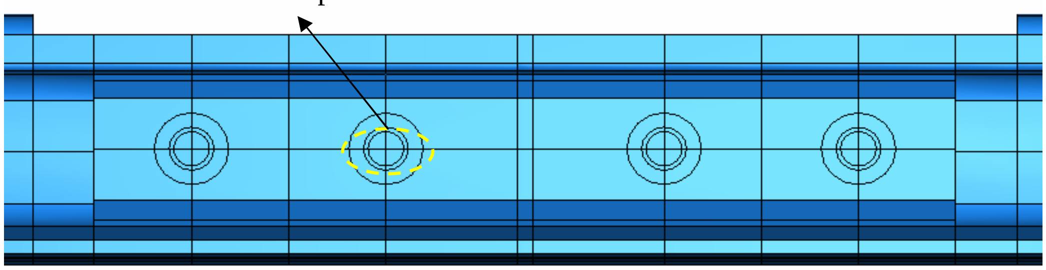

(c) IRJ zoom-in

Figure 4.30 Remaining part of IRJ

The meshing of the IRJ without the railhead partition is presented in Fig 4.31. The railhead partition is connected to the other parts of the IRJ at their intersection surfaces using coupling technique. All 3 coupling DOFs on the surfaces are arrested.

The full FE wheel and IRJ contact model is presented as Fig. 4.32. The entire FE model consists of 169,655 nodes and 147,322 eight-node linear hexahedral solid elements with reduced integration C3D8R. Table 4.2 presents the mesh information for different parts.

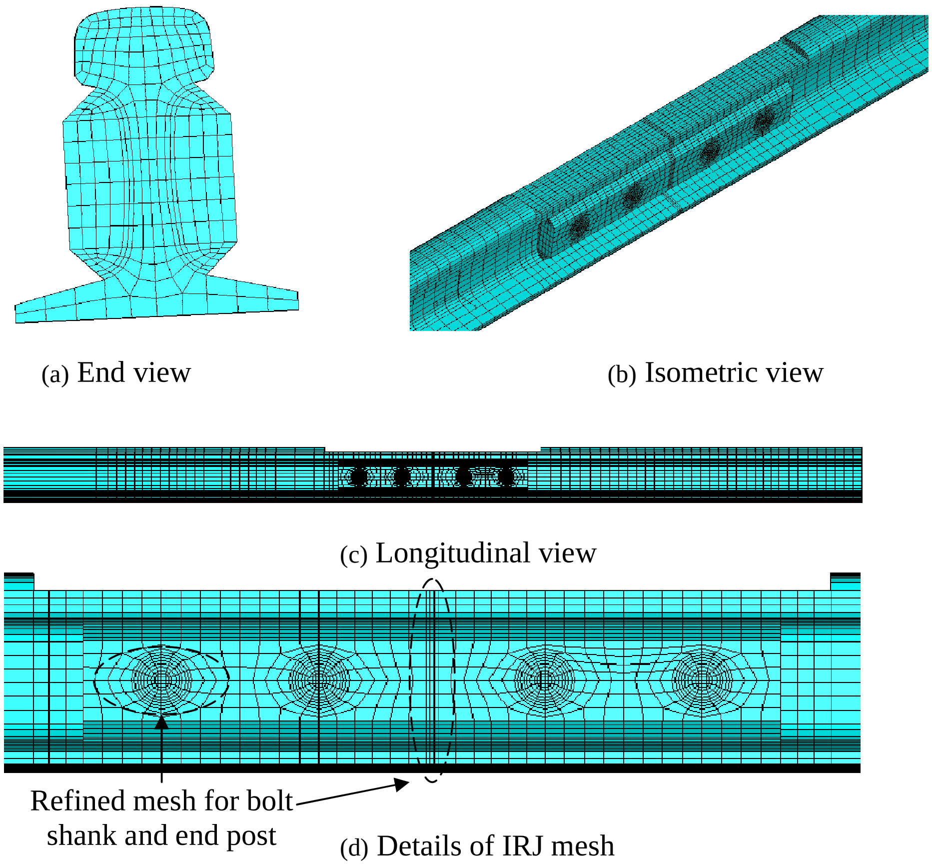

Figure 4.31 IRJ elastic zone meshing

Table 4.2 mesh of wheel/IRJ contact model

Part name		Number of elements	Number of nodes	Max size of elements in the refined zone
Wheel		56,606	65,865	2.5mm
IRJ	Beam part	46	48	230mm
	Railhead of solid part	56,625	63,080	0.5mm
	Rest of solid part	32,216	38,635	2.5mm

(a) Longitudinal view

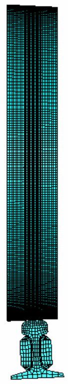

(b) End view

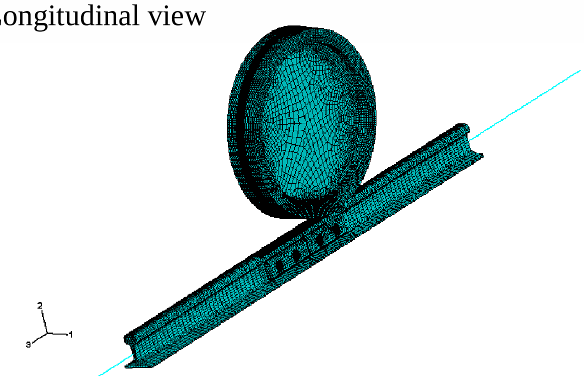

(c) Isometric view

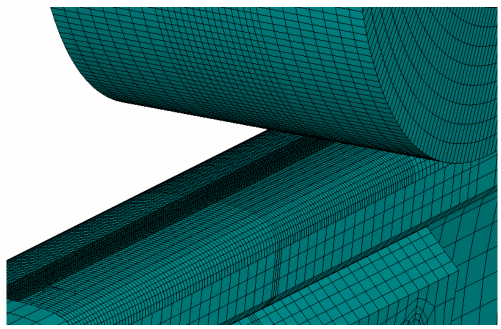

(d) Enlarged view for wheel/IRJ contact

Figure 4.32 Finite element meshing of the wheel-rail system

4.9. Summary

The FE modelling of wheel/rail contact impact in the vicinity of the end post has been introduced in this chapter. The 3D full scale wheel/rail contact model employs a two-step analysis strategy, from static to dynamic, to achieve a steady contact condition prior to impact analysis. To achieve a reasonable model size which is acceptable to the available computing facility, several model idealisation and simplification strategies are employed in following aspects:

- wheel profile and IRJ assembly
- material modelling
- boundary conditions

Some special attention is also paid to the following FE modelling strategies:

- loading strategy
- contact modelling strategy
- meshing strategy

With the employment of above strategies, the FE model is set up and the numerical example for wheel/rail contact impact at the IRJ is presented in next chapter.

5. FE Evaluation of Contact-Impact Forces

5.1. Introduction

This chapter reports numerical examples of wheel/rail contact impact at IRJs obtained using the FE model described in the previous chapter. The results of the examples are presented as the wheel-rail contact force time histories. The contact patch parameters, the peak contact pressure and the contact distribution away from and close to the end post are also discussed; where possible comparisons are made with Hertzian contact theory. The effects of some selected IRJ design parameters to the magnitude of the impact force are studied through several sensitivity analyses.

5.2. Numerical Example: Typical Input Data

All simulations are run on the Altix 3700 BX2 super computer installed at the Australian Partnership for Advanced Computing (APAC), Canberra. The system contained CPU type Itanium2 (1.6GHz) and the maximum memory allowance for each run has been 4069Mb. Typical computational time for the combined static and dynamic analysis was 35 hours, of which the dynamic analysis took 28 hours.

A wheel with a vertical load of 150KN (corresponding to gross wagon mass of 120 tonnes) was assumed to travel at a speed of 120km/h over the IRJ. Although most freight wagons and all coal wagons run at a maximum spend of 80 km/h, a higher speed (120km/h) was adopted to reduce the duration of travel for simulating the required travelling length of 400mm. The example with a lower speed (<80km/h) corresponding to the field test is reported in Chapter 7.

Fig. 5.1 shows the load and boundary conditions used in the static analysis. The bolt pretension load of 200KN corresponding to the torque of 1050Nm was applied to the bolt shank and the wheel load of 150KN was applied vertically downwards at the axis of the wheel (identified as B in Fig. 5.1). In the static analysis, the wheel/rail contact position was located at 218mm away from the IRJ centre (shown in Fig. 5.1).

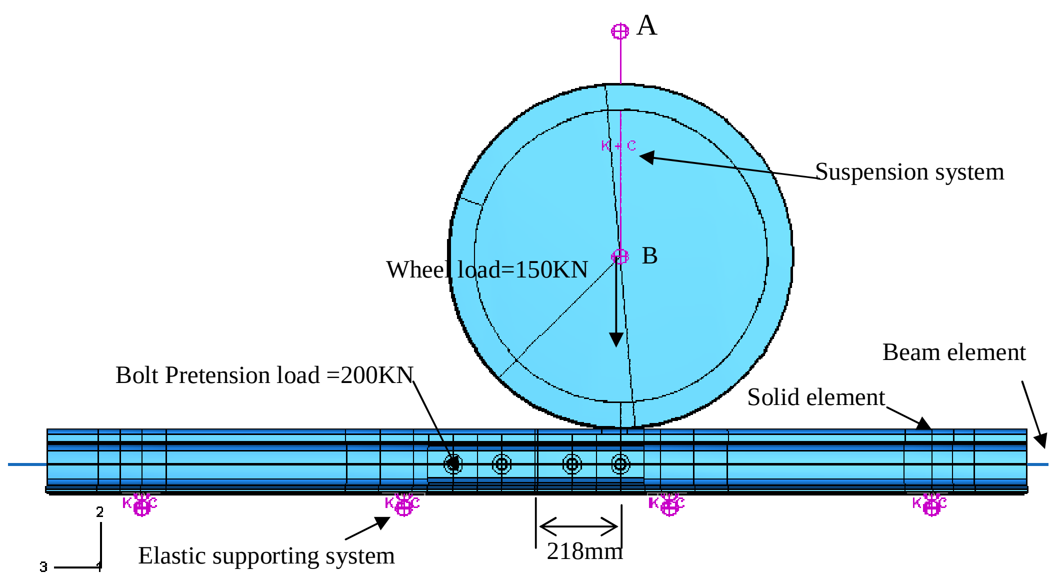

Figure 5.1 Typical wheel/rail static contact model of IRJ

For the purpose of smooth transfer of static analysis results into dynamic analysis input data, it was required to apply the centrifugal force (see Fig. 4.23) due to the steady state velocity of the wheel in the static analysis. This was achieved by prescribing the velocity at Point B in ABAQUS/CAE. The mass of the wagon shared by the wheel was also applied (at point A in Fig. 5.1) to enable smooth transfer of the static results into the dynamic analysis input data.

In the dynamic analysis, the model was preloaded by transferring the results from the static analysis. The longitudinal speed 120km/h and the rotational angular speed 72.46 rad/s were applied to the wheel as the initial conditions. A similar approach is also adopted for the simulation of automobile tyre-road interaction problems (ABAQUS, 2003). Initial condition instabilities were minimised by allowing the wheel to roll a sufficiently long distance (218mm) prior to impacting the IRJ. The total duration of this simulation in real time was 12ms.

The mechanical properties of the material are shown in Table 5.1. In this example, the end post thickness was kept as10mm and the end post material was assumed glued to the rail ends for simplicity. The suspension system and the elastic supporting system were modelled as spring/dashpot sets, and their mechanical properties are shown in Table 5.2.

Table 5.1 Mechanical properties of steel and insulation material (Chen, 2002)

Property	*Steel*	*Nylon66*
Young's modulus	210GPa	1.59GPa
Poisson's ratio	0.3	0.39
Density	7800kg/ m^3	1140kg/ m^3
Yield Stress	780MPa	_

Table 5.2 Properties of the Supporting and Suspension system (Wen, 2005)

Elastic support system	Suspension system
Stiffness K_b (MN/m) 26.8	Stiffness K_s (KN/m) 220
Damping C_b (KNs/m) 14.5	Damping C_s (Ns/m) 138

5.3. Typical Results

In this section, typical results of static and dynamic analysis are presented. The static results are presented first; the contact impact force obtained from the dynamic analysis is presented later.

The results are presented with two main objectives; first to provide some confidence that the results are indeed plausible, and second to ensure that an engineering interpretation of the results is possible. In order to demonstrate the plausibility of the results, fine meshes were used, especially in the static analysis. Unfortunately these fine meshes could not be adopted for the complete analysis, especially for the dynamic explicit analyses, due to the limitation of the super computing facilities provided for the project. It should be remembered that the dynamic solution could only be obtained after 28 hours of computer CPU time with coarse mesh. Therefore, even with larger resources, fine meshes would not have been economically viable.

5.3.1. Results of static analysis

First the contact pressure contour obtained from the elastic and the elasto-plastic analyses are presented and compared with the HCT as shown in Fig. 5.2. The dashed ellipse represents the HCT contact patch. Table 5.3 presents the dimensions of the major and minor axes of contact areas, as well as the contact area (πab) and the peak pressure obtained from the elastic and elasto-plastic FE analyses and that of the HCT.

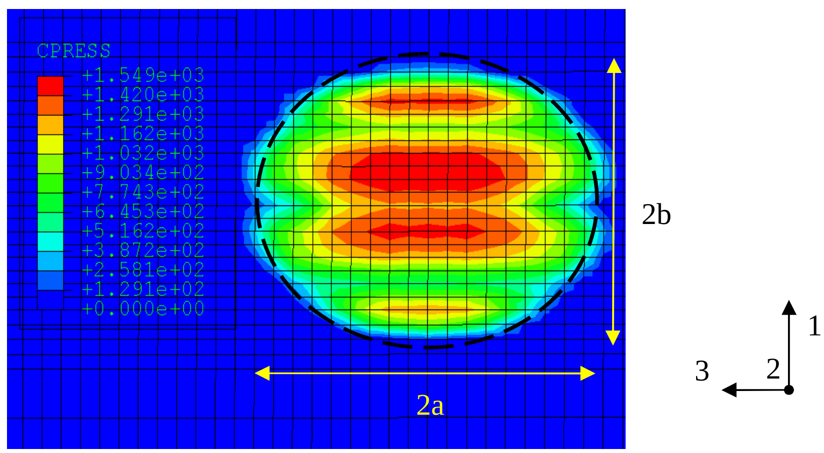

(a) Elastic FEA

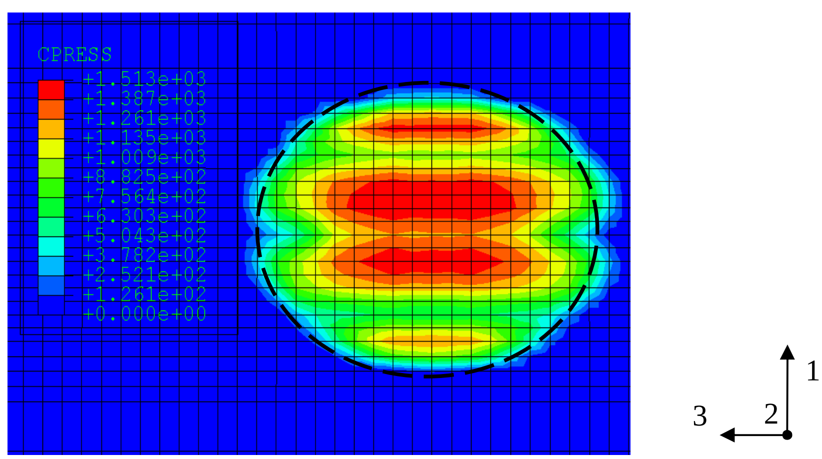

(b) Elasto-plastic FEA

Figure 5.2 Contact pressure distributions

Table 5.3 HCT and FEA comparison

	HCT	Elastic FE		Elasto-platic FE	
	Values	Values	% Diff.	Values	% Diff.
Major axis a	$7.9\,mm$	$8.5\,mm$	7.6%	$8.5\,mm$	7.6%
Minor axis b	$6.3\,mm$	$6.0\,mm$	4.7%	$6.0\,mm$	4.7%
Contact area A	$157\,mm^2$	$161\,mm^2$	2.5%	$162\,mm^2$	3.2%
Peak pressure P_0	1434MPa	1549MPa	8.0%	1513MPa	5.5%

It is notable that all parameters of the contact patch obtained from the elastic and elasto-plastic analyses compare well with that of the HCT. Further refining of the mesh would have reduced the percentage difference between the FE results and the HCT predictions. However such attempts were not carried out as even the mesh shown in Fig. 5.2 had to be made coarser for the dynamic analyses for reasons explained earlier.

One interesting observation is that the FE analyses have predicted slightly larger contact areas as well as higher contact pressures. Indeed both methods must satisfy static equilibrium for the applied wheel load of 150 KN. To examine the matter further, the HCT and FE pressure distributions are compared in Fig. 5.3. From the non-continuous distribution of the contact pressure predicted by the FE (especially along the minor axis), the reason for higher peak contact pressure becomes obvious. It should also be realised that the HCT is an overly idealised theory and hence its prediction of smooth, continuous distribution of pressure should be treated carefully. As an idealised theory, the HCT pressure distribution could be regarded as ‘average’ from Fig. 5.3.

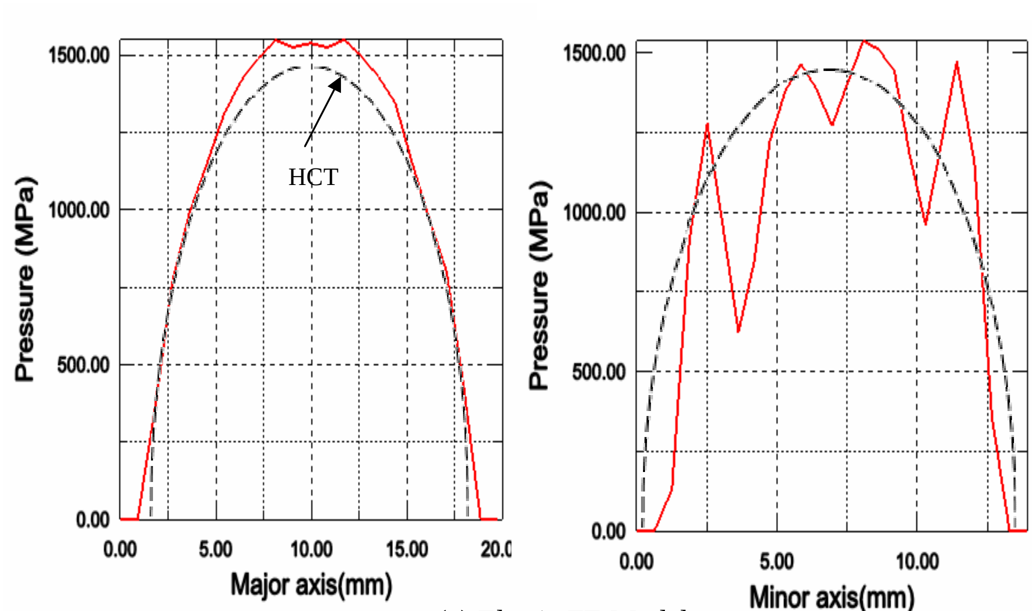

(a) Elastic FE Model

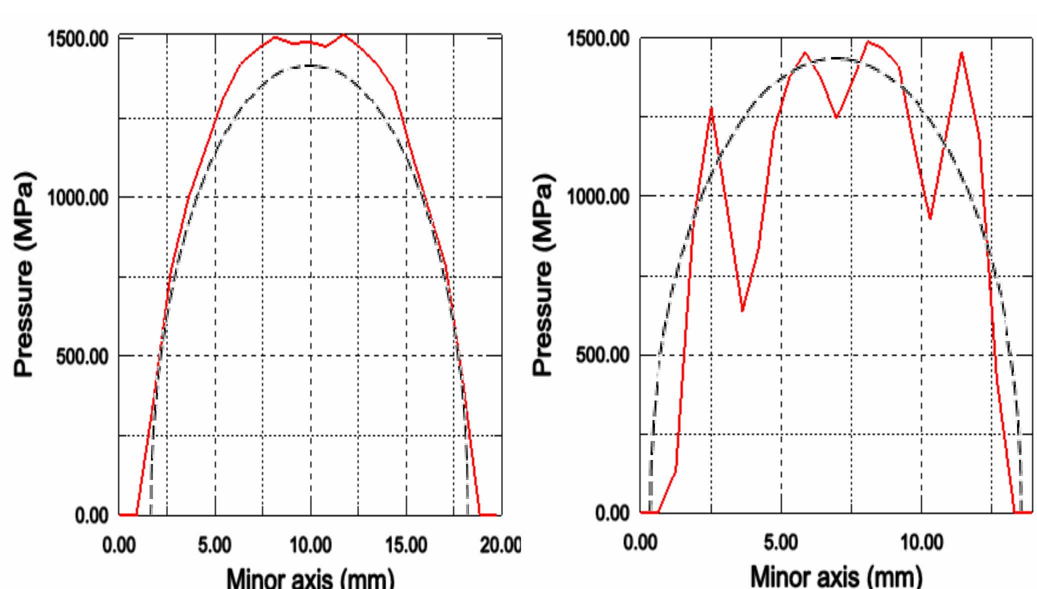

(a) Elasto plastic FE Model

Figure 5.3 Contact pressure distribution X-Y plot

Another observation to make is the effect of plasticity to peak pressure; only a marginal reduction in peak pressure has occurred due to the load of 150KN being just sufficient to initiate the plastic deformation as shown in Fig. 5.4. Higher loads would have caused reduced pressure with the corresponding enlargement of contact area. Such analyses were not carried out as the main objective of the FE model was limited to the determination of the contact impact forces in the vicinity of the end post. The reason for the elaborate discussion of the contact patch is primarily to demonstrate that the FE contact model is appropriate.

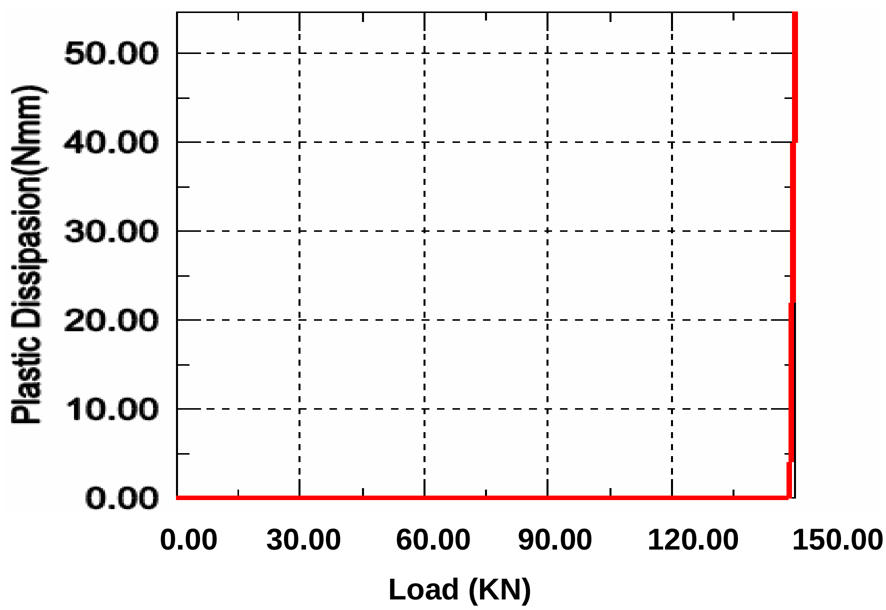

Fig 5.4 Plastic energy history

Unfortunately, as described above due to computational resource limitations, the mesh that has provided good static results (from the contact patch perspective) is not affordable in the dynamic analysis. In order to run the dynamic model within the constraints of available resources, the mesh was made coarser. The refined mesh used in the above two cases and the coarser mesh adopted for further analyses in the contact zones are shown in Fig. 5.5. It shows that the element size is enlarged by four times in the longitudinal direction (along axis 3) while in the radial and vertical directions the element size has been kept unaltered.

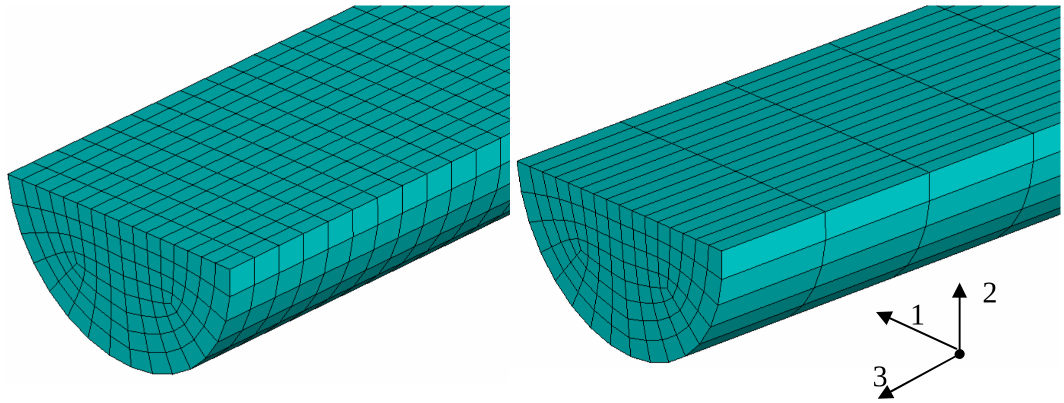

(a) Refined Mesh $0.9mm \times 0.5mm \times 0.5mm$ (b) Relaxed Mesh $3.6mm \times 0.5mm \times 0.5mm$

Figure 5.5 Mesh in the contact zone

The contact pressure distribution was obviously altered due to the coarser mesh as presented in Fig. 5.6. The analysis considered elasto-plastic rail steel properties. It indicates that due to the coarser mesh the contact area is enlarged by 17.3% ((190-162)/162) and the peak pressure is reduced by 10.6%((1513-1352)/1513). However, the results reported in the next section on dynamic analysis shows that the contact force and peak pressure are still sufficiently accurate.

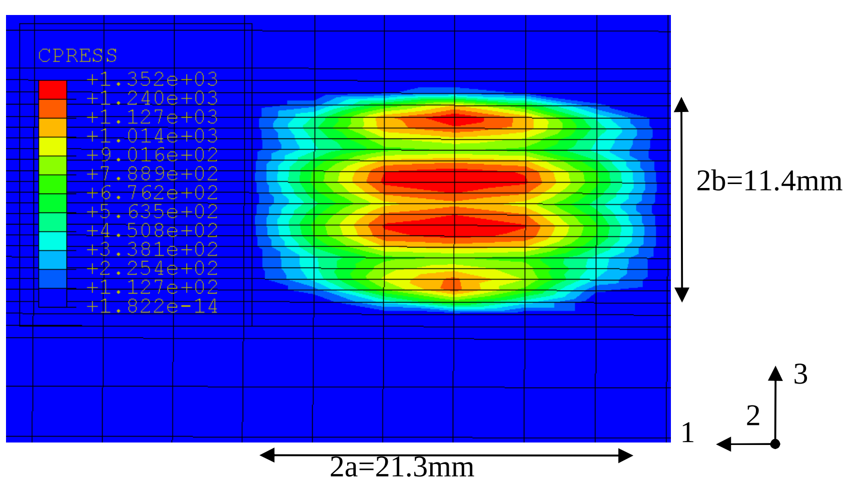

Figure 5.6 Contact pressure distribution of coarse mesh

5.3.2. Results of dynamic analysis

ABAQUS/Explicit permits two methods for contact constraint enforcement: the Penalty method and the Kinematic method. The effectiveness of these two methods was first examined. Fig. 5.7 indicates that both methods produce the same magnitude of the impact force, 174KN. However, the contact force history due to the Kinematic method has exhibited more severe vibration than that due to the Penalty method. This might have been associated with the algorithm of the Kinematic method that advances the kinematic state of the model into a predicted configuration *without considering the contact conditions*. The computational times of these two methods are fairly similar. The Kinematic method is therefore not chosen for further analyses because of its severe numerical vibration; all calculations carried out and results reported in this thesis were based on the Penalty method.

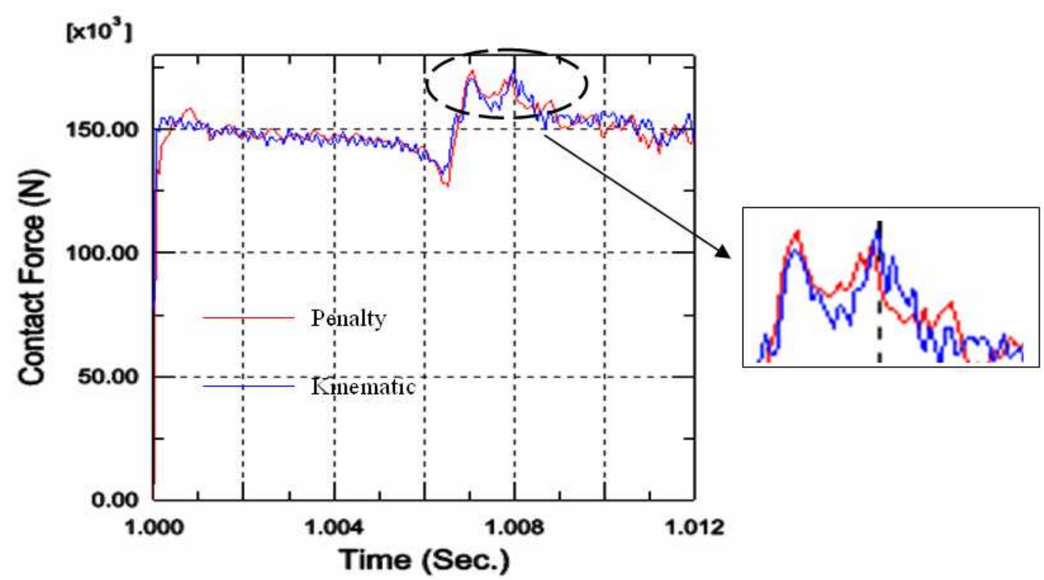

Figure 5.7 Contact force history using Penalty method and Kinematic method

(a) Contact forces

Dynamic analysis of the IRJ has provided the railhead/wheel contact force time history, which is shown in Fig.5.8.

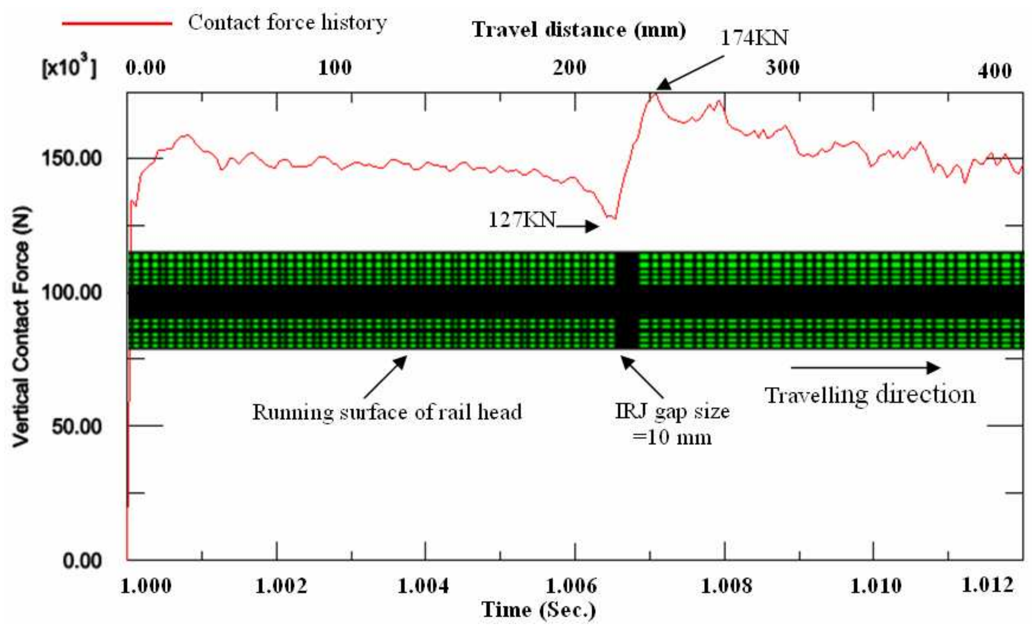

Figure 5.8 Rail/wheel contact force history

Fig.5.8 shows that, at the beginning of the dynamic analysis, the contact force has increased sharply just above 150KN and stabilised to the static wheel load value of 150kN after a short period of approximately 1.2 milliseconds. As the wheel approached the end post, a drop in the contact force (127kN) occurred due to the local deformation of the edge of the railhead that is affected by the difference in the material properties between the two interacting materials (rail steel and endpost Nylon). Within 0.54 millisecond the contact force increased from 127kN to 174kN (or 37%) indicating the occurrence of the rail/wheel contact-impact. The impact occurred at 7.1 millisecond since the start of the wheel travel with the corresponding impact factor of 1.16 (calculated from the quotient of impact force on static load (1+(174-

150)/150)). The concept of wheel/IRJ contact impact is described previously in Chapter 2 Section 2.6 (See Fig. 2.14).

It is believed that the wheel impact at the rail edge is due to the momentary "loss" of contact leading to wheel flight across the end post with the wheel landing on the edge of the other railhead. The exact location of the wheel tending to lose contact and re-landing on the railhead can not be precisely estimated from the FE model. As 0.54 millisecond of "flight time" of the wheel travelling at 120km/h corresponds to 18.0mm which is larger than the end post (10mm gap) thickness, it is inferred that the hypothesis of wheel impact in the vicinity of the end post is approximately validated. After the impact, the contact force has gradually damped down to the static wheel load level of 150 KN. It should also be observed from Fig. 5.8 that the post impact history is associated with high frequency noise, which was relatively calm in the pre-impact stage. This again reinforces that the wheel has actually caused impact at the forward section of the railhead.

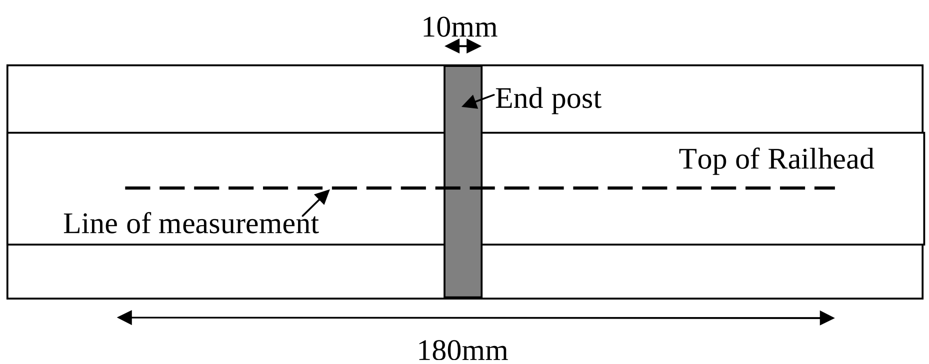

Figure 5.9 Measurement line on the top of railhead

The inferences discussed above can be further proven with the displacement profile of the IRJ as the wheel passing over the joint. The line of measurement is selected through the nodes at the top centre line of railhead surface as shown in Fig. 5.9. The displacement of the selected nodes on this line is shown in Fig. 5.10.

Fig. 5.10 demonstrates that during pre-impact, Rail 1 has a lower profile than Rail 2 as the wheel load is primarily distributed on Rail 1. It shows that the end post was severely compressed by the uneven forces from the two rails which leads to a pop-up zone close to Rail 2. Because of the higher profile of Rail 2, the approaching wheel would hit Rail 2 severely at the edge of Rail 2 which is considered as an impact. At the moment of impact, the end post material under wheel contact loading dipped down significantly more than the two rail ends due to lower modulus. This deformed profile illustrates that only two point contact of the 460mm radius wheel in the vicinity of the end post as hypothysed in Section 2.6 would be possible. During the post impact stage, the deformation profile appears mirror-imaged to that of the pre impact behaviour.

(b) Contact pressures and dimensions

Contact pressure distribution at the top of the railhead obtained during one of the increments of the rolling of the wheel, corresponding to the pre-impact stage, is shown in Fig. 5.11. The shape of the contact pressure zone appears approximately elliptical with the major axis oriented along the longitudinal direction (shown by the single headed arrow) of travel. The dimension of the contact ellipse (a=10.35mm, b=6.35mm) is close to the static analysis using coarse mesh (see Fig. 5.6 in which a=10.65mm and b=5.70mm).

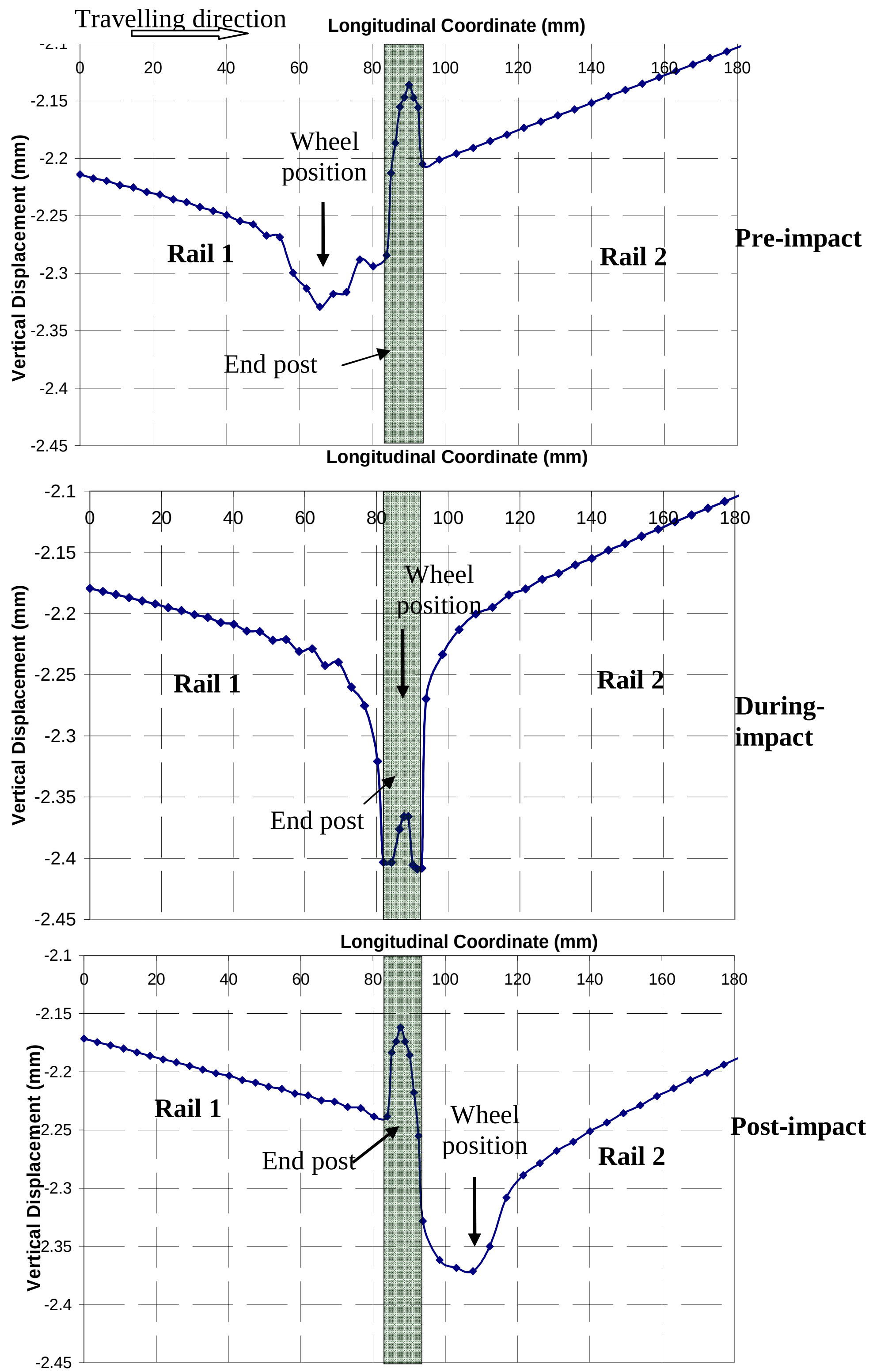

Figure 5.10 IRJ vertical displacement with wheel passing over the joint gap

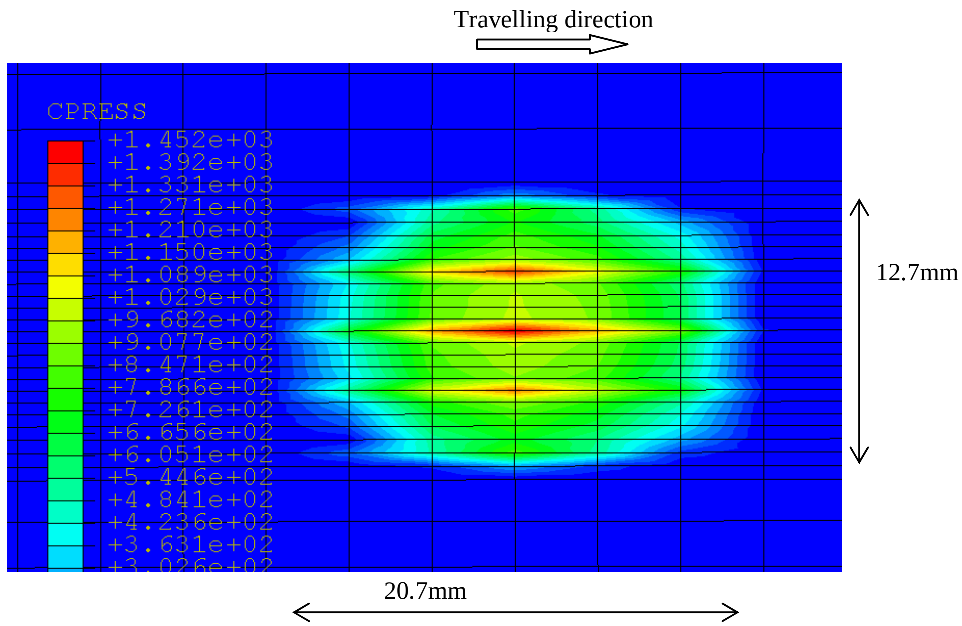

Figure 5.11 Contact pressure distribution (pre impact)

The peak pressures of the dynamic and static analyses obtained from the coarse mesh are 1352MPa and 1452MPa respectively. It is apparent that the dynamic rolling of the wheel has narrowed the peak pressure zone (compare the red contours of Fig. 5.11 and Fig. 5.6) with the corresponding increase in the peak pressure. As peak pressure is perhaps the most important parameter that affects the damage, its determination using dynamic analysis appears more appropriate, as this is likely to provide a less conservative estimation of the damage.

The contact pressure on the railhead was monitored throughout the travel of the wheel. Until the wheel approached the edge of the IRJ (closer to the end post), the contact pressure shape remained approximately elliptic. When the wheel just crossed the IRJ, the shape of the contact pressure distribution has shown two point contact of the wheel spanning across the IRJ as illustrated in Fig. 5.12. The maximum contact pressure in this case was 1231MPa.

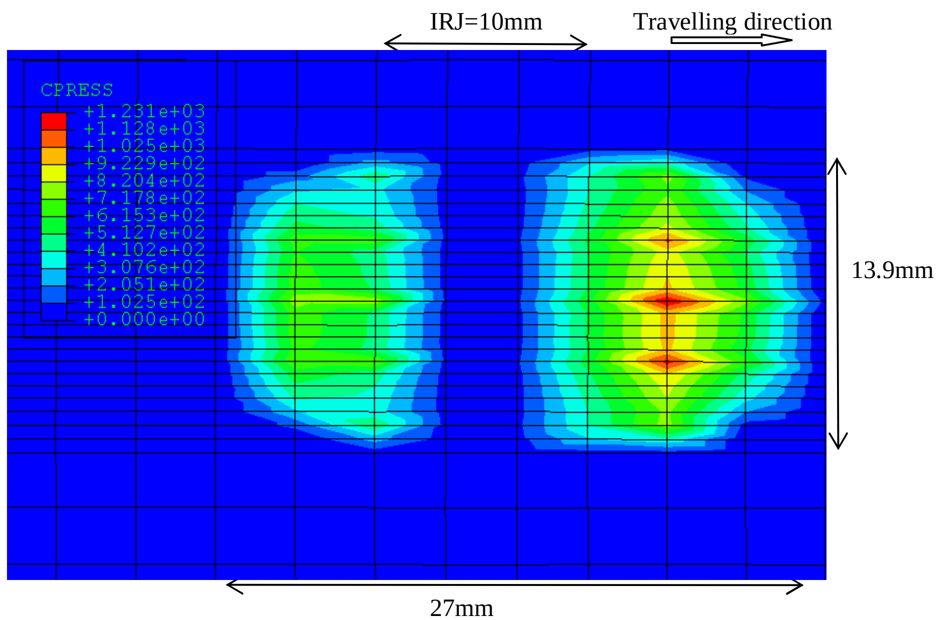

Figure 5.12 Contact pressure distribution (during impact)

Fig. 5.12 shows that the contact area was divided into two parts and the middle part corresponding to the end post was considered out of contact. In this situation, the continuous contact surface assumption of HCT was violated. This figure together with Fig. 5.10 infer that, at the time of impact, the wheel and rail are under a condition of ‘two-point contact’ in contrast with the ‘single-point contact’ beyond the vicinity of the end post. The post-impact contact pressure distribution on the railhead is shown in Fig. 5.13. It indicates the peak pressure of 1495MPa and the elliptical dimensions of major and minor axis are close that of the case just prior to impact as shown in Fig. 5.11.

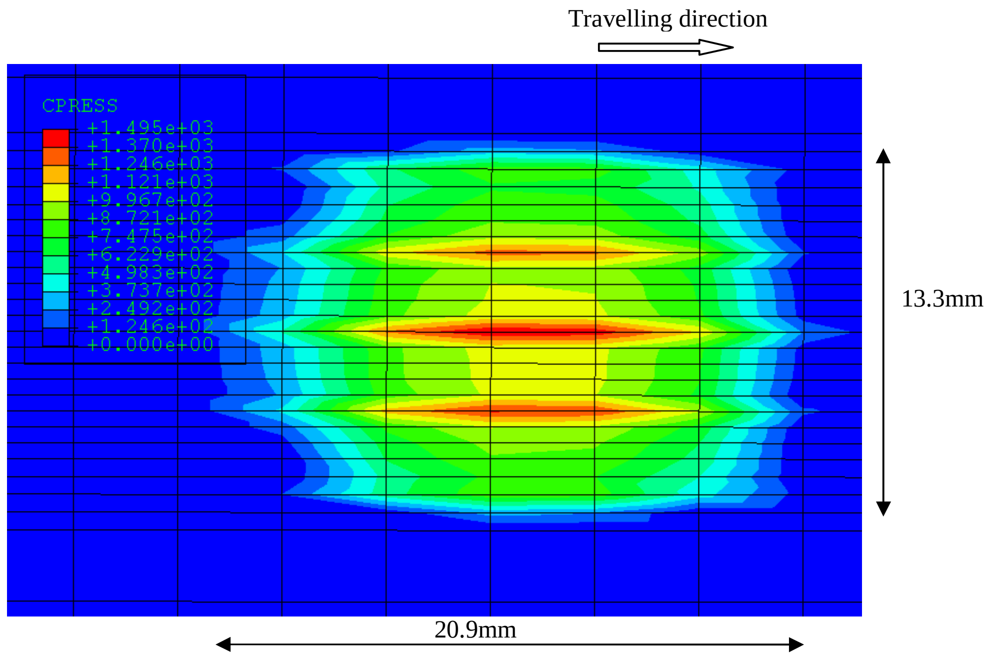

Figure 5.13 Contact pressure distribution (post impact)

The area of the contact patch obtained at each increment of the explicit analysis is plotted as a time history in Fig. 5.14. In this figure the contact area predicted by the HCT is also shown (as the horizontal straight line). Whilst the HCT predicts the area as 160 mm^2, the explicit dynamic analysis predicted areas varied around a value of approximately 260 mm^2 prior to impact, and has registered a sharp increase in the contact pressure area to 450 mm^2 at the time of impact, and 280 mm^2 post impact. The consistent deviation between HCT and FE results is primarily due to coarse mesh. Based on the discussion in Section 5.3.1, should the mesh be refined it is believed that the contact area pre and post impact would be fairly close to the HCT.

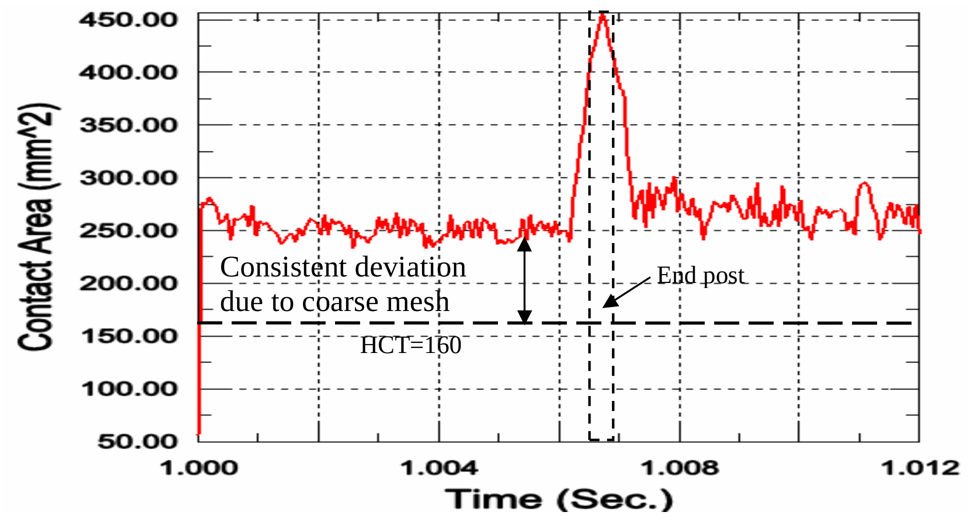

Figure 5.14 History of total area of contact

The time series of the maximum contact pressure is shown in Fig. 5.15. Except for the influence of the initial conditions, the contact peak pressure P_0 determined from the explicit FE analysis has exhibited reasonable agreement with that of the HCT analysis until the wheel was located approximately 20mm away from the edge of the rail and then started deviating from the HCT prediction at times of impact. Just after crossing the end post, P_0 has shown a steep raise to 1600MPa. The coarse mesh appear to have not affected the peak pressure significantly.

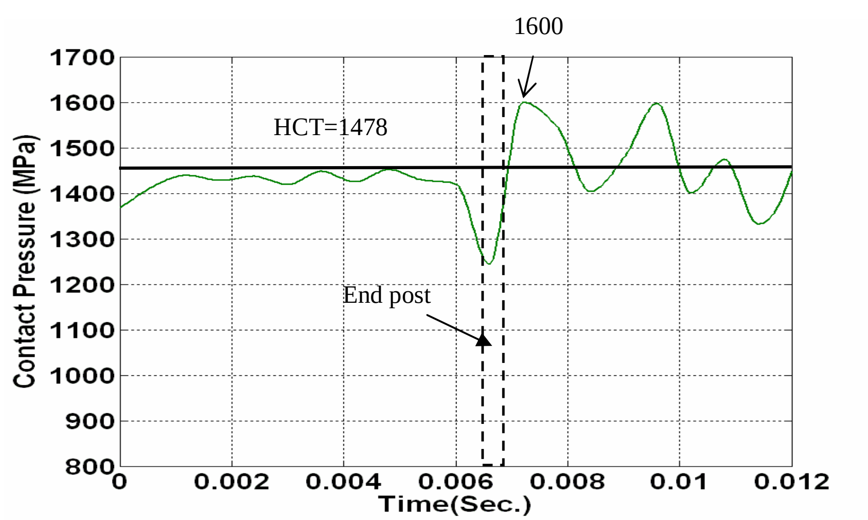

Figure 5.15 Time series of peak pressure P_0

(c) Stresses

The Von-Mises stress distribution presented in Fig. 5.16 shows the most part of the IRJ (excluding the contact patch of wheel and rail) is subjected stresses lower than 150 MPa (which will not cause any plastic deformation). The bolt pretension load has only a localised influence on the IRJ as shown in Fig. 5.16. The magnitude of Von-Mises stress in the bolt zone is also below 200MPa. Through these results, the assumption on the localised plastic zone of the IRJ used in the FE modelling is validated.

Prior to impact, the wheel/rail contact force remained at a stable level that produced a maximum Von Mises stress of 645MPa (the yield stress of steel was 780MPa). The maximum stress occurred at a point 3.75mm below the railhead surface shown in Fig. 5.17&5.18.

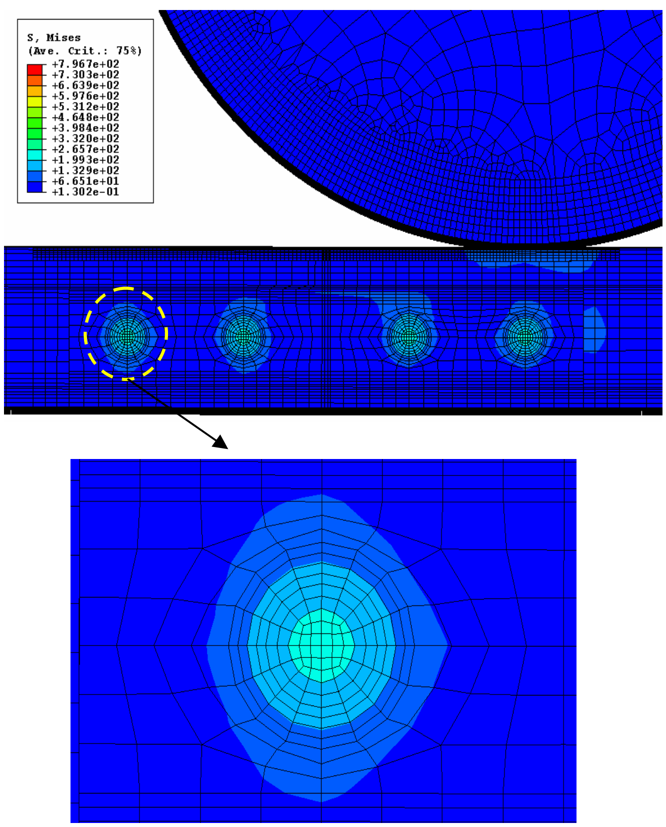

Figure 5.16 Von-Mises stress distribution

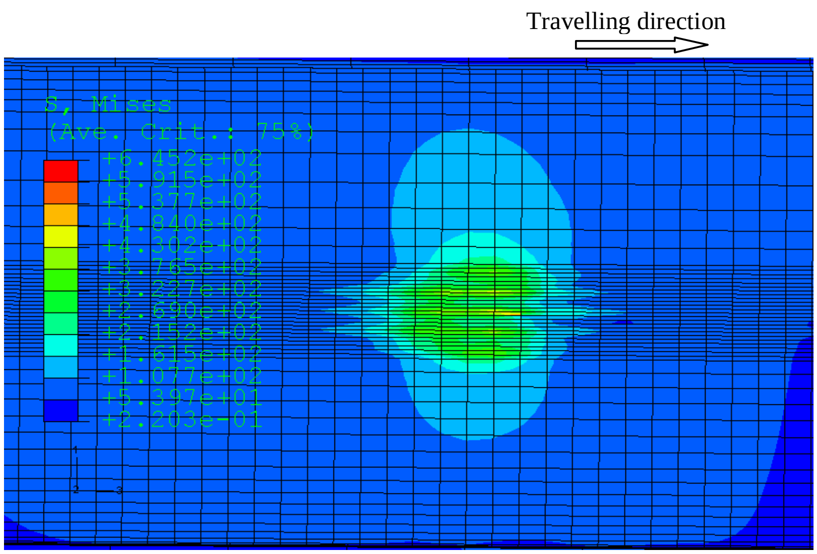

Figure 5.17 Von Mises stress contour (top of rail view) prior to impact

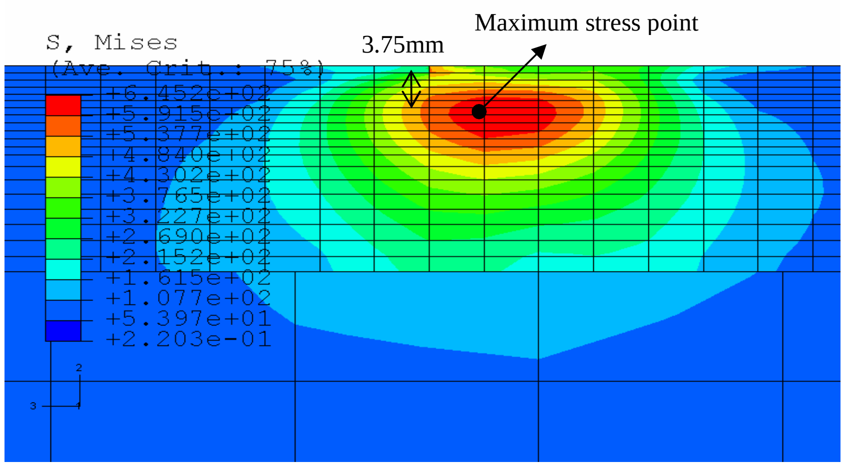

Figure 5.18 Von Mises stress contour (longitudinal vertical symmetric plane through the rail) prior to impact

At the time of impact, the contact force reached its maximum magnitude; the corresponding Von Mises stress distribution is shown in Figs. 5.19 & 5.20. The contours indicate that the Von Misses stress on the surface of the railhead was 668 MPa and the maximum stress of 798.7 MPa (greater than the rail material plastic stress) occurred at 3.19mm below the railhead surface. This shows the impact is the major cause of the initiation of the damage near the edge of the rail in the vicinity of the end post.

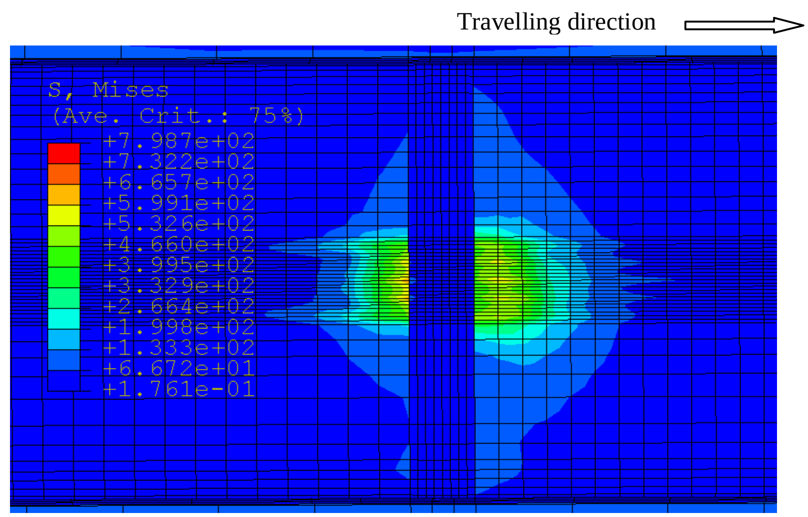

Figure 5.19 Von Mises stress contour (top of rail view) at impact

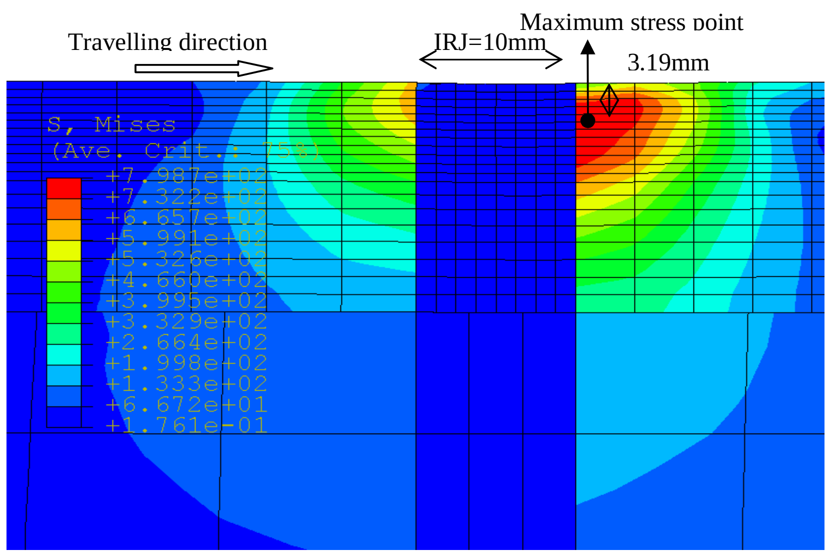

Figure 5.20 Von Mises stress contour (longitudinal vertical symmetric plane through the rail) at impact

The Von-Mises stress distribution post impact is shown in Fig. 5.21&5.22. The maximum stress is 736Mpa and located at 3.02mm beneath the railhead.

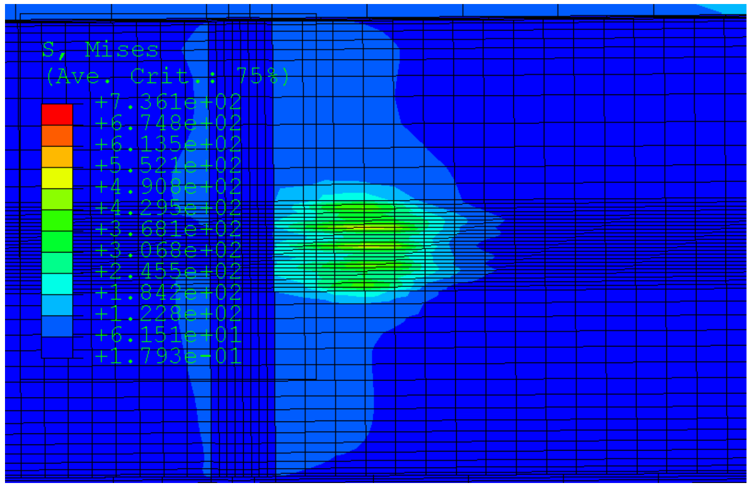

Figure 5.21 Von Mises stress contour (top of rail view) post impact

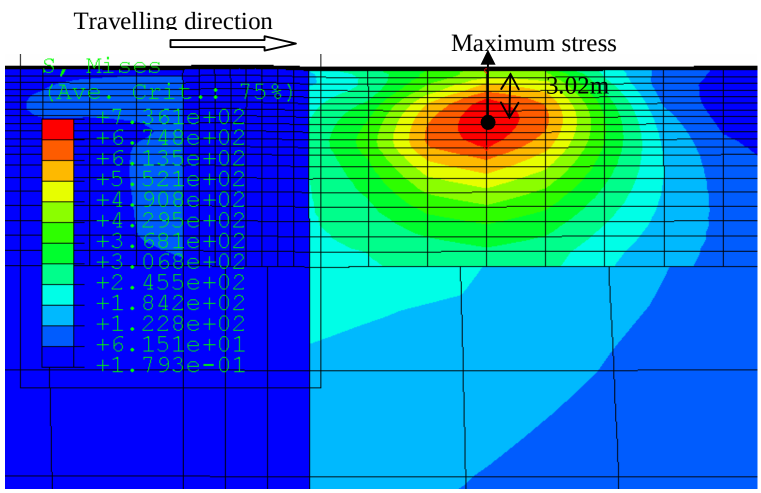

Figure 5.22 Von Mises stress contour post impact

Comparing the results of Von-Mises stress (Figs. 5.17 to 5.22) and contact pressure distribution (Figs.5.11 to 5.13), it appears that at impact, the peak contact pressure reduces (approx. 18.4% and 27.2% relative to pre-impact and post impact respectively) due to an apparent increase in contact area. In spite of the reduction in peak contact pressure, the maximum Von-Mises stress at impact is larger relative to the pre and post impact stages (approximately 21.2% and 12.5% respectively). Discontinuity of rail in the vicinity of the end post appears to be the primary factor influencing the large increase in Von-Mises stresses.

(d) Energies

In this section, kinetic energy ($\frac{1}{2}mv^2$) and plastic energy ($\frac{1}{2}\sigma\varepsilon_P$) time series are presented. The kinetic energy time series of the IRJ is plotted in Fig.5.23. The kinetic energy remained very high throughout the duration of wheel travel due to the significant contribution from the wagon mass which was 15 tonnes or 96% of the mass of the whole model. During the steady state rolling, the kinetic energy recorded a gradual reduction until the impact imparted higher levels of kinetic energy. The maximum peak of the kinetic energy occurred at 8.0 millisecond of travel time, which shows a delay of 0.9millisecond to the time of maximum impact force (Fig. 5.9). This time delay is in accordance to the theory of stress wave propagation in solids. When impact occurred, the stress waves propagated in the solids are reflected back as they reached boundaries. The reflected stress waves cause wheel response and propagated into the entire system. This whole process took some time and caused the time delay.

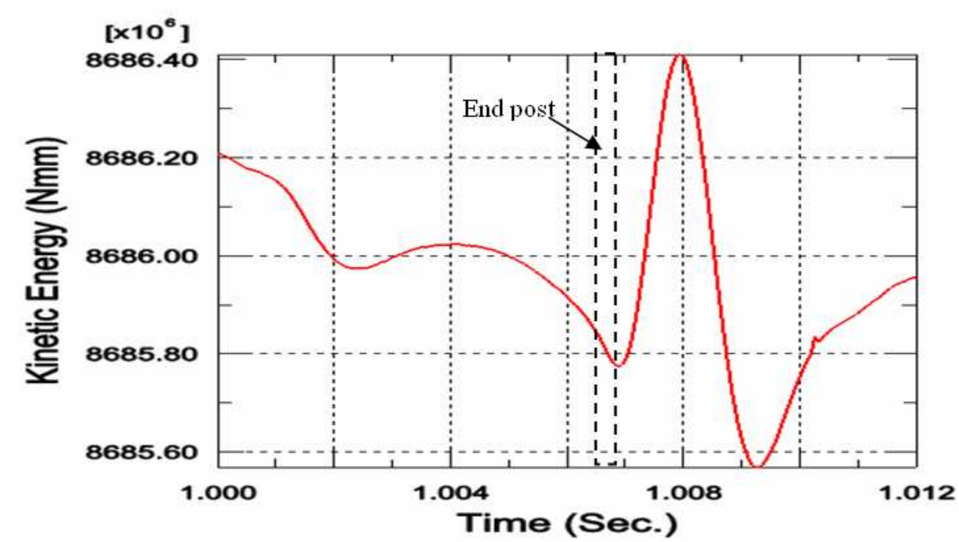

Figure 5.23 Kinetic energy time series

The Plastic energy history is plotted in Fig. 5.24. Impact has sharply increased the plastic strain energy to a higher value that gradually crept to a maximum steady state level towards the end of the analysis. It has been found that the sharp increase of plastic energy occurred between 6.6ms and 7.1ms, corresponding to the impact (Fig. 5.9). This shows that the material is significantly plasticised due to wheel impact almost instantaneously.

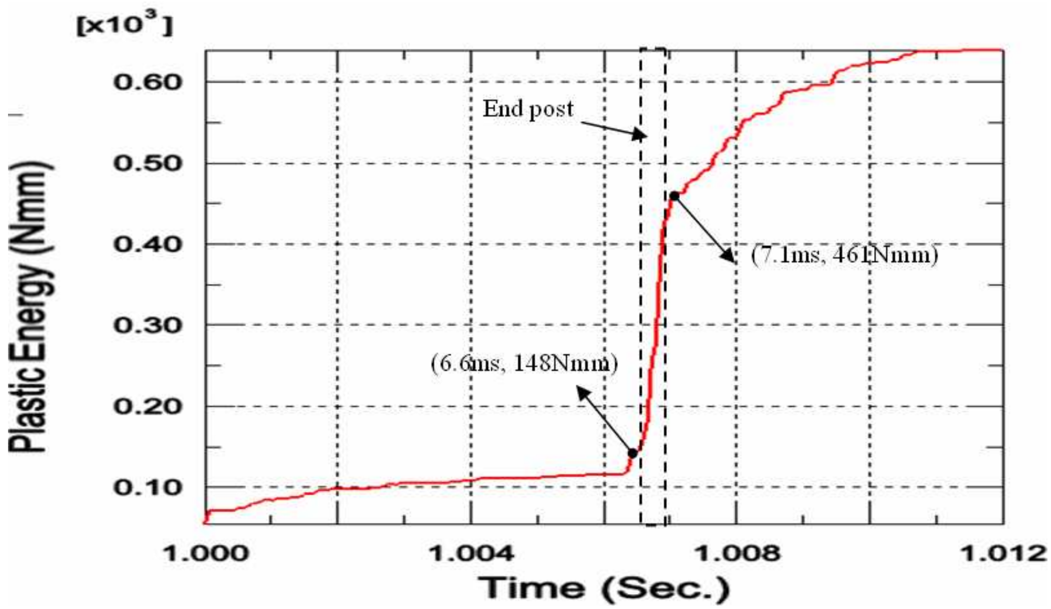

Figure 5.24 Plastic energy time series

Although the results presented so far illustrate the logical occurrence of impact in the vicinity of the end post, to further prove the appropriateness of the FE model for the contact-impact analysis, the end post material (nylon66) was replaced with the rail steel itself. This modification has effectively removed the joint (discontinuity), with the FE model of the IRJ becoming a rail with no joint; as such the model should predict no impact. The contact force time history shown in Fig. 5.25 proves that the FE model works well, as no impact is found with the contact force remaining at 150kN level (equivalent to static wheel load) throughout the travel and with the distinct absence of impact. The FE model is therefore regarded as being appropriate for the contact-impact study in this thesis. The model is further validated using some limited experimental data as explained in Chapters 6 and 7. The FE model is then used to examine the sensitivity of the design parameters of the IRJ with a view to determining a low impact (or, optimal) design of IRJ.

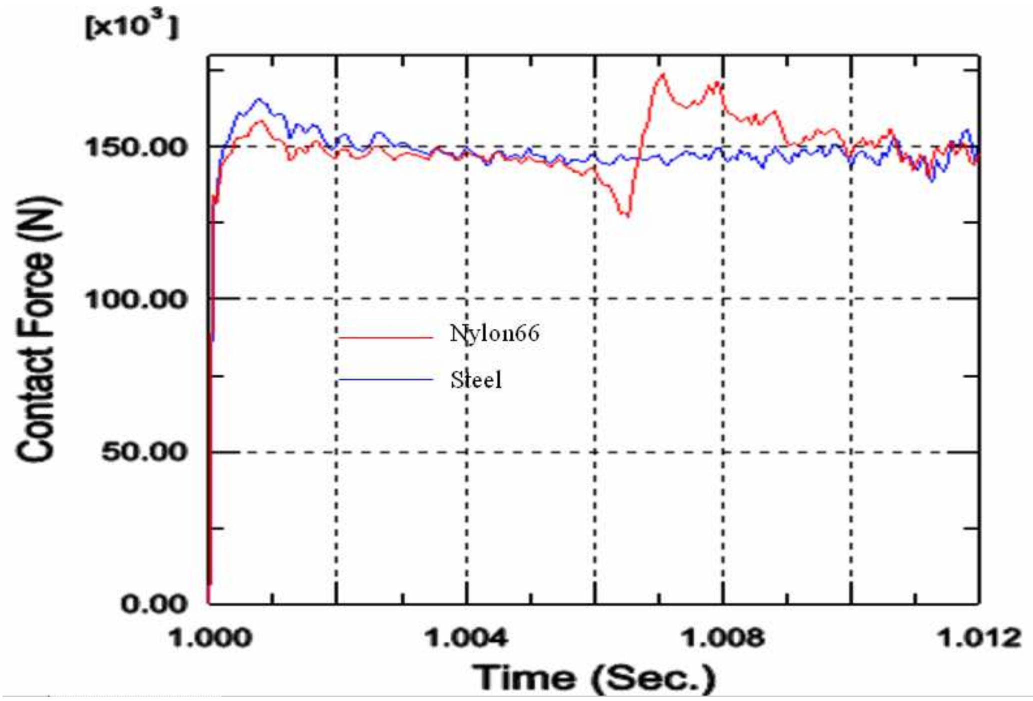

Figure 5.25 Contact force history of Nylon66 and Steel end post material

5.4. Sensitivity Analyses of Design Parameters of IRJ

There are a range of designs of IRJ available as discussed in Chapter 2. Sensitivity of a few major design parameters is reported. The basic design parameters examined are illustrated in Fig. 5.26; the sensitivity of these parameters to wheel/rail impact are reported in this section. The design parameters considered are:

(i.) End post bonding detail: glue or inserted

(ii.) Gap size: 5mm or 10mm

(iii.) Supporting system type: flexible or rigid (iv.) Length of joint bar: 4 bolts or 6 bolts long

(v.) End post material: Nylon66, Fibreglass or Polytetrafluoroethylene (PTFE).

(vi.) Joint suspended or directly supported on sleeper

In addition to the above, an operational parameter, namely sliding of wheels across the joint was also considered and compared to the rolling case. In all analyses, other than the sliding analysis, the wheel was considered as undergoing pure rolling.

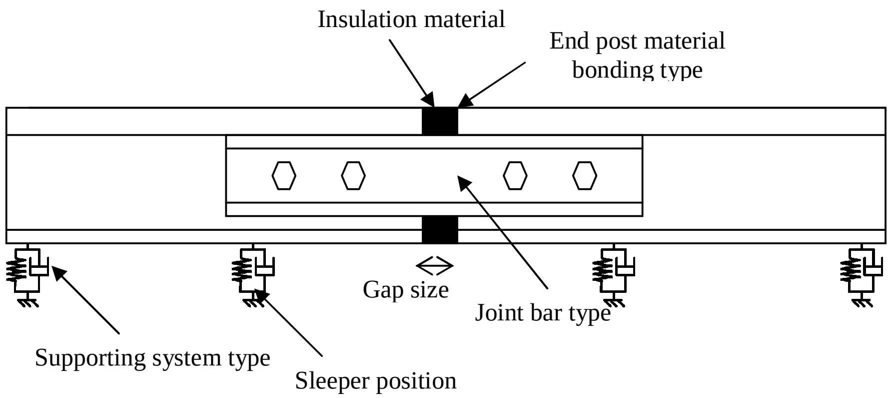

Figure 5.26 IRJ design parameters examined

5.4.1. Design cases considered

Each design case is uniquely identified by a combination of characters and/or numbers. The first character represents the end post bonding detail: **G** for glued and **I** for inserted (i.e. non-glue). The next two digits **05** or **10** represents the gap size 5mm or 10mm respectively. The fourth character, **F** or **R** is used for the flexible or rigid support at the base of the rail. The fifth and sixth characters stand for the length of joint bar, namely **4B** or **6B** standing for the 4-bolt joint bar or 6-bolt joint bar. The seventh character, **N**, **F** or **P** is used to specify the insulation material Nylon66, Fibreglass or PTFE respectively. The final three characters '**sus**'/ '**sup**' stand for whether the joint is suspended between sleepers or directly supported on the sleeper. The design parameter sensitivity was inferred by comparing the results from one or two design cases with Case (1) that served as a base case as shown in Table 5.4.

Table 5.4 Sensitivity study plan

Case Number	Sensitivity Studies	Explanation
(1)	**G10F4BNsus**	Base case
(2)	**I10F4BNsus**	Compare (2) to (1) for the determination of effectiveness of end post bonding detail
(3)	**G05F4BNsus**	Compare (3) to (1) for the determination of effectiveness of gap size
(4)	**G10R4BNsus**	Compare (4) to (1) for the determination of effectiveness of supporting system at rail base
(5)	**G10F6BNsus**	Compare (5) to (1) for the determination of effectiveness of length of joint bar
(6)	**G10F4BPsus**	Compare (6), (7) and (1) for the determination of effectiveness of type of end post material
(7)	**G10F4BFsus**	
(8)	**G10F4BNsup**	Compare (8) to (1) for the determination of effectiveness of suspended versus supported joint

5.4.2. Sensitivity studies

In this section, the sensitivity of design parameters is reported by comparing the design cases discussed above. The wheel/IRJ contact-impact force, which is the key cause of IRJ failure, is chosen as the basis for sensitivity study.

Two types of wheel motion, namely pure rolling and pure sliding, are investigated first. Locked wheels due to heavy braking/ traction tend to slide and are known as the primary reason for “wheel burn” type damage even on rails with no joints. The FE model developed was used to analyse the effect of sliding wheels near the IRJ on the contact force history. The IRJ containing a glued end post was used for this purpose.

Degree of freedom 5 of the wheel was arrested to simulate dragged wheels. The contact force history shown in Fig. 5.27 illustrates the increase in impact force (194kN – 174kN = 20kN for a static wheel load of 150kN representing 13% increase) that is significant. It is, therefore, important the operating vehicles ensure good rolling of wheels through application of gentle braking/ traction torques.

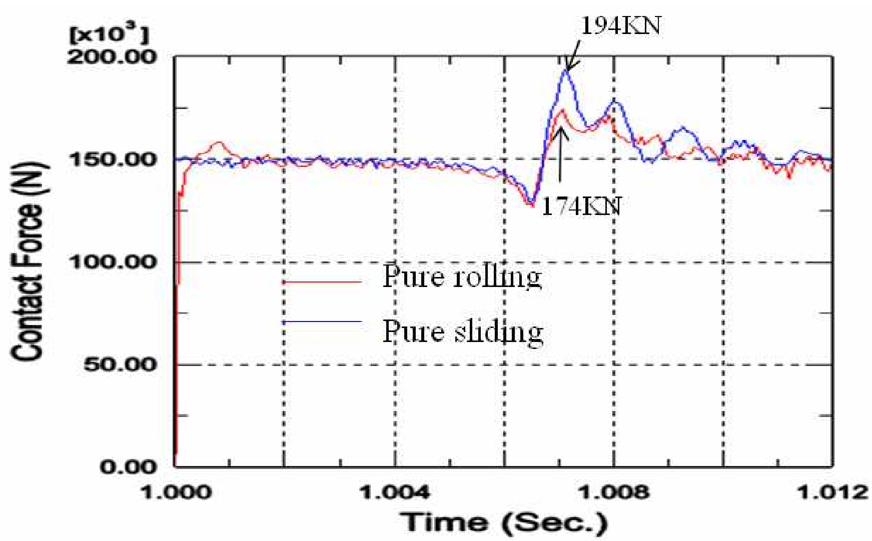

Figure 5.27 Contact force history of wheel pure rolling and pure sliding

(a) Effect of end post material bonding detail

Fig 5.28 shows the modelling of the glued and inserted end post.

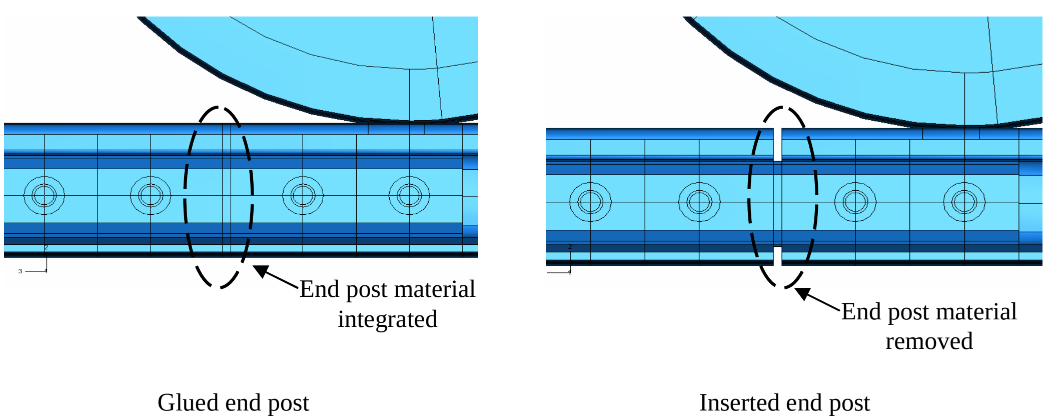

Figure 5.28 Modelling of end post material bonding detail

As the ‘inserted’ end post (non-glued) does not provide additional stiffness to the entire IRJ structure unlike the glued end post, it is generally expected that the ‘inserted’ type would generate higher impact. Modelling of the ‘inserted’ case of the end post is complex. To truly model this case, the end post surfaces and the rail end surfaces should all be initially defined as free. Progressively due to deformation, the model should account for the development of contact between these surfaces. For simplicity, the end post for the ‘inserted’ case was removed. Therefore it is expected that the model would predict high impact force as no benefit of partial support from the end post is accounted for in the model. The glued and inserted case modellings can therefore be regarded as lower and upper bound results.

Fig. 5.29 presents the contact-impact force histories of these two cases. The damage potential due to the increased impact of each wheel passage (185kN – 174kN = 11kN for a static wheel load of 150kN, or 8% increase) requires further investigation as the costs of gluing the end post against the potential increase in railhead damage requires economic justification. For the inserted (non-glued) case, the impact occurs 0.15ms later than for the glued case, corresponding to 48mm travel for the speed of 120Km/h. This suggests enlargement in the damage area of the IRJ.

(b) Effect of gap size

The gap size of conventional IRJ designs normally range from 5mm to 10mm. In this sensitivity study, two sizes of gap (thickness of end post material) of 5mm and 10mm have been considered. The FE modelling was simply realised by partitioning the end post zone for 5mm or 10mm, as shown in Fig. 5.30 for the two cases respectively.

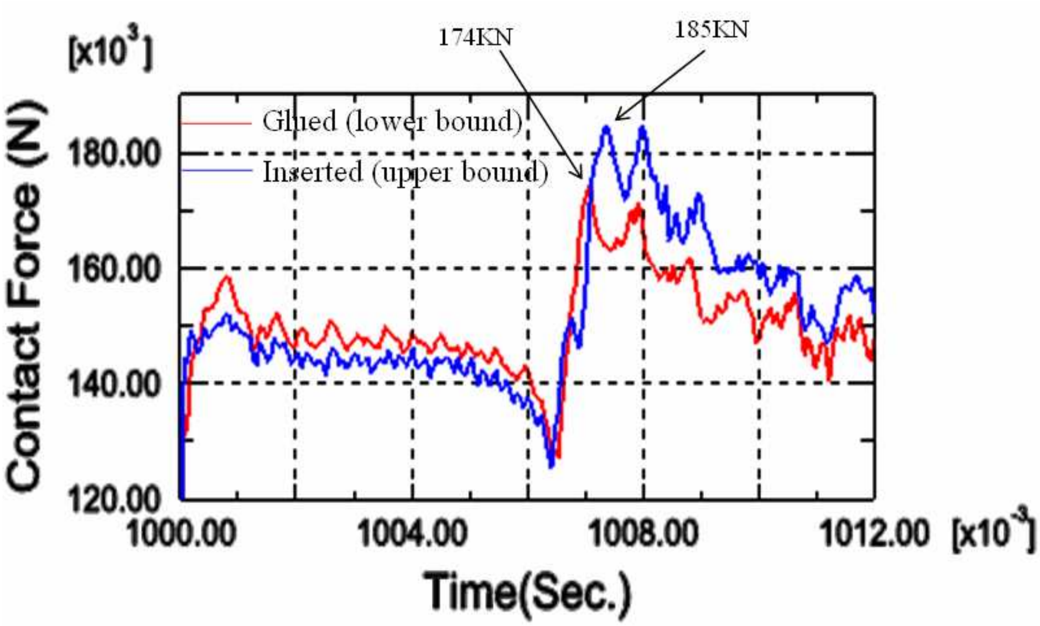

Figure 5.29 Contact force history of glued and inserted joint

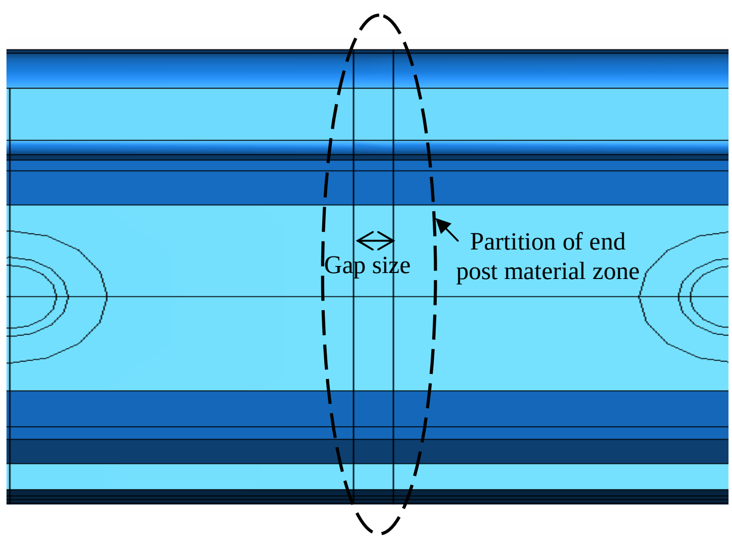

Figure 5.30 Modelling of gap size

The impact force time series for these two cases (cases (3) and (1)) are compared as shown in Fig. 5.31. The numerical result indicates that the small gap size reduces the impact force by 11KN (174KN-163KN) or 7.3% of the static load of 150KN. Further economic and technical assessment is required as the thinner gap may increase the possibility of early electrical isolation failure.

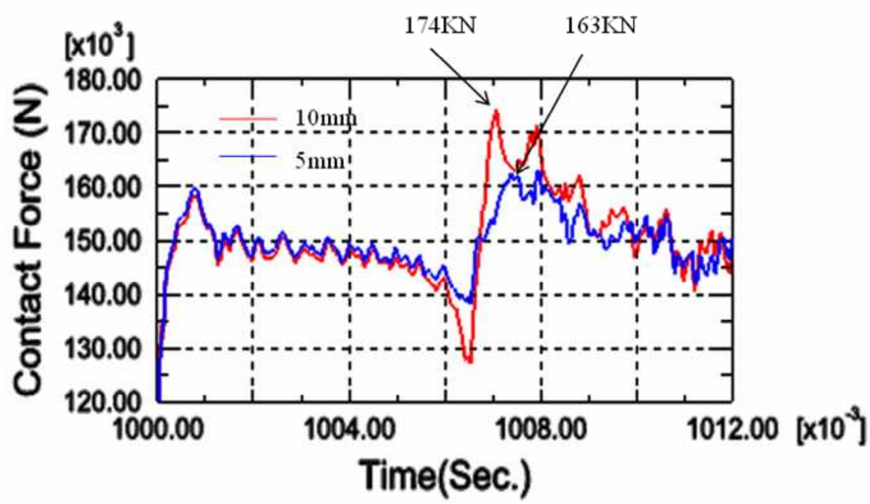

Figure 5.31 Contact force history of 10mm and 5mm gap size

(c) Effect of support condition

The modelling of the rail support foundation has been studied by many researchers. Models using discrete spring/dashpot sets representing the supporting system are commonly adopted for railway track studies. However, the constants of springs and dashpots are varied depending on different practical conditions and models. To examine the effect of the spring constant, the supports beneath the rail base were either considered as either flexible or rigid, which is an extreme case for rigid springs. The flexible supporting system has been already introduced in the previous chapter. The rigid case is realised by removing the spring/dashpot sets and directly fixing the rail bottom to the ground at the positions of sleepers.

The result illustrates that without the damping effect of flexible springs, the impact force can reach as high as 205KN with an increase of 21KN over the flexible case or 14% of the static load of 150KN. Fig. 5.32 also infers that without foundation damping the wheel/rail contact exhibits more vibration and is slower to stabilise after impact.

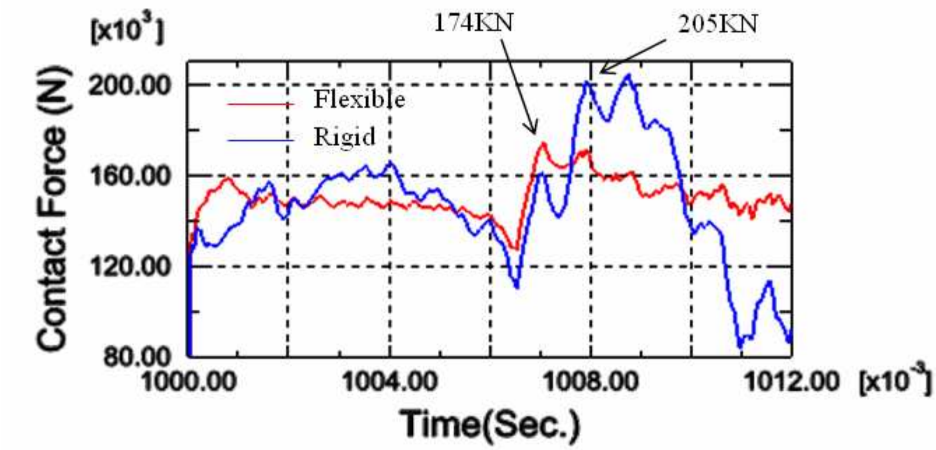

Figure 5.32 Contact force history of flexible and rigid support

(d)Effect of joint bar length (number of bolts)

Two types, namely 4 bolt long and 6 bolt long joint bars as shown in Fig. 5.33 have been considered. The cross sections of these two joint bars were kept the same and the longitudinal lengths were 576mm and 830mm respectively.

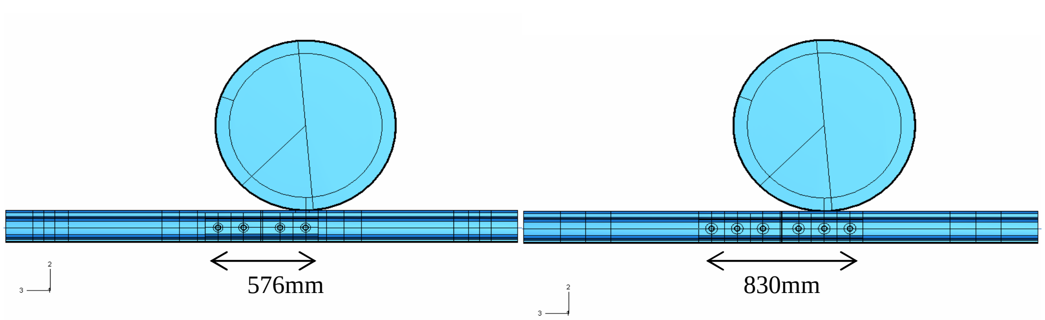

4-bolt joint bar model

6-bolt joint bar model

Figure 5.33 4-bolt and 6-bolt joint bar IRJ model

In this design case the 4-bolt joint bar is 254mm shorter than the 6-bolt joint bar in the longitudinal direction. As bolt pretension load is kept same, the four bolt joint bar has had lower pretension force in the lateral direction relative to the six bolt joint bar case. Fig. 5.34 illustrates that the 6-bolt joint bar IRJ generates a slightly larger impact force of 178KN compared to the 4-bolt joint bar case of 174KN. A conclusion can be drawn that the effect of the joint bar length and number of bolts on the impact force is not evident for reasons as explained below.

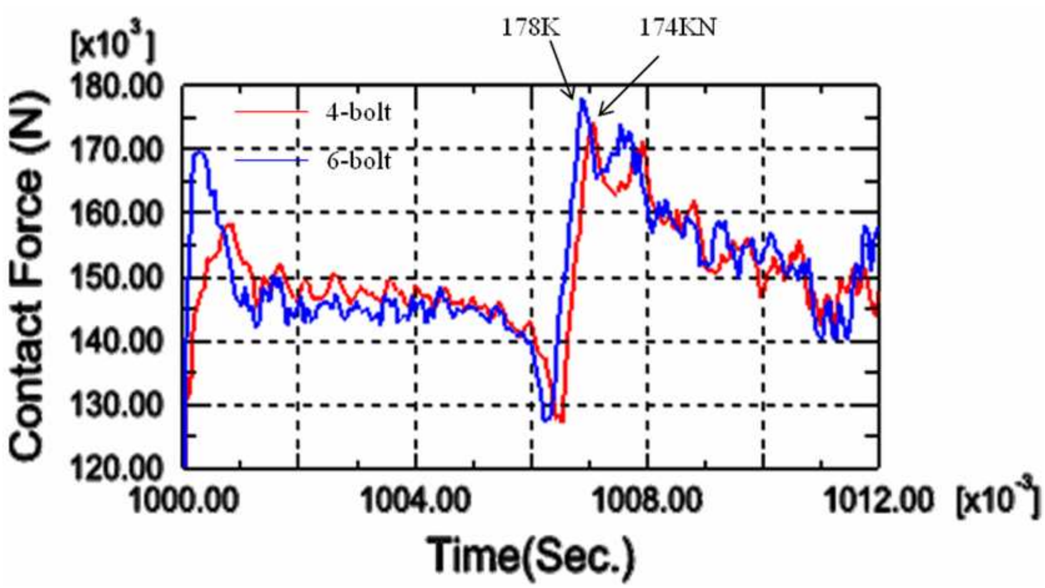

Figure 5.34 Contact force history of 4-bolt and 6-bolt joint bar

Considering the sleeper clear spacing is 564mm (Fig. 5.35), joint bars always span across sleepers whether 4-Bolts (576mm) or 6-Bolts (830mm) designs are used. Therefore their effect on impact is not significant in the cases considered. However, with 6-bolt joint bars, a larger sleeper spacing may be adopted. In the event of larger sleeper spacing, the 4-bolt case might generates larger impacts due to the larger dip (deflection) under wheel passage.

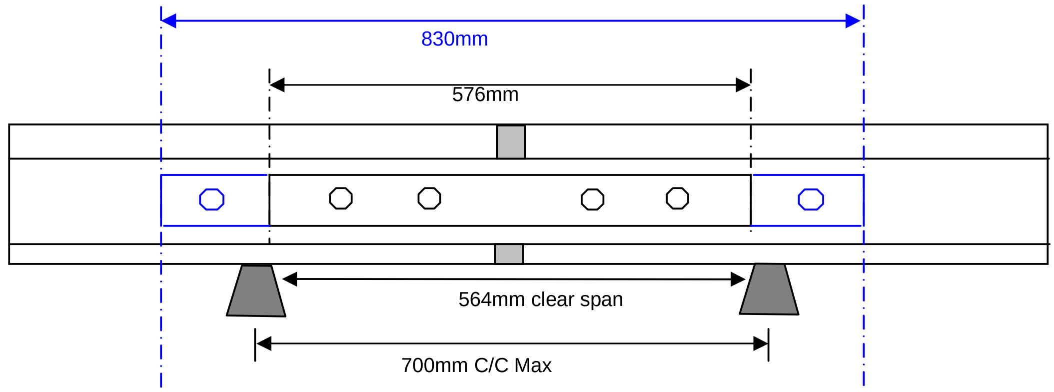

Figure 5.35 Illustration of sleeper spacing and joint bar length

(e) Effect of end post material

Three insulation materials have been investigated in this study: Nylon66, PTFE and Fibreglass (case 1, 6 and 7). Table 5.5 shows the Fibreglass is the stiffest material and the PTFE is the softest of the three materials. The result of the study is presented in Fig 5.36, which shows that the IRJ with fibreglass exhibits the lowest impact force level of 168KN while the other two cases both reach 174KN. Although the peak impact forces are the same for Nylon66 and PTFE cases, the PTFE case shows more post impact vibration during the wheel passages and the peak value has occurred 1.2ms later than the other two cases, corresponding to 40mm length. This would mean that the damage area may larger for PTFE. In contrast, the fibreglass case shows not only a lower impact force but also less post impact vibration.

Table 5.5 Mechanical properties of insulation material (Chen, 2002)

	PTFE	Nylon66	Fibreglass
Young's modulus E	400MPa	1590MPa	45000MPa
Poisson's ratio ν	0.46	0.39	0.19

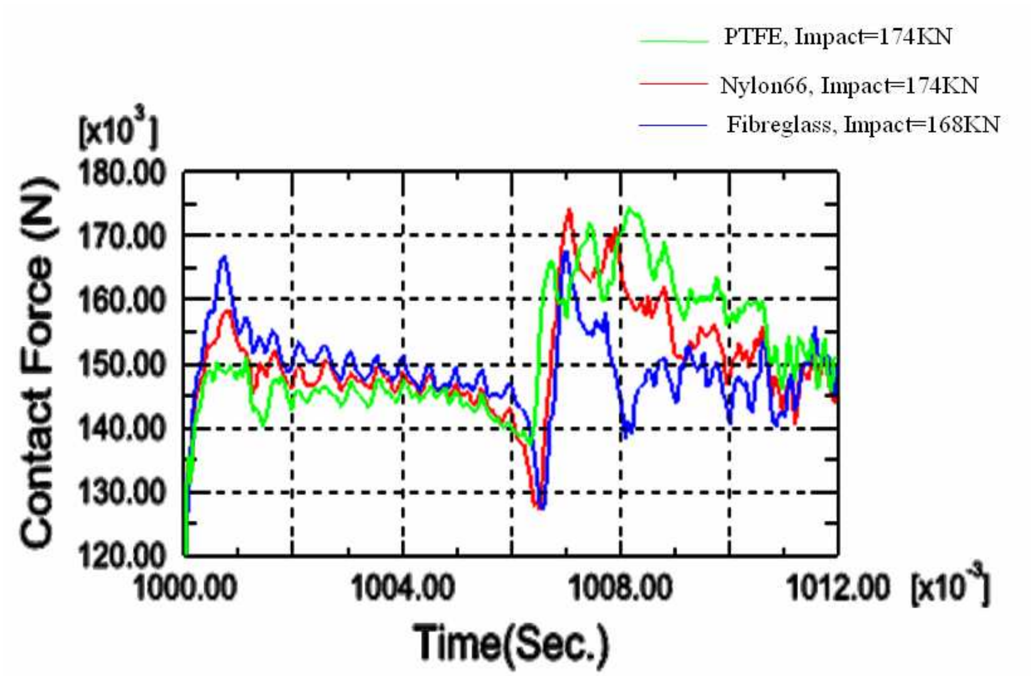

Figure 5.36 Contact force history of different end post material

(f) Effect of sleeper position

The sleeper position effects on the wheel/rail contact impact at the IRJ were studied by positioning the end post either symmetric to the sleepers (suspended IRJ) or directly on the sleeper (supported IRJ). Fig. 5.37 shows these two cases (case 1 and 8 respectively). The sleeper spacing was kept the same for both cases.

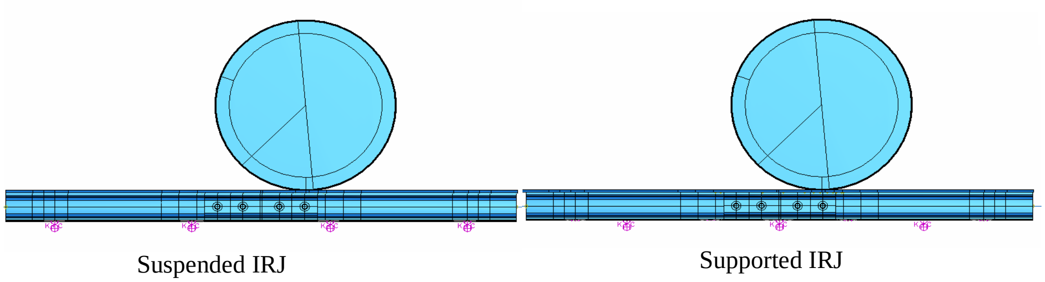

Figure 5.37 Position of sleepers

Fig. 5.38 shows that the supported IRJ has generated an impact force of 192KN, while the suspended IRJ has generated just 174KN impact force. The impact force difference is almost 12% of the static load of 150KN. The supported IRJ also exhibited significant post impact vibration. A similar response was also exhibited for the case of rigid support (Fig. 5.32). This shows that when either the support is stiffer or the IRJ is directly supported, the waves generated due to impact reflect more strongly resulting in the post vibration effect lasting longer.

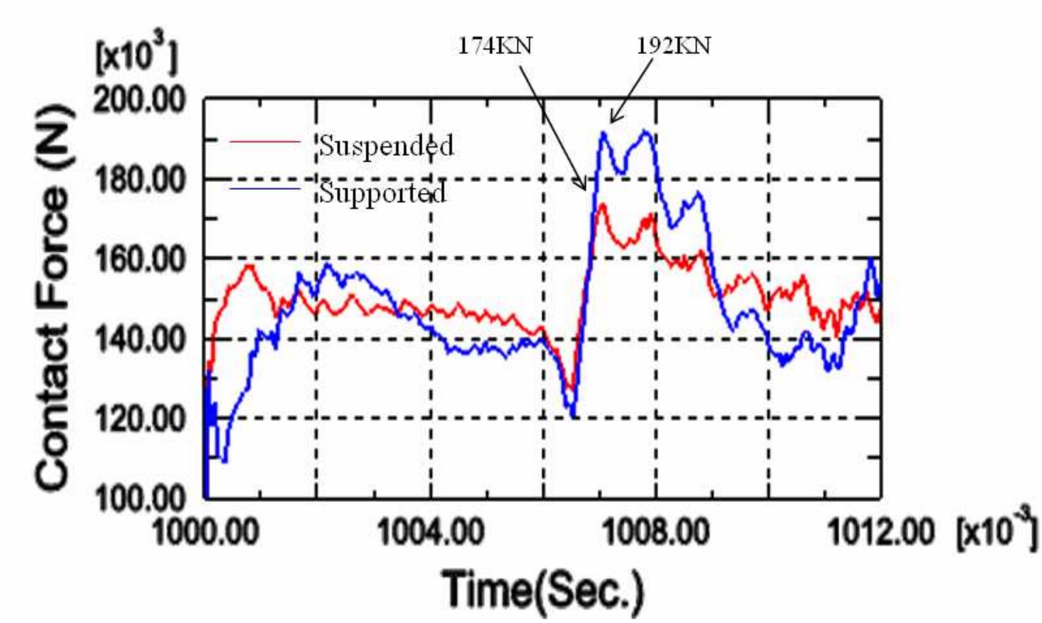

Figure 5.38 Contact force history of IRJs suspended or supported

5.4.3. Discussion of sensitivity study results

Through the analyses of these eight design cases, the effects of the selected design parameters on the wheel/rail contact-impact forces are investigated and a few conclusions are drawn.

- The glued IRJ performs better than the inserted (non-glued) IRJ. The IRJ with a smaller gap size generates less impact.
- The higher the flexibility of the supporting system, the lower the wheel/rail contact-impact.
- The effects of joint bar length seem to not be significant to the wheel/rail impact force based on the numerical results. Both the 4-bolt joint bar and the 6-bolt joint bar have just enough length to span across the clear spacing of the sleepers. Should the sleeper spacing be larger than the 4 bolt joint bar length, the result would have been different.
- The stiffer the end post material (fibreglass in this case), the lower the impact forces. This is because the material with mechanical properties closer to steel decreases the discontinuity in stiffness in the vicinity of the end post.
- It seems not a good choice to place a sleeper directly underneath the IRJ end post. The directly supported IRJ generates much larger impact forces relative to the suspended IRJ.

In summary, to minimise the wheel/rail contact impact force at the IRJ, the best design parameter combination is a fibreglass end post with 5mm gap size that is glued to the rail sections suspended between the flexible supporting system (**G05F4BFsus**). Fig. 5.39 indicates that the impact force is largely eliminated in this case. From a practical perspective, this case may be considered technically optimal.

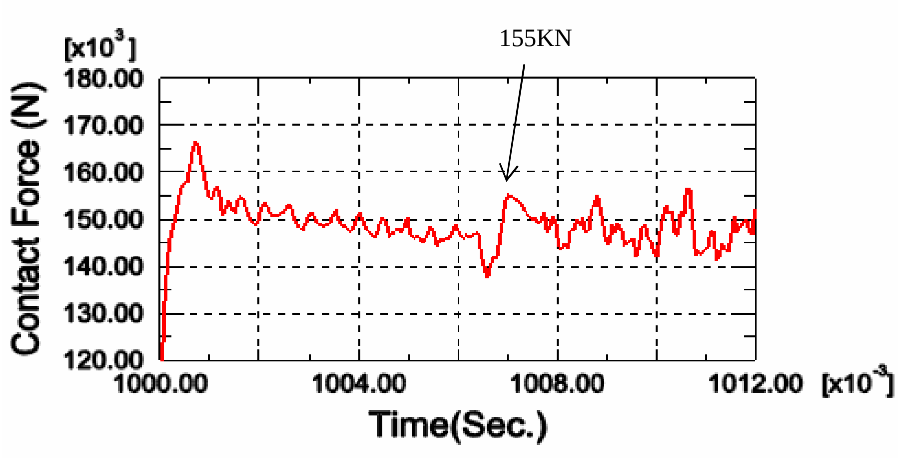

Figure 5.39 Contact force history for case **G05F4BFsus**

5.5. Summary

The wheel/rail contact impact at IRJs has been studied and reported in this chapter. The wheel/rail contact force history indicates that the impact is generated due to a ‘two-point contact’ as the wheel passes over the joint due to a flexible deformation of the joints in the vicinity of the end post. This flexibility causes an early reduction in the contact force below the static wheel load. At the time of impact, the wheel lands on the end of the rail on the other side of the joint, with the impacting point several millimetres away from the rail end and whilst the first rail end is still in contact with the wheel. It is notable that the structural deformation of IRJs during the impact is recoverable, although some plastic deformation may have occurred at the rail head. The impact mechanism can be explained as one caused by the IRJ stiffness discontinuity leading to the temporary geometry discontinuity under wheel passages as:

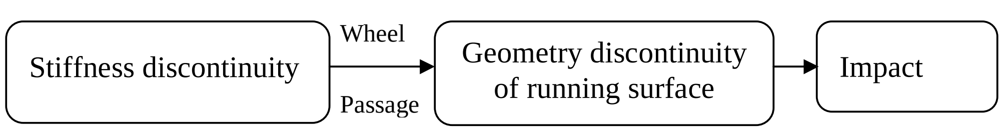

It has been shown that the contact pressure distribution, in particular the contact patch dimensions and the contact area, are significantly affected by the mesh size. Due to the limitation of the computational facility, the mesh was made coarse. It was found that, in the dynamic analysis although the contact area was consistently larger than HCT, the peak contact pressure was not affected indicating mesh changes to the distribution of pressure within the contact patch.

The HCT is proved valid as long as the wheel/rail contact area remains away from the joint. Dynamic results indicate that the Hertz contact theory is not strictly valid due to edge effect and material plasticity during the occurrence of impact.

6. Strain Gauged IRJ Experiments

6.1. Introduction

To validate the FE model presented in Chapter 4, this thesis has taken advantage of a major field experimental program carried out jointly by the Centre for Railway Engineering (CRE) and Queensland Rail (QR). This experiment involves laboratory tests and field tests. In this chapter, the design of the experiment is presented first in section 6.2. The strain gauge positioning strategy is reported in section 6.3. The manufacturing process of the strain gauged IRJ is introduced in section 6.4. The setup details of lab test and field test are presented in sections 6.5 and 6.6 respectively. Analysis of typical test data is presented in section 6.7 followed by the summary of the chapter in section 6.8.

6.2. Strain-Gauged IRJ Experimental Strategy

The experimental program contained two parts: lab test and field test. The main purpose of the lab test was to ensure the strain gauges were properly working prior to installing in the field. The lab test was conducted in the Heavy Testing Laboratory (HTL) and the field test was carried out in the live railway track. The lab test involved six loading positions as shown in Fig. 6.1 (0mm, 20mm, 50mm, 100mm, 150mm and 200mm from IRJ centre). A static load of 150KN was applied to the railhead and the IRJ was simply supported at the two ends 300mm away from the IRJ centre (end post) as shown in Fig 6.1.

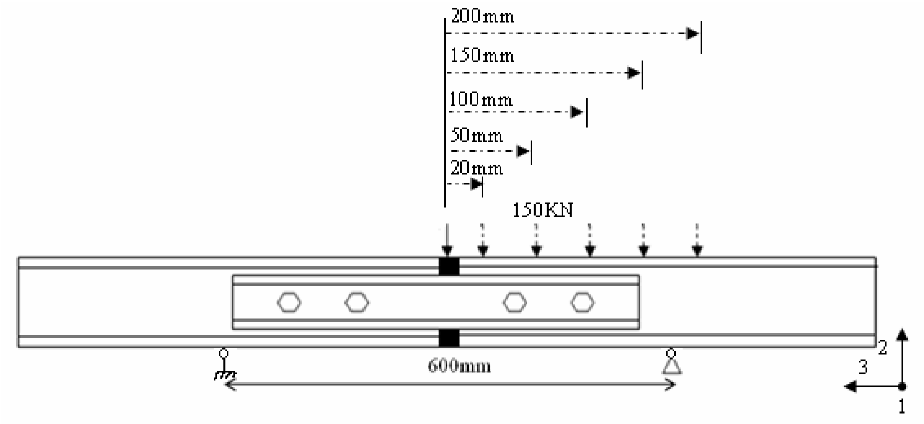

Figure 6.1 Loading positions in lab test

In the field test, the wheel/rail contact impact at the IRJ was indirectly inferred from the strain time series under wheel passages. Referring to Fig. 6.2, the passing wheel triggers the solar powered data recording system using an ultrasonic sensor. The signals from strain gauges were amplified and recorded using the National Instruments DAQ card. The DAQ scanning frequency was set as 20 kHz, sufficient to capture the high frequency dynamic responses. The data recording only occurred for 10 seconds (200,000 data points) with a view to minimising the size of data files. Each passing train triggered collection of the data that were stored in separate files. After each recording, the ultrasonic sensor remained off line for two minutes and started scanning for the next passing wheels.

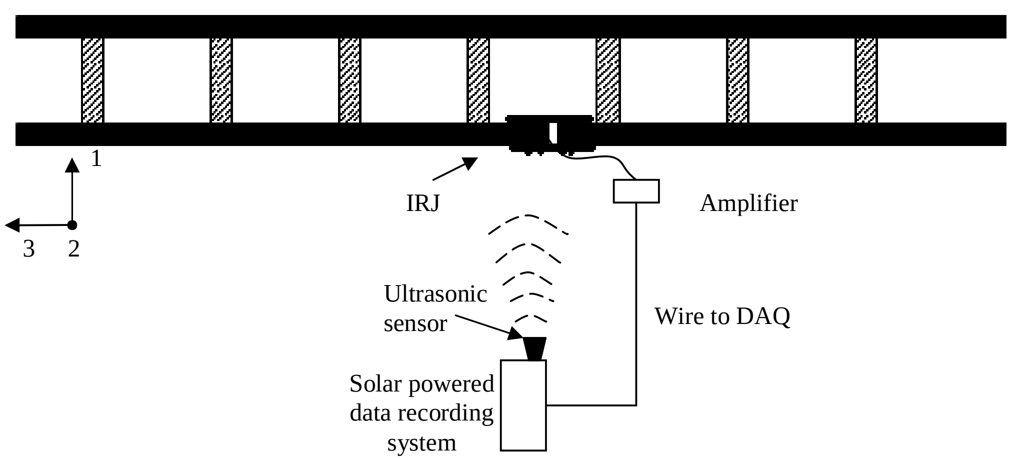

Figure 6.2 Data recording system for the field test

6.3. Strain Gauge Positioning Strategy

Positioning of the strain gauges is critical to the successful outcome of this experiment. As a principle, the locations for strain gauges should be fairly sensitive to the high magnitude strains under static and dynamic loads whilst being technically feasible. To acquire the IRJ impact response that is of interest, the strain gauges are also required to be as close as possible to the end post and railhead. Strain gauges can only be placed on the surfaces of IRJ parts; the top of the railhead surface is automatically excluded because of the wheel passage; the rail ends are also excluded as it would be difficult to detail the strain gauge wires and strain gauges in a safe manner. As a result, the rail web, the rail bottom and the joint bars are possible locations. Numerical results from the dynamic FE model are employed to identify the most sensitive positions for locating the strain gauges.

Determining the rail strain is a complex problem. This is because rail is constantly subjected to thermal strain and under the action of wheel loads; it is subjected to bending and shear stresses. Therefore three surface strains (two normal and one shear) on two mutually perpendicular planes would establish six independent strain components. As two of the out of plane shear strains (E_{12} & E_{13}) and lateral normal strain E_{11} are of less significance in tangent track rails (without regard to braking/traction forces), only three strain components that are sensitive to the wheel/rail normal contact (the vertical normal strain E_{22}, the shear strain E_{23} and longitudinal normal strain E_{33}) have been measured. The FE results indicate that the rail web is sensitive to the E_{22} and the E_{23} while the rail bottom is more sensitive to the E_{33}. The joint bars are not sensitive to any of the important strain components.

The snap shots of the vertical strain distribution from the dynamic analysis corresponding to three wheel positions (15mm before end post, at end post and 15mm after end post) are shown in Fig. 6.3 (a), (b) and (c) respectively. Before the wheel hitting the end post, the maximum strain value is shown as 430 μs located at the fillet radii between the railhead and the web, 110mm above rail bottom. For the wheel loading at 0mm and 15mm after the end post, the maximum strains are 660 μs and 620 μs respectively. These strain values are sufficiently large for reasonable measurement accuracy by electrical strain gauges.

Hence, there are four symmetric points (1, 2, 3&4) on both sides of rail web at both rails selected for gauging the vertical normal strain E_{22} and shear strain E_{23} shown in Fig. 6.4. The longitudinal normal strain on the rail web, although captured by these strain gauge rosettes, remain very small throughout the wheel travel in the vicinity of the end post.

For the longitudinal strain E_{33}, the most sensitive and practical position is the rail bottom. Referring to Fig. 6.5, with the wheel load at the IRJ centre, the maximum longitudinal bending strain is around 64.2 μs. The contour demonstrates a symmetric distribution of E_{33} at the bottom of both rail ends. E_{33} is concentrated at the positions approximately 60mm away from the joint. Hence the strain gauges (Strain gauge 5 & 6) are symmetrically positioned to measure the E_{33} as shown in Fig. 6.6.

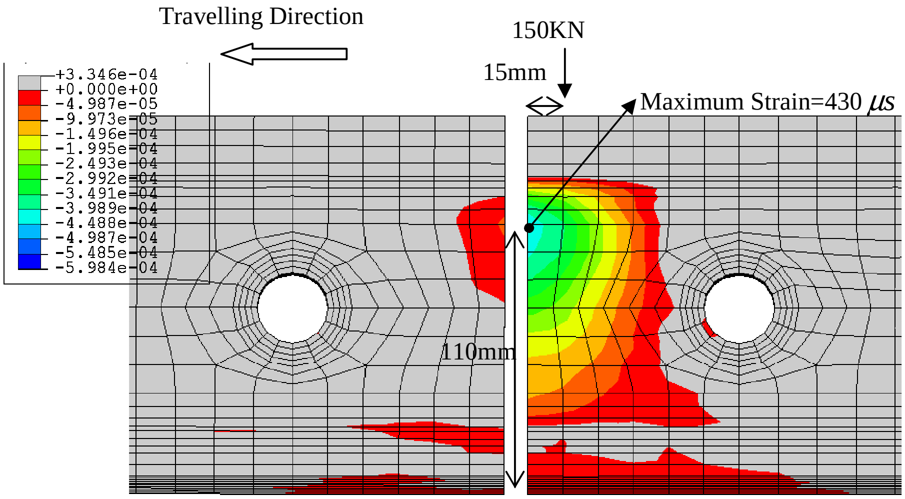

(a) Pre impact

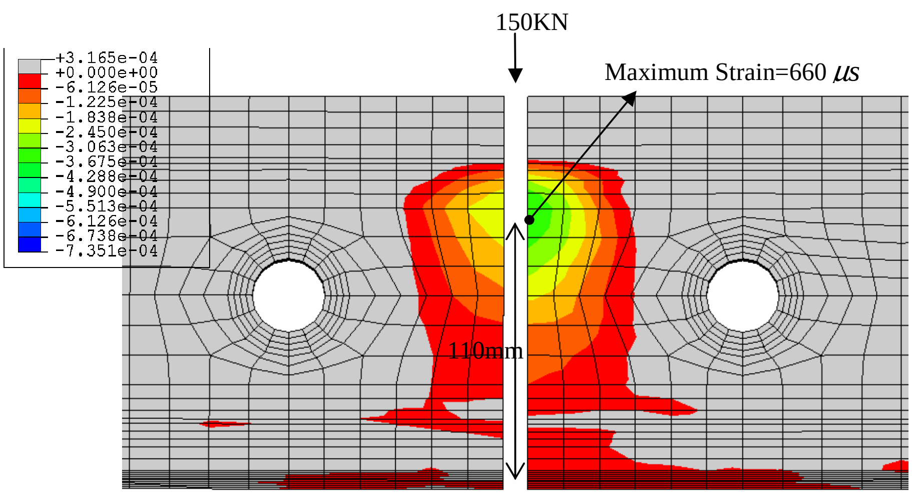

(b) At impact

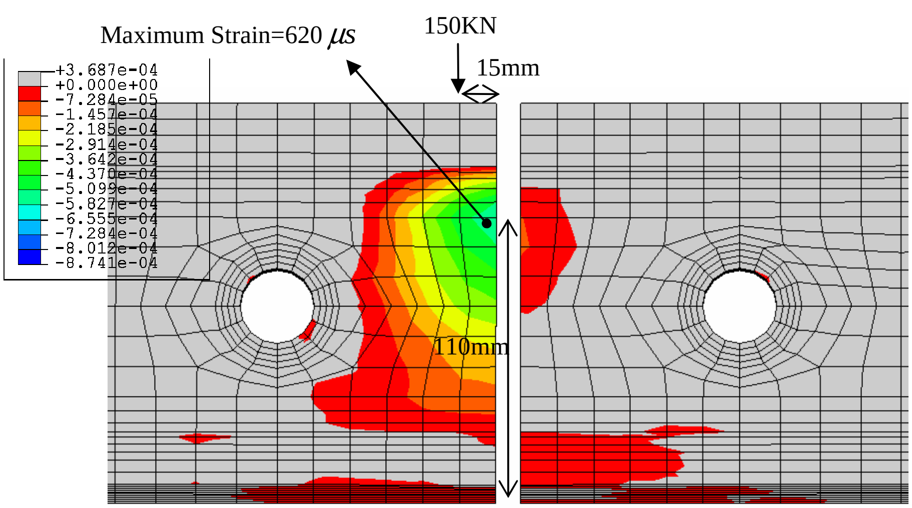

(c) Post impact

Figure 6.3 Snap shots of the vertical strain distribution from the dynamic analysis

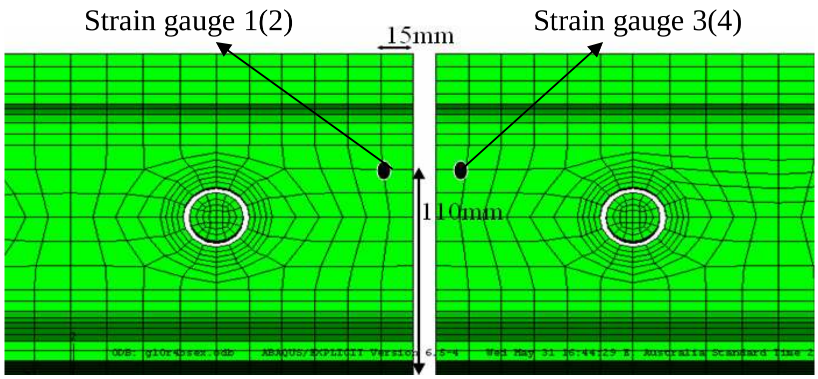

(a) Longitudinal view

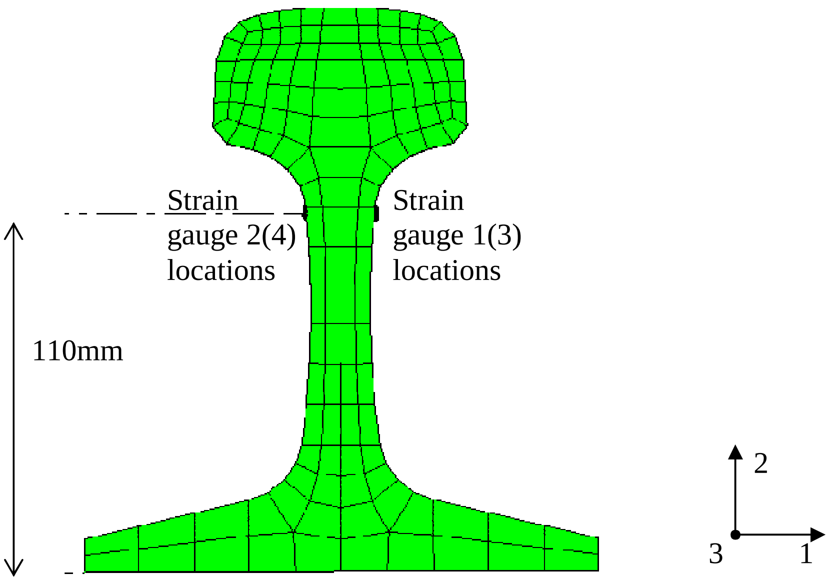

(b) End view

Figure 6.4 Strain gauge positions for E_{22} and E_{23} measurements

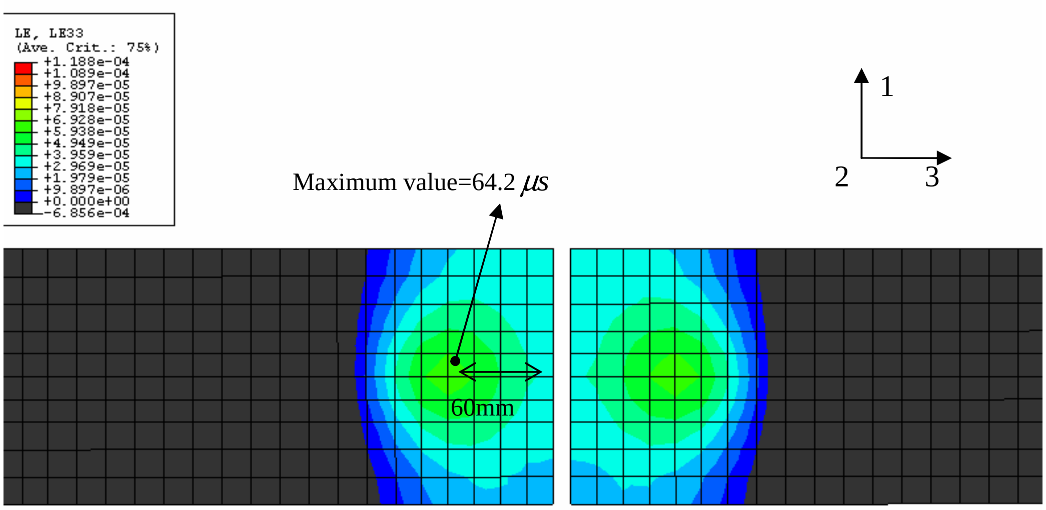

Figure 6.5 E_{33} distribution on the rail bottom

In summary, there are six positions on two both rail sections (four on rail web and two on rail bottom) of IRJ selected for strain gauging. Strain gauges 1, 2, 3 and 4 on the rail web surface are used for E_{22} and E_{23} measurement and Strain Gauges 5 and 6 on the bottom are selected to measure the E_{33}.

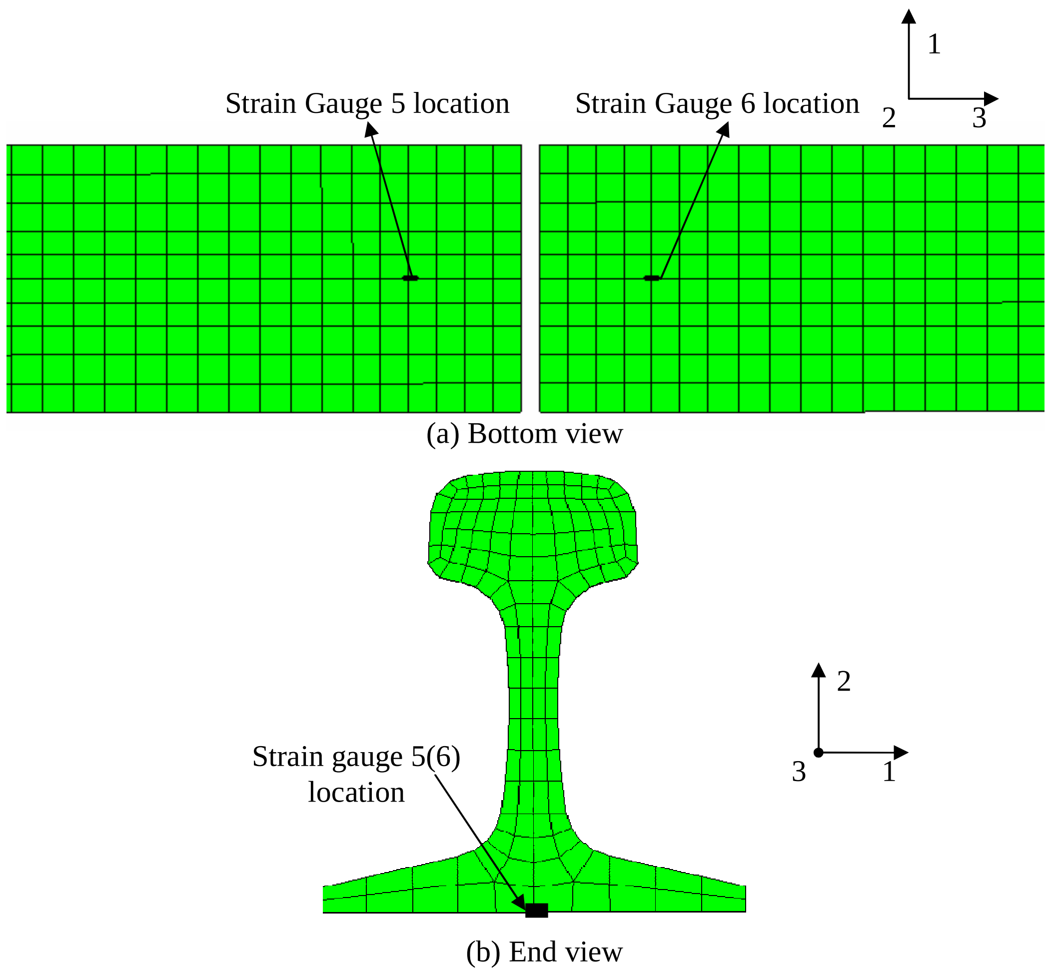

Figure 6.6 Strain gauge positions for E_{33} measurements

6.4. Preparation of Strain Gauged IRJ

6.4.1. Selection of strain gauge rosette

The 45˚ 3-gauge rosette selected for the measurement of the vertical normal strain E_{22} and shear strain E_{23} is shown in Fig. 6.7. The middle gauge B is aligned in the vertical direction for the E_{22} measurement, and the E_{23} is calculated from the two 45˚ aligned gauges A and C. A linear gauge D is used at the rail bottom surface for the E_{33} measurement. Eq. (6.1) was used to convert the measured linear strains to the normal and shear strain:

$$\begin{aligned} E_{22} &= E_{BB} \\ E_{23} &= E_{CC} - E_{AA} \\ E_{33} &= E_{DD} \end{aligned} \tag{6.1}$$

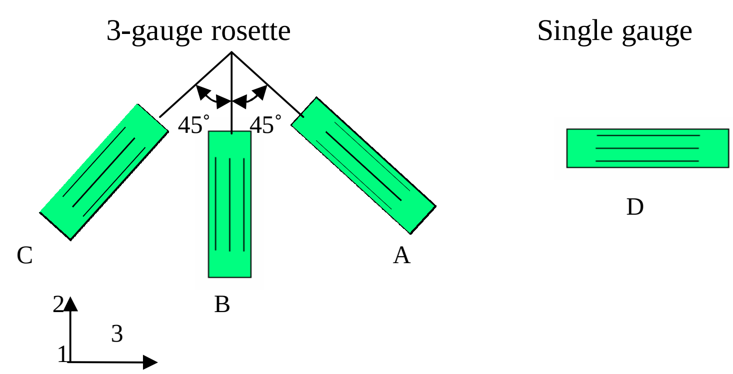

Figure 6.7 Strain gauge rosettes

To withstand the high temperature involved in the IRJ assembling process, Vishay Micro-Measurement CEA gauges with a fully encapsulated grid and exposed copper-coated integral solder tabs were selected. This strain gauge had a wider working temperature range from (-50˚C) to (+250˚C).

6.4.2. Installation of strain gauges on IRJ

The strain gauges were positioned at the rail web and the rail bottom. Installation of the rail web strain gauges was comparatively more complex as they were positioned on the rail web covered by the joint bar. The rail bottom strain gauges were stuck on the exposed rail bottom surface after the IRJ was fabricated in the factory.

The rail web strain gauges were installed during the process of assembling of the IRJ in the factory. First the strain gauges were stuck on both sides of the rails (Fig 6.8). The rail bottom strain gauges were stuck on after the IRJ was assembled in the factory, and covered with a plastic layer of water proofing material.

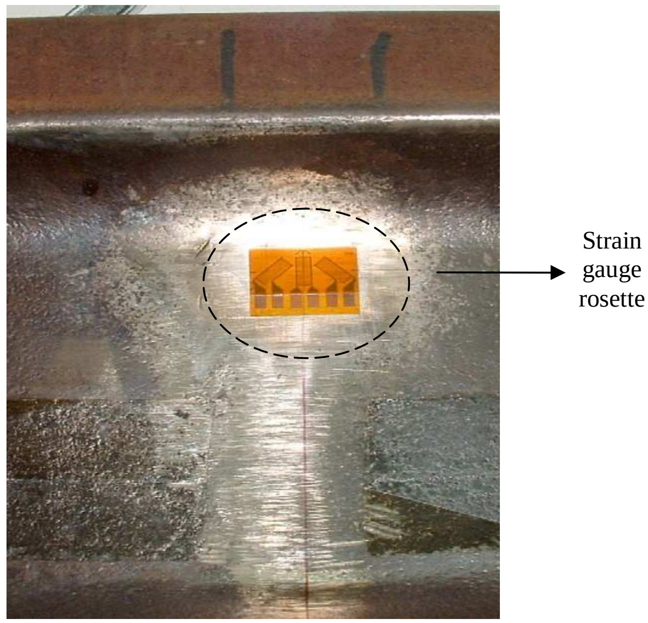

Fig 6.8 Strain gauges stuck to the rails

6.5. Lab Test of Strain Gauged IRJ

In this section, details of IRJ laboratory test setup are presented. Some typical test data are also reported; the data were used to validate the FE model as described in the next chapter.

6.5.1. Laboratory test setup

The overall IRJ test setup in the laboratory is displayed in Fig. 6.9. The IRJ was supported on two steel bars in such a way that the rail bottom surface contacted with the bar top surface. The smooth contact surfaces between the rail bottom and the steel bars allowed the IRJ to move freely in the longitudinal direction. The span of the IRJ was kept as 600mm. The static load driven by the actuator was transferred to the railhead through a steel block. The steel block was provided with the railhead profile to ensure a conforming contact. The actuator was driven by a hydraulic pump and the loading rate was controlled as 1kN/s to satisfy the static loading hypothesis. Fig 6.10 shows how the load was transferred from the actuator to the railhead.

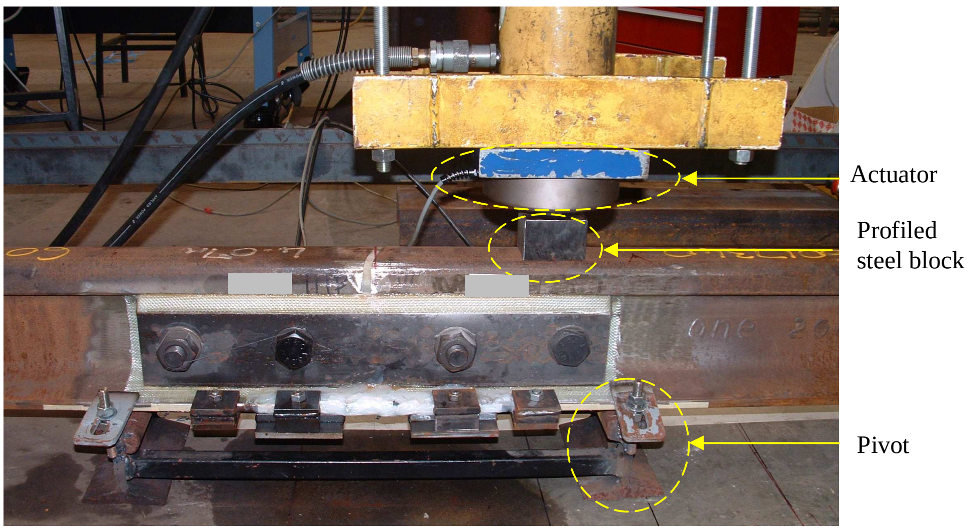

Figure 6.9 Lab test setup

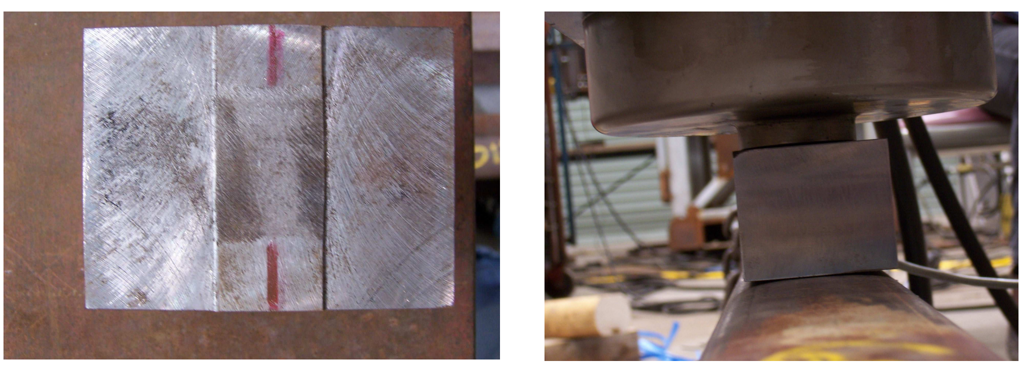

(a) Loading block (b) Load transfer to railhead

Fig 6.10 Loading equipments

The strain gauge response signal was acquired by four 4-channel National Instruments DAQ cards. In this lab test, all fourteen strain gauge channels were connected to the

DAQ card for data collection. The Quarter-Bridge type was employed for the strain gauge circuit (Fig 6.11), where the $R1 = R2 = 500\Omega, R3 = 350\Omega$ are resistors, $Rl = 2.76\Omega$ is the wire resistance and strain gauge resistance $Rg = 350\Omega$. $Vex = 5V$ is the bridge excitation voltage and Vo is the calibrated bridge output voltage. The strain is calculated from the voltage as:

$$\varepsilon = -4Vr * (1 + Rl / Rg) / [GF * (1 + 2Vr)] \tag{6.2}$$

Where $Vr = (Vo / Vex)$ and gauge factor GF is 2.11 in this case.

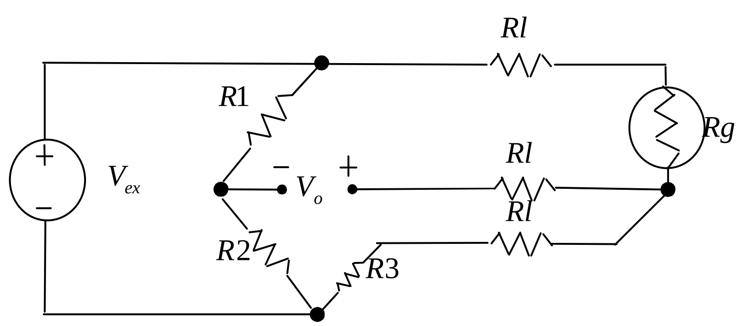

Fig 6.11 Quarter-bridge routine for strain gauges

6.5.2. Typical data

The data collected from the strain gauges were converted to the objective strain components: vertical normal strain E_{22}, shear strain E_{23} and longitudinal strain E_{33} using Eqs. (6.1) and (6.2). Strain gauges 1, 2, 3 and 4 were used for E_{22} and E_{23} measurement and strain gauges 5 and 6 on the rail bottom were used for E_{33}.

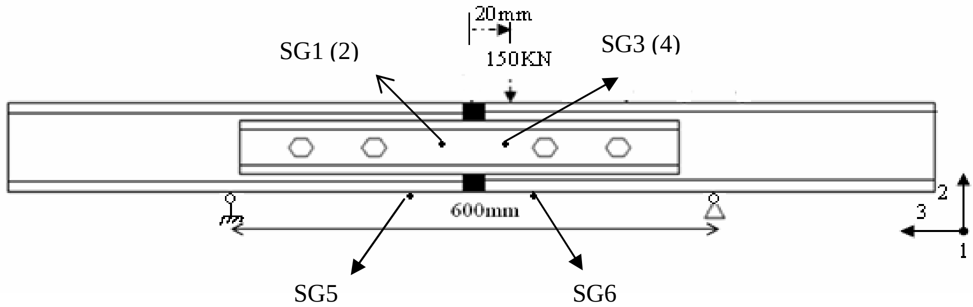

Fig 6.12 Illustration for position of strain gauges and load

It was extremely difficult to ensure the symmetry of loading (see Fig. 6.10); some eccentricity was unavoidable. Therefore it was found that the strain data collected from Strain Gauges 1 and 2 and Strain Gauges 3 and 4 varied. To ensure linearity and repeatability checks, it was considered sufficient to average the corresponding strains to both sides of the rail web. Fig. 6.12 shows that the loading position is 20mm away from the IRJ end post centre. Fig. 6.13 and 6.14 indicate that under the 150KN static load, E_{22} from Strain Gauges 1/2 is 35.6 microstrain and 464.7 μs for Strain Gauges 3/4. The shear strain E_{23} for the Strain Gauge 1/2 is 47.1 μs while Gauges 3/4 show a value of 234.5 μs. The longitudinal tensile strain is plotted in Fig. 6.15. It indicates that Strain Gauges 5 and 6 have had a very similar magnitude of 118.2 μs and 123.1 μs respectively.

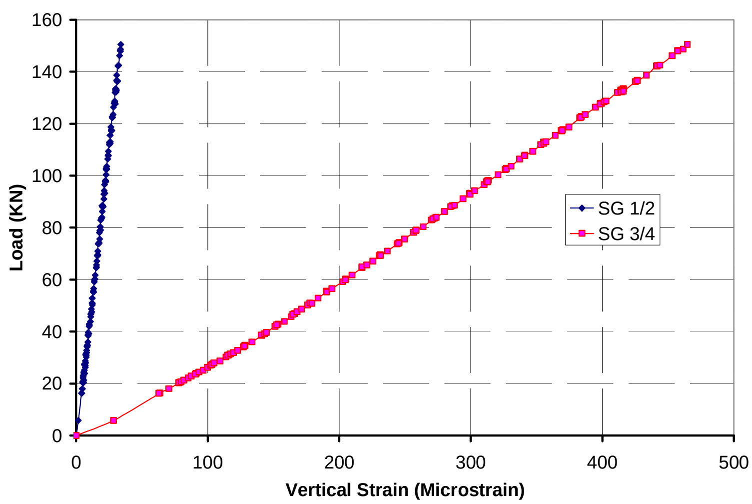

Figure 6.13 Averaged vertical strain E_{22}

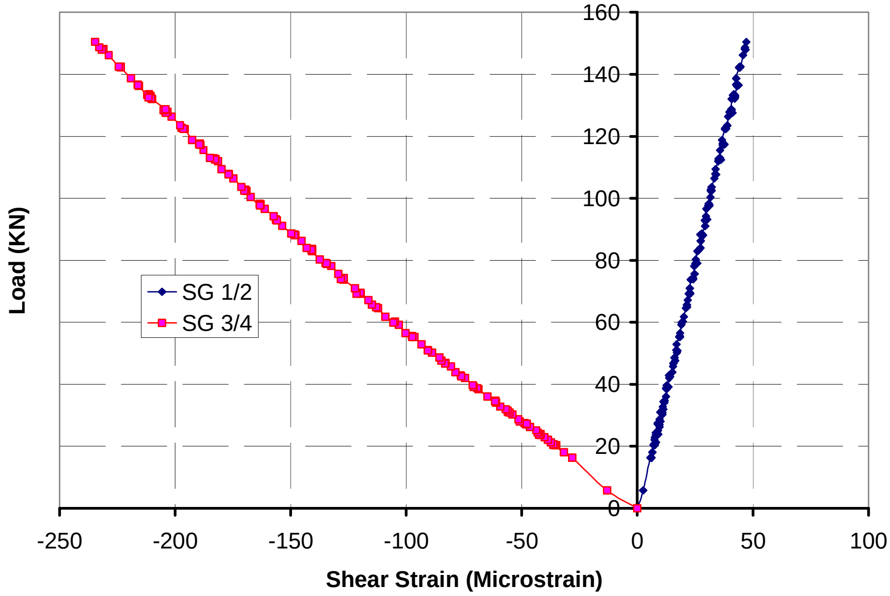

Figure 6.14 Averaged shear strain E_{23}

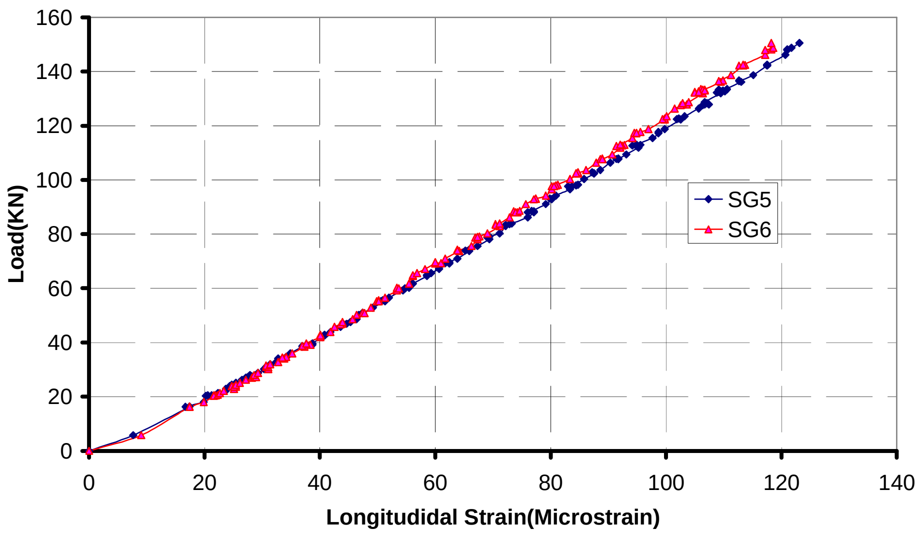

Fig 6.15 Longitudinal strain E_{33}

6.6. Field Test of the Strain Gauged IRJ

In this section, the details of IRJ field test setup are presented and the typical test data are also reported.

6.6.1. Field installation

The strain gauged IRJ was installed in the field by replacing a continuous weld rail section (Fig. 6.16). A data recording housing was built near the track for automatic wheel passage detection and data recording.

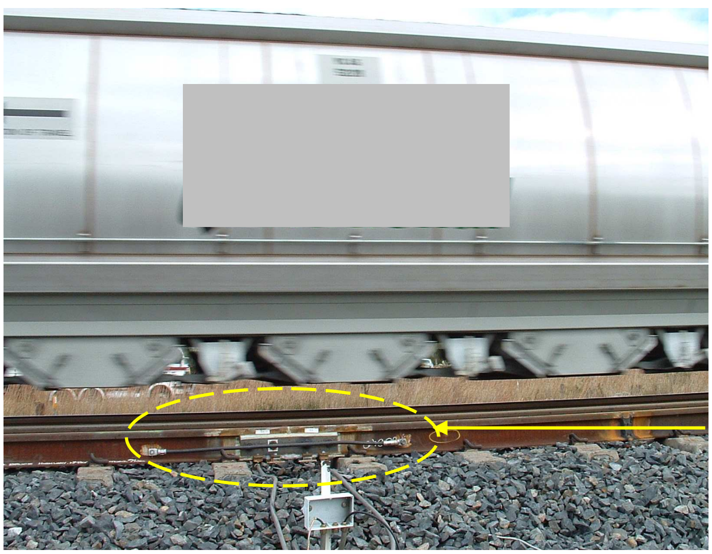

Figure 6.16 Installed strain gauged IRJ as a wagon is passing over

The wires from strain gauges were connected to an amplifier used to amplify the voltage signals to improve the signal reception. The signals from the amplifier were transferred to the data recording system. A solar powered data recording system consisted of a National Instruments compact DAQ and Logger, ultrasonic sensor, solar panels (2 x 80W), charger and storage hard disk.

The strain gauge circuit used in the field test was the same as that of the lab test. Due to the limited number of DAQ channels, the strain gauges on only one rail of the strain gauged (Strain gauge 1, 2 and 5) IRJ were activated. The DAQ channel scanning frequency was kept as 20 kHz and the recording duration for each passing train was limited to 10s, which corresponded to 200,000 data points from each channel for each train. A data processing programming was coded in MATLAB.

6.6.2. Typical data

In this field test, Strain gauges 1 and 2 were used for monitoring E_{22} and E_{23} and Strain gauge 5 was used for measurement of E_{33} . The converted strain components E_{22} , E_{23} and E_{33} are presented in Fig. 6.17, Fig 6.18 and Fig. 6.19 respectively.

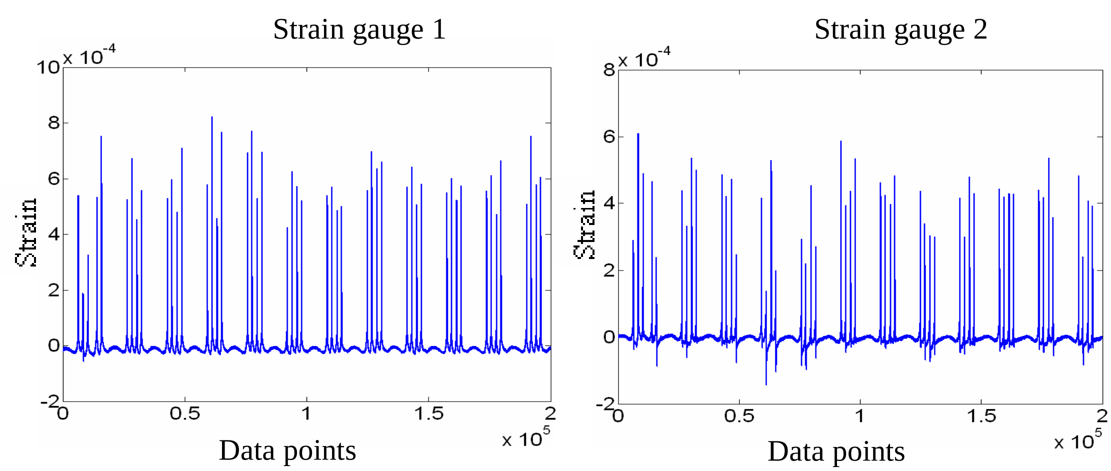

Figure 6.17 Vertical normal strain E_{22} history

It can be seen there are many ‘impacts’ in each file and each ‘impact’ represents a passing wheel. The horizontal axis is the recorded data point number (which can be converted to time divided by 20,000) and the vertical axis is the strain magnitude. The recorded peak value of E_{22} and E_{23} are in the order of 10^2 μs while E_{33} has a lower value at the order of 10^1 μs. The strain time series of E_{33} exhibits quite noisy signals due perhaps to the strain gauges being located away from impact locations. Furthermore, longitudinal strains are affected by flexure due to other wheels as well as thermal longing.

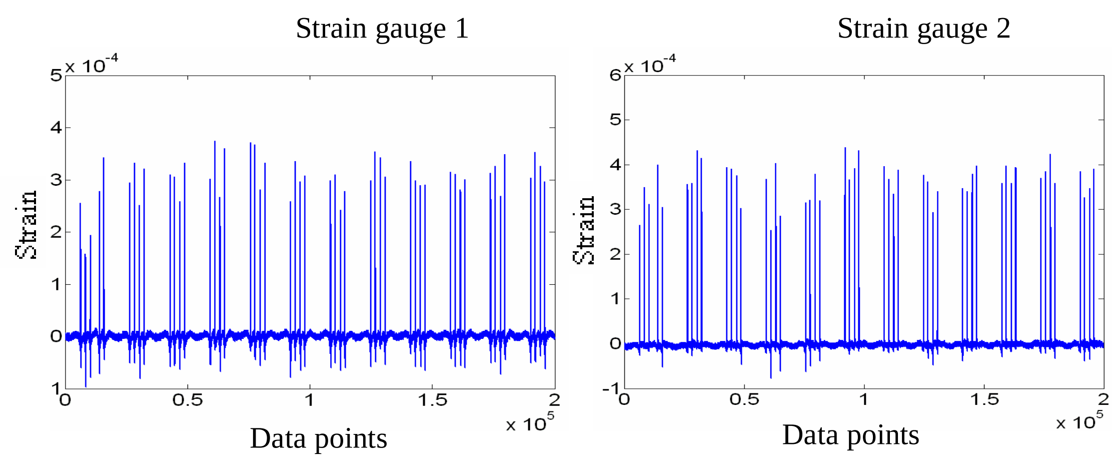

Figure 6.18 Shear strain E_{23} history

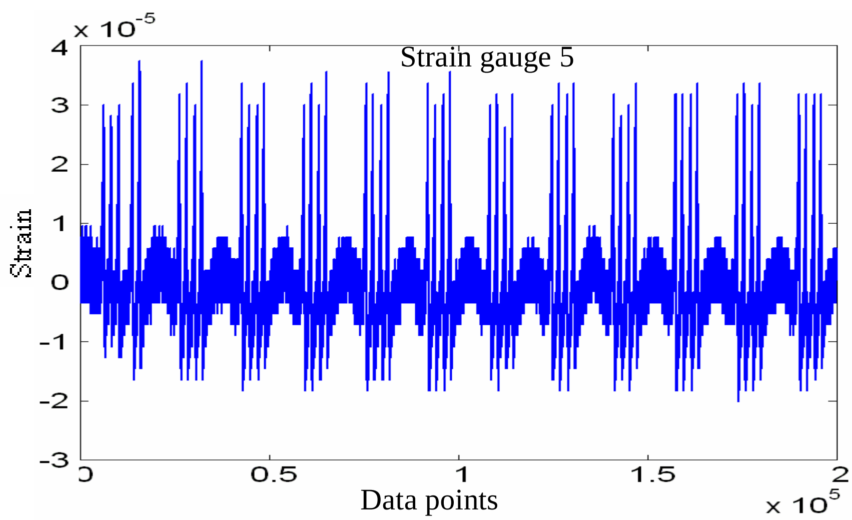

Figure 6.19 Longitudinal strain E_{33} history

The data from Strain gauge 1 are shown in Fig. 6.19; this indicates that the strains on both sides of the rail caused by the passing wheels are different due primarily to eccentric positioning of the wheels. As an approximation in the first stage of analysis, the eccentricity in the wheel position was disregarded as the strain data from Strain gauges 1 and 2 were averaged. Figs. 6.20 and 6.21 present the averaged strain components E_{22} and E_{23}. A set of even peaks are shown in these figures because the wheel eccentricity was eliminated.

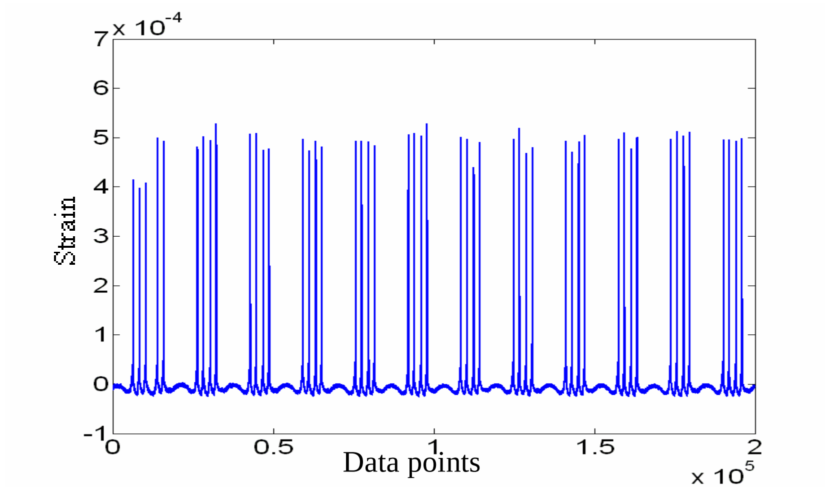

Figure 6.20 Averaged vertical normal strain E_{22} history

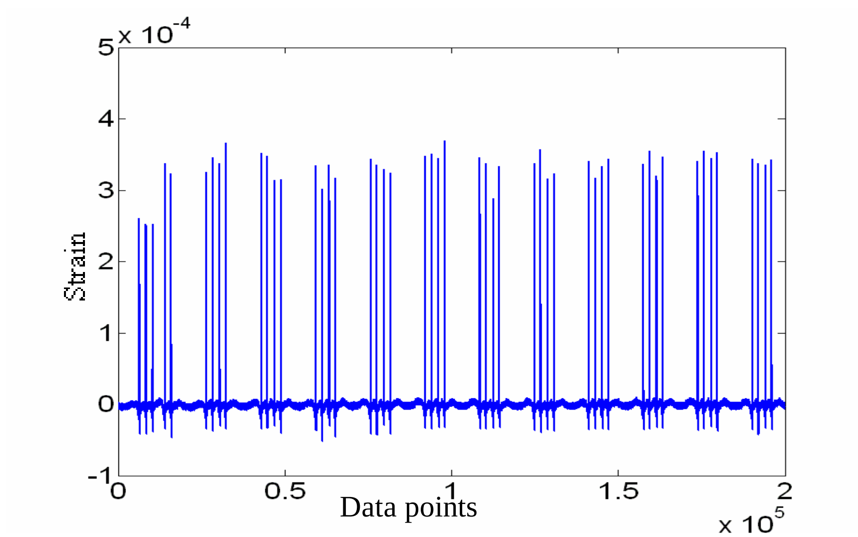

Figure 6.21 Averaged shear strain E_{23} history

6.7. Analysis of Field Data

The field traffic condition is an important factor for FE model validation. A close examination of the field test data helps with understanding the traffic condition and the characteristics of the wheel/IRJ impact as described in this section.

6.7.1. Traffic classification

As the IRJ was subjected to mixed traffic conditions with coal, freight, and passenger trains travelling at different speeds, different axle loads and even different directions, it became necessary to sort out the data according to the type of train prior to analysing the strain history carefully.

Fig. 6.22 illustrates the averaged vertical normal strain data E_{22} corresponding to an unknown train. All we can state is that each impact represents a passing wheel. As the data show that there are 5-impacts as a 'group' (shown circled in Fig. 6.22) at the beginning of the record, it is inferred that the five impacts correspond to that of the rear bogie (three axles) of a diesel locomotive and the front bogie (two axles) of a wagon. It should be noted that due to the delay in triggering of the DAQ system by the ultrasonic sensor, generally the first three bogies of the two locomotives are missed. Subsequent impacts occurred generally in groups of four wheelsets.

The traffic condition is worked out by conducting the data analysis with additional help of QR operational data. Due to confidentiality, the processing details of traffic conditions are not provided in this thesis. The sorted out traffic condition was applied to the FE model for model validation.

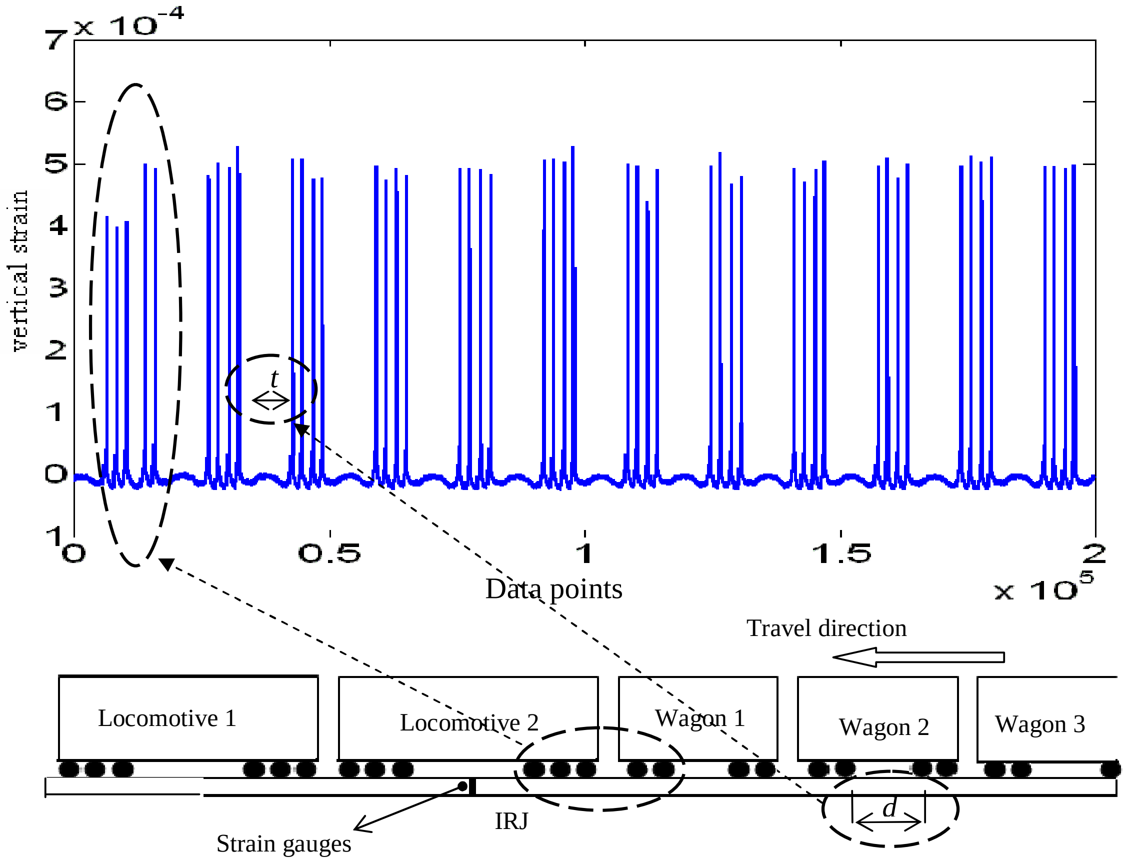

Figure 6.22 Illustration of rollingstock travelling in field test

6.7.2. Vertical strain signature

By zooming into one of the ‘impacts’, the strain signature caused by the moving wheel load is examined. Typically two types of strain signature were found according to different travelling directions. The first signature is shown in Fig. 6.23 where the strain remains at near zero magnitude before the wheel hits the IRJ. As the wheel approaches the IRJ, the strain value sharply increases to a peak value of 491.9 μs within a very short duration. After impact, the strain value damped relatively slowly. It is notable that the passing wheel causes two peaks when the strain gauge is located after the joint. The first peak has a higher magnitude than the second peak. The time interval between the two peaks is 0.95 ms corresponding to approximately

20.0mm with the train longitudinal velocity of 74.5Km/h. Considering the strain gauge located 15 mm from rail end and the thickness of end post material being 10mm, it is believed that the first peak is generated by the wheel/IRJ impact and the second peak is due to the wheel passing above the strain gauge position (15mm from the rail end) as shown in Fig 6.26. It indicates that the wheel/rail impact at the IRJ is captured in this signature.

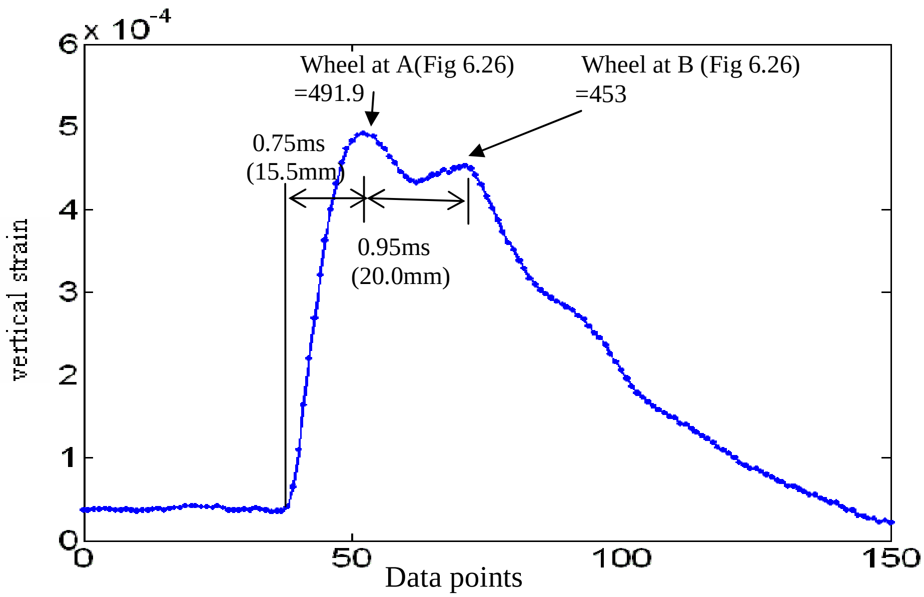

Figure 6.23 Zoom-in of vertical strain history for a wheel passage

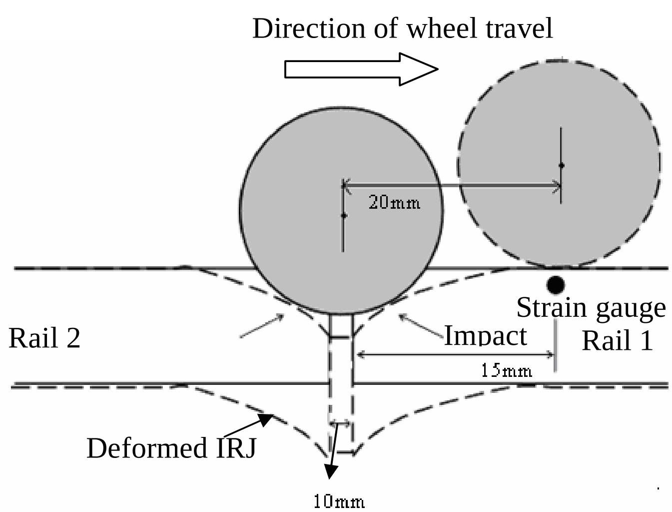

Figure 6.24 Illustration of two peaks generating mechanism

The second signature records a train travels in the opposite direction to the above case. The signature changes as shown in Fig. 6.25. In this case, the strain increases gradually to a peak value. After reaching the peak value it dives sharply to a constant level near zero. As the 'two peak' form does not appear, it is inferred that the impact is not acquired by the strain gauges as they are positioned on the 'first' rail end, referring to Fig. 6.26. It is also inferred that, although the impact is generated by 'two-point contact', the impact force is mostly concentrated on the 'second' rail end of the IRJ.

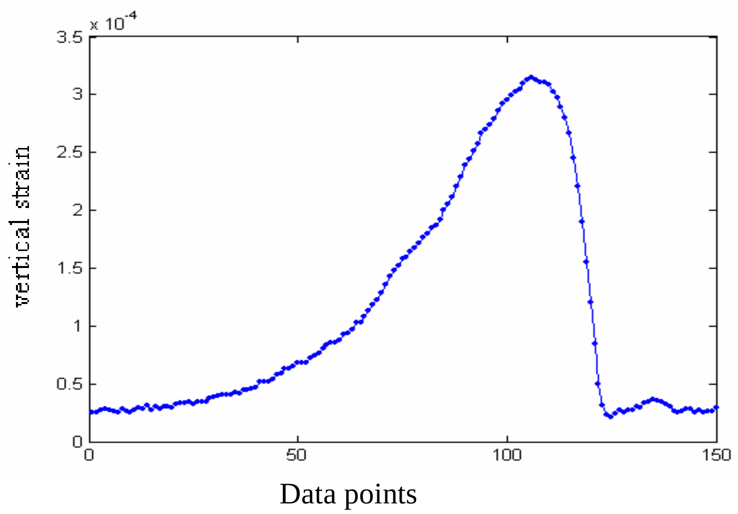

Figure 6.25 Zoom-in of vertical strain history for a wheel passage transporting in an opposite direction

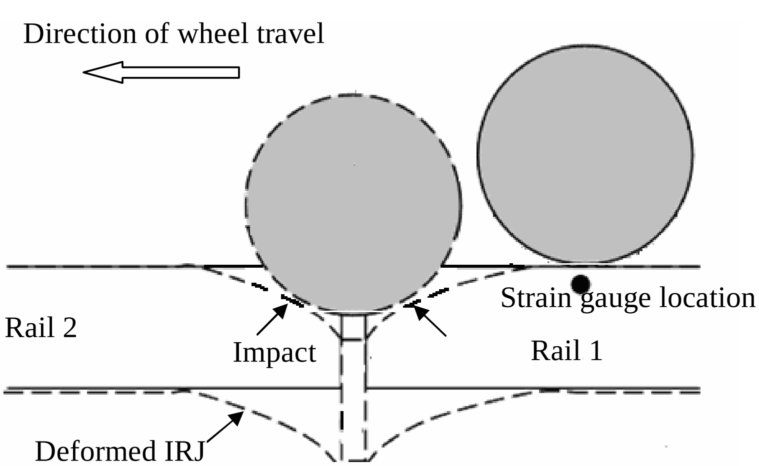

Figure 6.26 Illustration of one peak generating mechanism

6.8. Summary

The strain gauged experiment introduced in this chapter provides a platform to validate the FE model of wheel/rail contact-impact at the IRJ. The static loading experiment was carried out prior to the major field test. The field test was carried out in the live railway track that was designed to capture the dynamic response of the wheel/rail contact impact. The dynamic FE model was employed to identify the best possible locations for strain gauges.

In the lab test it was difficult to ensure the exact symmetry of the application of loading. In the field wheels generally run unsymmetrically on the rail head. As such, both tests have exhibited varying levels of strains on opposite faces of the rails due to lateral bending caused by eccentric loading. The strains were therefore averaged and all analyses thus considered a pseudo symmetric loading state. From the field strain data, it was shown that the traffic direction could be identified. It was also possible to sort out the data as per the type of wagons. The data are used to validate the FE models (static and dynamic) as reported in Chapter 7.

7. Validation of the FE Model of IRJ

7.1. Introduction

The FE results are compared with the strain gauged experimental data in this chapter. Both the static and the dynamic FE analyses results are validated using the lab and field tests respectively. The comparison has generally been regarded as satisfactory.

The experiment is conducted as part of an ongoing research project at the Centre for Railway Engineering (CRE) with the support from QR. This thesis takes the advantage of the experiment by collecting limited experimental data for FE model validation. The vertical strain is selected for the result comparison.

7.2. Validation of Static FEA Model

The IRJ was supported in the lab test different to the condition in the field; hence, the boundary condition of the static FE model was modified. The results of the modified FE model are validated with the lab test data.

As introduced in the Chapter 6, in the static test the IRJ bottom was supported on two steel bars allowing free movement of the IRJ in the longitudinal direction. Referring to Fig. 7.1, for simplicity, the effect of the steel bar contact surface width (18mm) was modelled through coupling the rail bottom to the support bar via a reference node. The boundary condition of the reference nodes' DOF 3 was set free and the remaining five DOFs were arrested. The beam element was also removed from the FE model as the IRJ section was only 2.4m long in the lab test. The boundary condition of the wheel was kept the same as described in Chapter 4 in which DOF 2 was set free and DOFs1 and 3 were arrested. The 150KN vertical load was applied to the railhead.

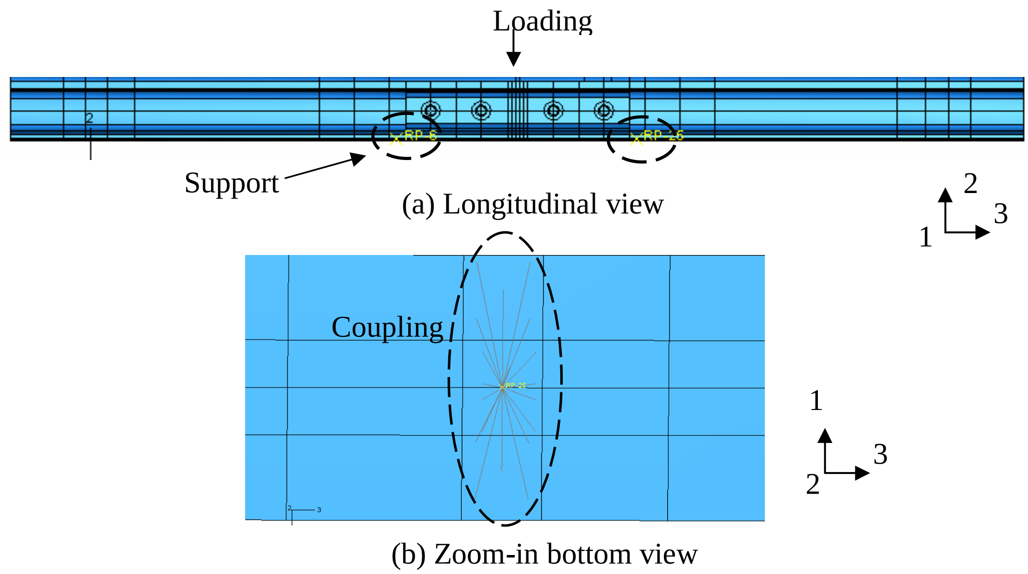

Figure 7.1 Support system of static test

Six different loading positions were simulated in the static FE model. The positions of strain gauges and loadings are illustrated in Fig. 7.2.

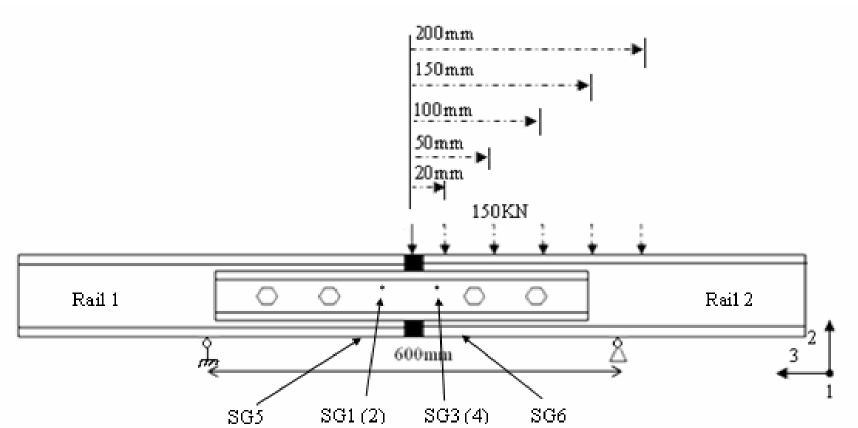

Figure 7.2 Positions of strain gauges and loadings

In Figs. 7.3 and 7.4, the horizontal axis represents the loading positions and the vertical axis shows the vertical strain magnitude. Fig 7.3 shows that the FE results agree well with the tests for the Strain Gauge 1/2. The maximum difference appears at the loading position at the centre (0mm) where the result of the lab test is 264.9 microstrain, while the FE model gave a magnitude of 258.1 with the difference being 2.57% ((264.9-258.1)/264.9). As the loading position moves, the E_{22} strain value from SG 1/2 decreases sharply to a low level. This is because at the 0mm loading position, half of static load is distributed to Rail 1; where the load is moved to other positions, the static load is concentrated on Rail 2. It is worth to note that in this thesis, for plotting convenience, the compression strain is regarded as positive and the tension strain is regarded as negative.

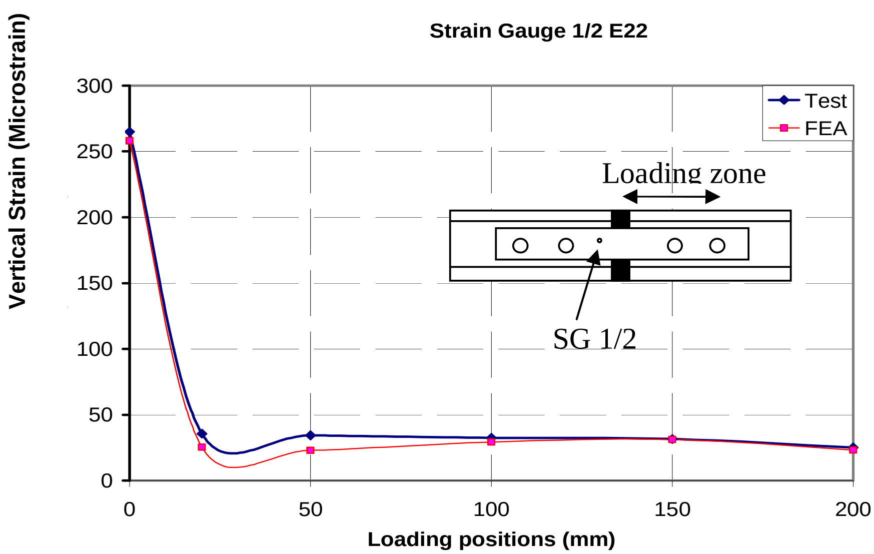

Figure 7.3 Vertical strain E_{22} comparison of Strain Gauge 1/2

The results from SG 3/4 exhibit a different trend as the loadings are positioned at both sides of the strain gauges. Referring to the Fig. 7.4, the peak value of E_{22} emerges at the 20mm loading position which is closest to the strain gauges (strain gauge 3/4 is positioned at 20mm from the IRJ centre). At this point, the simulation error is 3.16% ((464.7-450.0)/464.7).

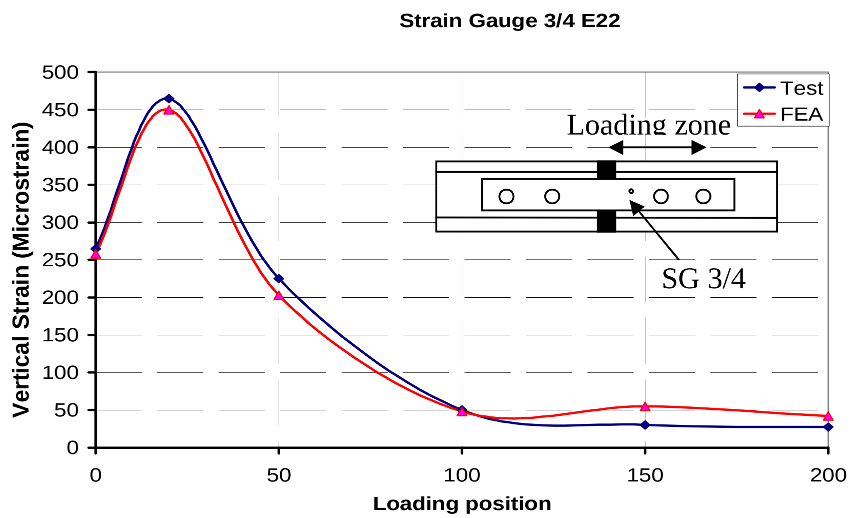

Figure 7.4 Vertical strain E_{22} comparison of Strain Gauge 3/4

7.3. Validation of Dynamic FEA Model

The major traffics on the rail route selected for the field test were the fully loaded heavy haul coal trains heading from left to right and coming back with empty wagons. In this section, two traffic conditions with different vertical wheel load, velocity and travel directions are investigated and compared with the dynamic FEA results.

Chapter 6 has provided brief details of how the traffic condition of the field test has been sorted out with the recorded strain time series. For the loaded coal wagons, the wheel travelling speed was approximately 74.5 Km/h and the vertical wheel load was 130.7 KN. This traffic condition was applied to the dynamic FE model and the strain time series of dynamic FEA were obtained. Because the strain gauges are on the Rail

2, referring to Fig. 7.5, the impact response between the wheel and the IRJ was captured by the strain gauges as explained in the previous chapter.

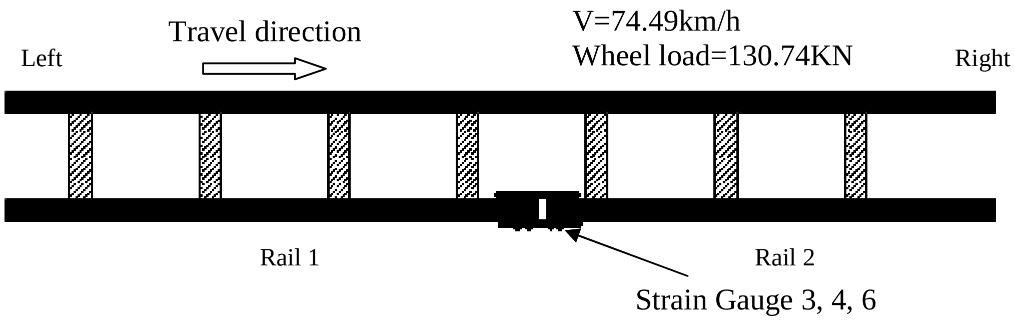

Figure 7.5 Illustrations of strain gauge location and travelling direction

There were 20 strain time series from 20 recorded wheel passages presented and compared to the FEA results. It is worth noting that the wheel loads were approximately close to 130.7KN calculated from the QR operational data which may lead to minor strain magnitude difference among these strain time series. The results of the comparison of vertical strain E_{22} is presented in Fig. 7.6. The vertical strain time series presents a satisfactory agreement between the field test and the FEA. The peak strain caused by the impact at the joint was an average 491.9 microstrain for the test and 469.3 microstrain for the FEA. The error is 4.69% ((491.9-469.3)/491.9). For the FE model, the second peak due to the location of strain gauges was not exhibited as prominently as in the field test data. The curves match well with similar curve slope and the steady strain value before impact.

In the other traffic condition, the empty train travels from right to left with a speed of 80.6 km/h and vertical wheel load of 28.91 KN, as shown in Fig. 7.7. In this condition, the major impact occurs on the Rail 1; as only the strains in Rail 2 were monitored, the strains close to impact were not recorded. However strain peaks corresponding to wheel passage over strain gauge location was traceable. For the purpose of validating the dynamic FE model, such data was considered sufficient.

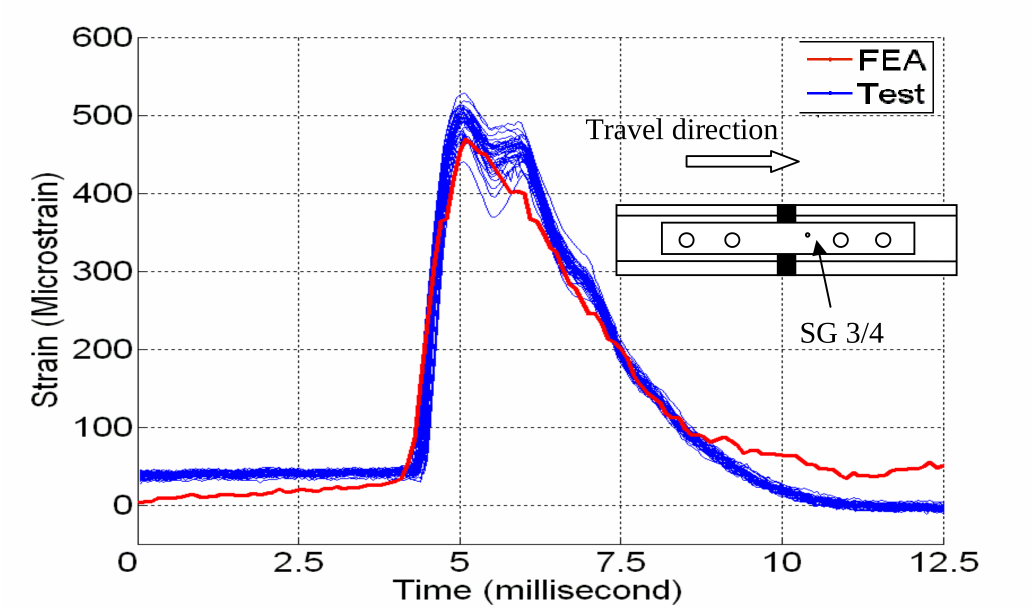

Figure 7.6 Vertical strain E_{22} comparison of Strain Gauge 3/4

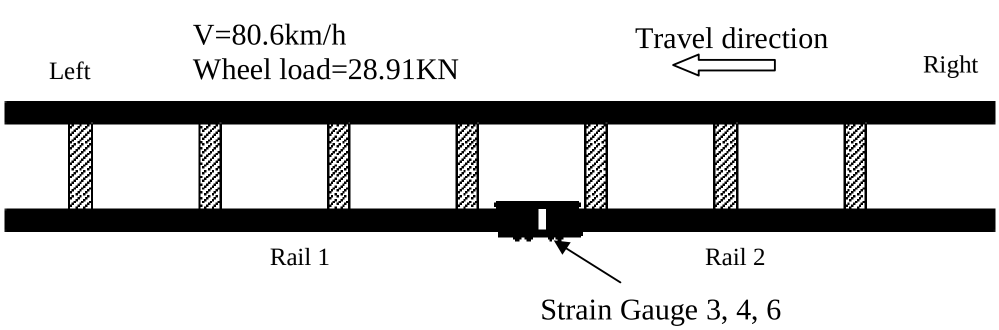

Figure 7.7 Illustrations of strain gauge location and travelling direction

Fig 7.8 presents that the peak values of FEA and field test are found relatively close. Before the peak, the FEA has predicted higher value of up to negative 60 microstrain. In the field test the strain were 10-20 microstrains at the beginning and gradually increases to 45 microstrain before the sharp surge to the peak.

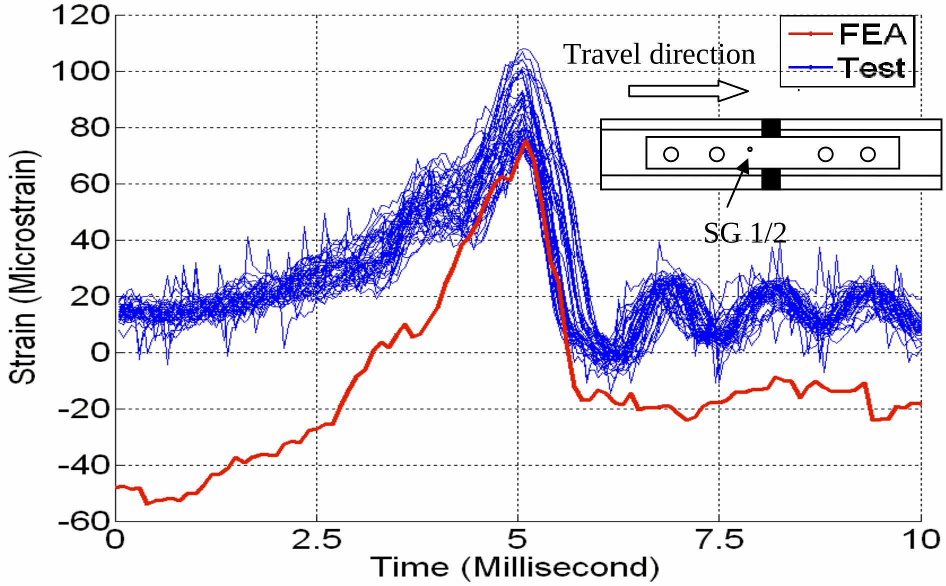

Figure 7.8 Vertical strain E_{22} comparison of Strain Gauge 3/4

7.4. Summary

In this chapter the results of the tests and FE model were compared. The static results generally demonstrated satisfactory agreement between the lab test and static FE model. In the dynamic FE model validation section, two traffic conditions were investigated. Similar to the static analysis, the vertical strain on the rail web showed reasonable agreement between the FEA and test. In general, as the purpose of this research is to investigate the contact-impact force at the IRJ, the agreements of strain results are acceptable considering the explicit time integration method has certain short coming with regard to strain/stress level accuracy.

8. Summary & Conclusions

The wheel/rail contact impact forces that occur in the vicinity of the end post at the insulated rail joints (IRJs) has been examined and reported in this thesis. The Finite Element Method and strain gauged experiments have been used in the examination.

The 3D wheel/rail contact-impact FE model employed a two-stage analysis strategy in which the wheel-IRJ railhead contact was first established in the static analysis and the results transferred to dynamic analysis for impact simulations. This strategy was proven efficient to obtain a fast and efficient solution of a steady state rolling contact prior to the impact. The explicit FE method was employed in the dynamic analysis. The master/slave contact surface method was adopted for both the static and the dynamic analyses. To achieve a reasonable model size which is acceptable to the available computing facility, several idealisation and simplification strategies have been employed in following aspects:

- IRJ assembly and wheel profile
- material modelling
- boundary conditions

Some special attention was also paid to the following FE modelling strategies:

- loading
- contact modelling
- meshing

The wheel/rail contact-impact in the vicinity of the end post was exhibited via numerical examples from the FE modelling. The wheel/rail contact impact mechanism was investigated and reported. The associated results of wheel/rail contact were also compared with the HCT. Through a series of sensitivity studies of several IRJ design parameters, it was shown that the IRJ performance can be largely improved with optimised design parameters.

The strain gauged lab and field experiments were reported. The data collected from both tests were processed and compared to the numerical results. The signature of the strain data from the field test was discussed. Both the static and the dynamic FE models were validated using the experimental data. In the lab test, the IRJ was simply supported and subjected to a static load and investigated with several different loading positions along the length of the IRJ. Two traffic conditions in the field test, namely loaded and unloaded coal wagon traffic, were selected to validate the dynamic analysis. Reasonable agreements between the FEA and tests have been achieved.

8.1. Conclusions

From the FEA and experiments as reported above, there are several general conclusions obtained as stated in the following part. The specific conclusions can be drawn from the numerical examples and the corresponding experimental data.

8.1.1. General conclusions

(1) The wheel/rail contact impact mechanism can be explained through the stiffness discontinuity of the IRJ structure causes a running surface geometry discontinuity during the wheel passages which then causes the impact in the vicinity of the end post.

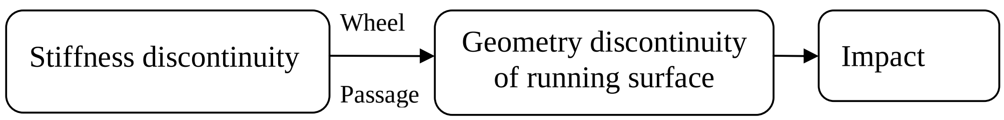

(2) At impact, the peak contact pressure reduces due to an apparent increase in contact area. In spite of the reduction in peak contact pressure, the maximum Von-Mises stress at impact is larger relative to the pre and post impact stages. Discontinuity of rail in the vicinity of the end post appears to be the primary factor influencing the large increase in Von-Mises stresses.

(3) At the impact, the wheel contacts both rails across the end post.

(4) This 3D wheel/rail contact impact FE model appropriately predicts the wheel/rail contact impact at the IRJs. It is also suitable to be used to conduct the sensitivity study of the design parameters and further improve the design.

(5) The sensitivity study has shown that the impact forces have generally been reduced when any one of the following design parameters are adopted:

- Gluing the end post
- Reducing the gap size
- Adopting flexible support system
- Using end post material with mechanical properties closer to those of steel
- Suspending IRJs between sleepers

The numerical example showed that when all these options employed, the impact factor (between a new IRJ and a new wheel) was reduced to a negligible level.

(6) The static analysis has shown that the elastic model agree well with the HCT in terms of the contact area dimensions and contact pressure distribution. The HCT has been found to be not valid at impact due to the edge effect.

(7) The mesh size influences the contact results significantly. Accurate results of the contact area dimensions and contact pressure distribution require fairly refined mesh within the contact zone. However, the global-scale result such as contact force is not so sensitive to the mesh size within the contact zone.

8.1.2. Specific conclusions

(1) The comparison between two available contact constraint enforcement methods in ABAQUS/Explicit, namely, Penalty method and Kinematic method, shows that the Penalty method is more stable numerically.

(2) Under 150KN vertical wheel load and 120Km/h longitudinal velocity, the impact

factor of 1.16 was generated between a new wheel and a new IRJ.

(3) The stress contour showed that the maximum stress was located at 3mm~4mm beneath the contact surface of the railhead. The 150KN wheel load caused fairly localised material plasticity in the wheel/rail contact zone.

(4) The pure sliding motion of a wheel (wheel under braking) generates higher impact load than the pure rolling wheel motion by 13% in the example. This finding indicates the braked case is more likely to cause railhead damage in the vicinity of an end post.

(5) The experiment data analysis indicates that the positions on the railweb of an IRJ in the vicinity of the end post are suitable for dynamic load response capture using strain gauges.

8.2. Recommendations

There are several recommendations listed as follows which could further improve the study on the wheel/rail contact impact at IRJs:

(1) To exactly measure the contact impact forces, only expensive systems such as the fully instrumented wheelsets are practically used at this stage. The strain gauged experiments reported in this thesis could be further developed to an inexpensive wayside monitoring technique that determines the contact-impact forces inversely through strain signatures.

(2) The mesh used in the dynamic analysis could be further refined with a higher performance computing facility to obtain more accurate results for the contact associated parameters (such as the contact area, contact pressure distribution etc.)

(3) The permanent deformation or damage on the railhead aggravates the contact-impact force, generating a vicious circle accelerating the overall failure of IRJs. Progressive wheel loads could be applied to the model to investigate the long term impact growth under this scenario.

(4) Although efficient meshing strategy is developed in this thesis, the computational cost is still considerably high, which limits the model for further development. Comparing with the Lagrangian formulation, the ALE formulation maybe more efficient for rolling contact problems. The ALE configuration, despite its rare application for commercial FE codes, may be considered as an alternative option in the future.

References

ABAQUS (2003). *ABAQUS Analysis User's Manual*, version 6.4, ABAQUS Inc.

AKRAILROAD, *Insulated Joints*, viewed August 2006, http://www.akrailroad.com/ins_joints.html

ANDERSSON, C. & DAHLBERG, T. (1998). Wheel/rail impacts at a railway turnout crossing. *Proceedings of Institution of Mechanical Engineers,* 212**,** 123-134.

AREMA, A. R. E. A. M. A. *Practical Guide*, viewed August 2006, http://www.arema.org/eseries/scriptcontent/custom/e_arema/Practical_Guide/PGChapter3.pdf.

BAEZA, L., RODA, A. & NIELSEN, J. C. O. (2006). Railway vehicle/track interaction analysis using a modal substructuring approach. *Journal of sound and vibration,* 293**,** 112-124.

BEER, F. P., JOHNSTON, E. R. & DEWOLF, J. T. (1915) *Mechanics of Materials*, McGrawHill.

BEZIN, Y., IWNICKI, S., STOW, J., BLAIR, S. & KAY, T. (2005). Development of a method to predict stress in rails using ADAMS/Rail and ABAQUS. *Internal communication.*

BOGY, D.B. (1971). Two edge-bonded elastic wedges of different materials and wedge angles. *Trans. ASME, Series E, Journal of Applied Mechanics*, 38, 377.

BONNETT, C. F. (1996) *Practical Railway Engineering*, Imperial College Press.

BRINKMEIER, M, NACKENHORST, U & ZIEFLE M. (2007). Finite Element Analysis of Rolling Tires A State of the Art Review, *Internal communication*, Gottfried Wilhelm Leibniz Universit¨at Hannover Germany

BUSQUET, M., L. BAILLET, BORDREUIL, C. & BERTHIER, Y. (2005). 3D finite element investigation on the plastic flows of rolling contacts-correlation with railhead microstructural observation. *Wear,* 258**,** 1071-1080.

CARTER, F. W. (1926). On the action of a locomotive driving wheel. *Proceedings of the Royal Society of London***,** 151-157.

CHEN, Y. & CHEN, L. (2006). Effects of insulated rail joint on the wheel/rail contact stresses under the condition of partial slip. *Wear,* 260**,** 1267-1273.

CHEN, Y. C. (2003). The effect of proximity of a rail end in elastic-plastic contact between a wheel and a rail. *Proceedings of Institution of Mechanical Engineers,* 217**,** 189-201.

CHEN, Y. C. & KUANG, J. H. (2002). Contact stress variations near the insulated rail joints. *Proceedings of the Institute of Mechanical Engineers, Part F, Jounal of Rail and Rapid Transit,* 216**,** 265-274.

CHOLLET, H. (1999). Contact roue-rail. *Internal report. INRETS.*

COMNINOU, M. (1976). Stress singularities at a sharp edge in contact problems with friction. *Zeitschrift für Angewandte Mathematik und Physik (ZAMP),* 27, 493

COOK, R. D. (1995) *Finite Element Modelling for Stress Analysis,* Canada, John Wiley & Sons.

COOK, R. D., Malkus, D. S., & E.Plesha, M. (1989). *Concept and Application of finite element analysis* (3rd edition ed.). Canada: John Wiley & Sons.

CURNIER, A. & Alart, P. A. (1988). A generalized Newton method for contact problems with friction. *J. Mec. Theor. Appl*., 7, 67-82.

DANIEL, I. M. & ISHAI, O. (1994). *Engineering mechanics of composite materials,* Oxford, Oxford Univerisity Press.

DAVIS, D. D. & AKHTAR, M. N. (2005). Improving the performance of bonded insulated joints. *RT and S: Railway Track and Structures,* 101**,** 14-17.

DUKKIPATI, R. V. & DONG, R. (1999). The dynamic effect of conventional freight car running over a dipped-joint. *Vehicle System Dynamics,* 31**,** 95-111.

DUNDURS, J. & LEE, M. S. (1972). Stress concentration at a sharp edge in contact problems. *Journal of Elasticity*, 2, 109.

ESVELD, C. (2001). *Modern Railway Track*, Delft University of Technology.

FARHAT NIA, F, SALIMI, M & MOVAHHEDY, M.R.(2006). Elasto-plastic finite element simulation of symmetrical plate rolling using an ALE approach. *Journal of Materials Processing Technology*,177,524-529

FERMER, M. & NIELSEN, J. C. O. (1995). Vertical interaction between train and track with soft and stiff rail pads-full scale experiments and theory. *Proceedings of institution of mechanical engineers,* 209**,** 39-47.

FISCHER-CRIPPS, A. C. (2000) *Introduction to Contact Mechanics,* Linfield Australia, Springer-Verlag.

FROHLING, R. D. (1997) Deterioration of Railway Track due to Dynamic Vehicle Loading and Spatilly Varying Track Stiffness. *Faculty of Engineering.* Pretoria, University of Pretoria.

GDOUTOS, E.E. & THEOCARIS, P.S. (1975). Stress concentrations at the apex of a plane indenter acting on an elastic half-plane. Journal of Applied Mechanics, Trans ASME, Series E, 42, 109.

GOODMAN, L.E. (1962). Contact stress analysis of normally loaded rough spheres. *Trans. ASME, Series E, Journal of Applied Mechanics*, 29, 119-121

HERTZ, H. (1896). On the contact of elastic solids. IN JONES & SCHOTT (Eds.) *Miscellaneous papers.* London, Macmillan.

HERTZ, H. (1896). On the contact of rigid elastic solids and on hardness. IN JONES & SCHOTT (Eds.) *Miscellaneous papers.* London, Macmillan.

IKEDA, K., SUMIT, T. & SASAKI, S. (1998). Characteristics of irregular inclination of rail vibration in the rail joint. *Proceedings of the Western Branch in JSCE***,** 136-138.

JENKINS, H. H., STEPHENSON, J. E., CLAYTON, G. A., MORLAND, G. W. & LYON, D. (1974). The effect of track and vehicle parameters on wheel/rail vertical dynamic forces. *Railway Engineering Journal,* 3**,** 2-16.

JOHNSON, K. L. (1985) *Contact Mechanics*, Cambridge, Cambridge University Press.

LAURSEN, T.A. (2002)， *Computational Contact and Impact Mechanics,* Springer, Germany.

KATAOKA, H., ABE, N.,WAKATSUKI, O. & OIKAWA, Y. (1997). A dynamic stress analysis of joint rails using finite beam element model (in Japanese). *Proceedings of the 14th Japan National Sysposium on Boundary Element Method***,** 93-98.

KALKER, J. J. (1964). The transmission of a force and couple between two elastically similar rolling spheres. *Proc. Kon. Ned. Akad. van Wetenschappen,* 135**,** 258.

KERR, A. D. & COX, J. E. (1999). Analysis and test of bonded insulated rail joints subjected to vertical wheel loads. *International journal of mechanical sciences,* 41**,** 1253-1272.

KHADEM, R & O'CONNOR, J. J. (1969). Adhesive or frictionless compression of an elastic rectangle between two identical elastic half-spaces. *International Journal of Engineering Sciences*, 7, 153, 111.

KHADEM, R & O'CONNOR, J. J. (1969). Axial compression of an elastic circular cylinder in contact with two identical elastic half-spaces. *International Journal of Engineering Sciences*, 7, 785, 111.

KNIGHT, C. E. (1993) *The Finite Element Method in Mechanical Design*, PWS KENT.

KORO, K., ABE, K., ISHIDA, M. & SUZUKI, T. (2004). Timoshenko beam finite element for vehicle-track vibration analysis and its application to jointed railway track. *Proceedings of Institution of Mechanical Engineers*, 218**,** 159-172.

LI, Z., ZHAO, X., ESVELD, C. & DOLLEVOET, R. (2006). Causes of squats: correlation analysis and numerical modelling. *Proceedings of 7th international conference on contact mechanics and wear of rail/wheel systems,* 2**,** 439-446.

LBFOSTER, *Rail Products*, viewed August 2006, http://www.lbfoster.com/content.aspx?id=1452.

NEDCAN (2006). http://www.nedcan.com/sales/tenconi/index.html.

NEWMARK, N. M. (1959). A method of computation for structural dynamics. *Jourmal of the Engineering Mechanics Division, ASCE*, 67-94.

NEWTON, S. G. & CLARK, R. A. (1979). An investigation into the dynamic effect on the track of wheel flats on railway wagon. *Journal of Mechanical Engineering and Science,* 21**,** 287-297.

NORFAST (2006). Insulated Joint. *Railway Track and Structures,* September**,** 35.

PANG, T. & DHANASEKAR, M. (2006). Finite element analysis of the wheel-rail interaction adjacent to the insulated rail joints. *Proceedings of 7th international conference on contact mechanics and wear of rail/wheel systems,* 2**,** 509-516.

PAU, M., AYMERICH, F. & GINESU, F. (2002). Distribution of contact pressure in wheel–rail contact area. 253**,** 265–274.

PONTHOT, J & BELYTSCHKO, T. (1997). Arbitrary Lagrangian-Eulerian formulation for element-free Galerkin method. *Comput. Methods Appl. Mech. Engrg.* 152, 19-46

RAIL, L. (2006). http://www.lbfoster.com/railproducts/alleghenyrail.html.

RAILCRC (2003). Project 75: Development of Novel Insulated Joints. http://www.railcrc.cqu.edu.au/research/projects/75.html.

RAILFOTO (2005). *Insulated Rail Fishplate Joint*, viewed August 2006, http://railfoto.fotopic.net/p15613474.html

REDDY, J.N. (1984). *An introduction to the finite element method*. New York, St Louis, San Francisco, Toronto, London, Sidney: McGraw-Hill.

RINGSBERG, J. W. & JOSEFSON, B. L. (2001). Finite element analyses of rolling contact fatigue crack initiation in railheads. *Proceedings of Institution of Mechanical Engineers,* 215**,** 243-259.

ROARK, R.J. (1965). *Formulas for stress and strain,* 4th Edition. New York, St Louis, San Francisco, Toronto, London, Sidney: McGraw-Hill.

SCHUPP, G., WEIDEMANN, C. & MAUER, L. (2004). Modelling the Contact Between Wheel and Rail Within Multibody System Simulation. *Vehicle System Dynamics,* 41**,** 349-364.

STANDARD AUSTRALIA, (2002). *Australia standard: Railway track material Part 1: Steel rails,* (AS1085.1-2002), Standard Australia, North Sydney.

STANDARD AUSTRALIA, (2002). *Australia standard: Railway track material Part 12: Insulated Joints Assemblies*, (AS1085.12-2002), Standard Australia, North Sydney.

STANDARD AUSTRALIA & STANDARD NEWZEALAND, (1996), *Australian/New Zealand Standard: High-strength steel bolts with associated nuts and washers for structural engineering,* (AS/NZS 1252:1996), Standard Australia Standard New Zealand.

STOLARSKI, T. A. & TOBE, S. (2000) *Rolling Contacts*, Suffolk UK, Professional Engineering Publishing Limited.

STEENBERGEN, M. J. M. M. (2006). Modelling of wheels and rail discontinuities in dynamic wheel-rail contact analysis. *Vehicle System Dynamics,* 44**,** 763-787.

STEM (2006). Project: 75 Insulated Joints Evaluation and Management Report 2005 Portfolio. Melbourne, Rail CRC.

SUN, Y. Q. (2003) A Wagon-Track System Dynamics Model for the Simulation of Heavy Haul Railway Transportation. *Engineering Faculty* Rockhampton Central Queenland University.

SUN, Y. Q. & DHANASEKAR, M. (2002). A dynamic model for the vertical interaction of the rail track and wagon system. *International journal of solids and structures,* 39**,** 1337-1359.

TONG, D. (1986). *Railroad Track,* Beijing, China railway publishing house.

TIMOSHENKO, S& Goodier, J.N. (1951). *Theory of Elasticity,* 3rd Edn. New York, London et al.: McGraw-Hill

UGURAL, A. C. & FENSTER, S. K. (1995) *Advanced Strength and Applied Elasticity,* NewJersey, PrenticeHall PTR.

WANG, M., C. (2003). *Finite Element Method(In Chinese),* Tsinghua University Press, Beijing.

WEN, Z., JIN, X. & ZHANG, W. (2005). Contact-impact stress analysis of rail joint region using the dynamic finite element method. *Wear,* 258**,** 1301-1309.

WIEST, M., DAVE, W., FISCHER, F. D. & OSSBERGER, H. (2006). Deformation and damage of a crossing nose due to wheel passages. *Proceedings of 7th international conference on contact mechanics and wear of rail/wheel systems,* 2**,** 517-525.

WIEST, M., KASSA, E., DAVE, W., NIELSEN, J. C. O. & OSSBERGER, H. (2006). Assessment of methods for calculating contact pressure in wheel-rail/switch contact. *Proceedings of 7th international conference on contact mechanics and wear of rail/wheel systems,* 2**,** 501-508.

WRIGGERS, P. (2002). *Computational Contact Mechanics*, John Wiley & Sons Ltd, England.

WU, T. X. & THOMPSON, D. J. (2003). On the impact noise generation due to a wheel passing over rail joints. *Journal of sound and vibration***,** 485-496.

WU, T. X. & THOMPSON, D. J. (2004). The effect of track non-linear on wheel/rail impact. *Procedings of Institution of Mechanical Engineers*, 218, Part F: Journal of Rail and Rapid Transit**,** 1-10.

YAN, W. & FISCHER, F. D. (2000). Applicability of the Hertz contact theory to rail-wheel contact problems. *Archive of Applied Mechanics,* 70**,** 255-268.

ZHAI, W. (1996). Locomotive-and-track system coupling dynamics and its application to the study of locomotive performance. *Journal of China Railway Science,* 17**,** 58-73.

ZIEFLE, M. (2007) Numerische Konzepte zur Behandlung inelastischer Effekte beim reibungsbehafteten Rollkontakt. *Phd–thesis*, Leibniz Universit¨at Hannover

ZIEFLE, M. & NACKENHORST, U. (2004). On the Treatment of inelastic materials within an ALE-formulation of rolling contact. *PAMM · Proc. Appl. Math. Mech.* 4, 388–389

ZIENKIEWICZ, O. C. (1971) *The Finite Element Method in Engineering Science,* London, McGrawHill.